NON-LINEAR FREE-SURFACE FLOWS ABOUT BLUNT BODIES

by

Lawrence K. Forbes

B.Sc.(Hons.), University of Adelaide, South Australia.

Thesis submitted for the degree

of Doctor of Philosophy

in the

University of Adelaide

Department of Applied Mathematics

March 1981

SUMMARY

In this thesis, three problems of inviscid free-surface hydrodynamics are investigated. The behaviour of the fluid at the free surface is governed by non-linear equations, and the free surface of the stream is disturbed by an immersed body. The body may be regarded as blunt, in the sense that its forward face is somewhere perpendicular to the direction of the flow of the oncoming stream. There is thus a stagnation point on the forward face of the body, so that approximate theories which involve assumptions of body slenderness may not be applied directly.

The first of these problems is discussed in chapter one. Here, a blunt-nosed body, such as a bridge pier, is considered to be standing in a fast-flowing shallow stream. The non-linear shallow water equations are used, and the bow wave upstream of the body is regarded as a shock front (hydraulic jump), across which suitable jump conditions are prescribed. The problem is then solved inversely, by assuming a known shape for the upstream bow wave, and seeking to determine the position and shape of the body. The flow variables are expressed as Taylor series expansions about the bow wave, and the computer is used to obtain numerical values for the coeff-icients. Several singularities in the flow field are discovered and discussed.

The second problem, discussed in chapter two, concerns two-dimensional flow of an ideal fluid in a horizontal stream, attached to the bottom of which is a semi-circular obstruction.

Infinitely far upstream, the fluid flows uniformly, with a known Froude number F. A new linearized theory is presented, which is valid for semi-circular obstructions of small radius, and accounts for the behaviour of the fluid at the stagnation points on the bottom. This theory predicts a train of downstream waves whenever the flow is subcritical $(F < 1)$, and a symmetric wave-free surface profile whenever the flow is supercritical $(F > 1)$. The exact non-linear equations are then solved numerically at the free surface using a boundary-integral technique and a Newton-Raphson procedure. Non-linear solutions possessing a train of downstream waves are obtained for $F < 1$, and solutions free of waves for $F > 1$. The non-linear results suggest that the validity of the wave-like solution may extend into $F > 1$, overlapping with the domain of validity of the wave-free solutions.

In chapter three, the semi-circular obstruction of the previous chapter is generalized to include the case of a semi-elliptical body attached to the bottom. Attention is confined to the subcritical region $F < 1$, where it is shown that, for ellipses of certain special lengths, the non-linear downstream wave amplitude may be made to vanish, resulting in zero wave resistance.

SIGNED STATEMENT

The contents of this thesis have not been submitted to any university for the purpose of obtaining any other degree or diploma. Also, to the best of my knowledge and belief, the thesis contains no material previously published or written by another person, except where due reference is made in the text.

L.K. Forbes

ACKNOWLEDGEMENTS

I wish to thank my supervisors, Dr. L.W. Schwartz and Professor E.O. Tuck, for their many helpful suggestions and the keen interest they displayed in the progress of this work. They have provided a stimulating intellectual environment, without which the pursuit of this research would not have been possible.

The financial support of an Australian Commonwealth Postgraduate Research Award during the three years of full-time research on this thesis is gratefully acknowledged.

I am also indebted to Mrs. Angela McKay for her efficient typing of this manuscript.

TABLE OF CONTENTS

CHAPTER ONE

SUPERCRITICAL FLOW ABOUT A BLUNT OBSTACLE IN SHALLOW WATER

1.1 Introduction

The topic of the present chapter represents a direct extension of the now classical blunt-body problem of gas-dynamics to a similar problem arising in shallow-water theory. Here, we consider a blunt object, such as a bridge pier, immersed in a supercritical water stream, and supporting a detached bow shock-wave, or bore. The problem is formulated inversely, that is, the free-stream Froude number and the shape of the shock-wave are specified in advance, and it is then required to determine the values of the flow variables downstream and the shape of the body. The shock conditions are used to relate flow quantities on the upstream and down-stream sides of the shock, and so serve as initial data for the partial differential equations describing the behaviour of the fluid in the shock layer.

The earliest attempts to solve the blunt-body problem of gas-dynamics involved formulating the problem inversely, as in the present study, and seeking to represent the flow variables in the shock layer as Taylor-series expansions about the shock-wave (see for example Cabannes (1951)). However, it was pointed out by Van Dyke (1958a, 1958b) that these Taylor series describe not only the region of physical interest

downstream of the shock wave, but also a physically fictitious region upstream of the shock where there exists a singular line, corresponding to an envelope of outgoing characteristics. As this singular line apparently always lies closer to the shock than does the body, the series expansions do not include the body within their domains of convergence. Thus, attempts to locate the body by simply summing terms in the power series are unsuccessful, since the series themselves become divergent in the vicinity of the body. Accurate results may nevertheless be obtained at the body, however, by devising some method of analytic continuation to extend the range of usefulness of the series downstream. Some of the earlier methods for doing this are reviewed by Hayes and Probstein (1966) and Van Dyke (1975).

Solutions to the gas-dynamic blunt-body problem have been produced more recently by Schwartz (1974a, 1975). The problem is again formulated inversely and the flow variables in the shock layer are expressed as Taylor-series expansions about the shock apex. The coefficients of the Taylor-series are computed to high order using a digital computer to perform the necessary arithmetic, and the series are then recast as Padé approximants (rational fractions) in order to provide the required analytic continuation downstream. For the case of an axisymmetric body supporting a paraboloidal bow-shock wave, Schwartz (1974a) demonstrated that he could accurately locate the position of the body as far as 200 shock-nose radii downstream, where his results showed substantial agreement with far-field asymptotic solutions. In a later investigation of the more general planar asymmetric problem in which the

shock is set at an arbitrary angle of attack to the upstream flow, Schwartz (1975) identified several singular lines within the flow region downstream of the shock, and demonstrated that the streamline of maximum entropy which intersects the shock at right angles is not generally the body streamline.

It is well known that the non-linear equations of shallow-water theory are analogous to those of gas-dynamics for an hypothetical gas having an adiabatic exponent $\gamma = 2$ (Preiswerk (1938))*; indeed this so-called hydraulic analogy is often used as a means of flow visualization for the supersonic blunt-body problem of gas-dynamics (see for example Stoker (1957) and Werlé (1973)). The shallow-water blunt-body problem is also of interest in its own right, since it models such situations as the flow about a bridge pier in a supercritical stream. It may also serve as a first approximation to the flow near the bow of a non-slender ship.

Recently, Pandolfi and Zannetti (1977) reported a numerical solution to the shallow-water blunt-body problem, in which a body was specified and the position of the shock found by a time-dependent iterative technique. The work presented in this chapter aims to complement that of the above authors, by concentrating on the mathematical structure of these solutions, and the extent to which they differ from the gas-dynamic blunt-body solutions.

---

* - there is also a very close analogy between the equations of shallow-water theory and those describing incompressible fluid flow in an elastic-walled tube, as is discussed by Forbes (1981).

1.2 Formulation of the Problem

Consider a cartesian coordinate system with the x- and z-axes lying along the undisturbed free surface, and the y-axis pointing vertically, as in Stoker (1957). The shock apex is at the origin, and the shock nose radius is R_s. Upstream, the flow is uniform, with depth H_∞ and velocity V_∞, and makes an angle α with the x-axis. The fluid is subject to the downward acceleration of gravity, g. This dimensional coordinate system is shown in Fig. 1.1.

We proceed immediately to dimensionless variables, under the shallow water approximation $H_\infty/R_s \to 0$. Thus the horizontal lengths x and z are made dimensionless with respect to R_s, while H denotes the total depth of fluid made dimensionless with respect to H_∞. The x- and z-components of velocity, U and W, are referred to the quantity V_∞. Under this approximation, the vertical component of velocity is assumed to be zero, and the equations of motion in the shock layer become (Stoker (1957))

$$UU_x + WU_z + H_x/F_\infty^2 = 0 \qquad (1.1a)$$

$$UW_x + WW_z + H_z/F_\infty^2 = 0 \qquad (1.1b)$$

$$(UH)_x + (WH)_z = 0 \,, \qquad (1.1c)$$

where the upstream Froude number is given by

$$F_\infty = \frac{V_\infty}{(g\, H_\infty)^{1/2}} \,,$$

and subscripts denote partial differentiation.

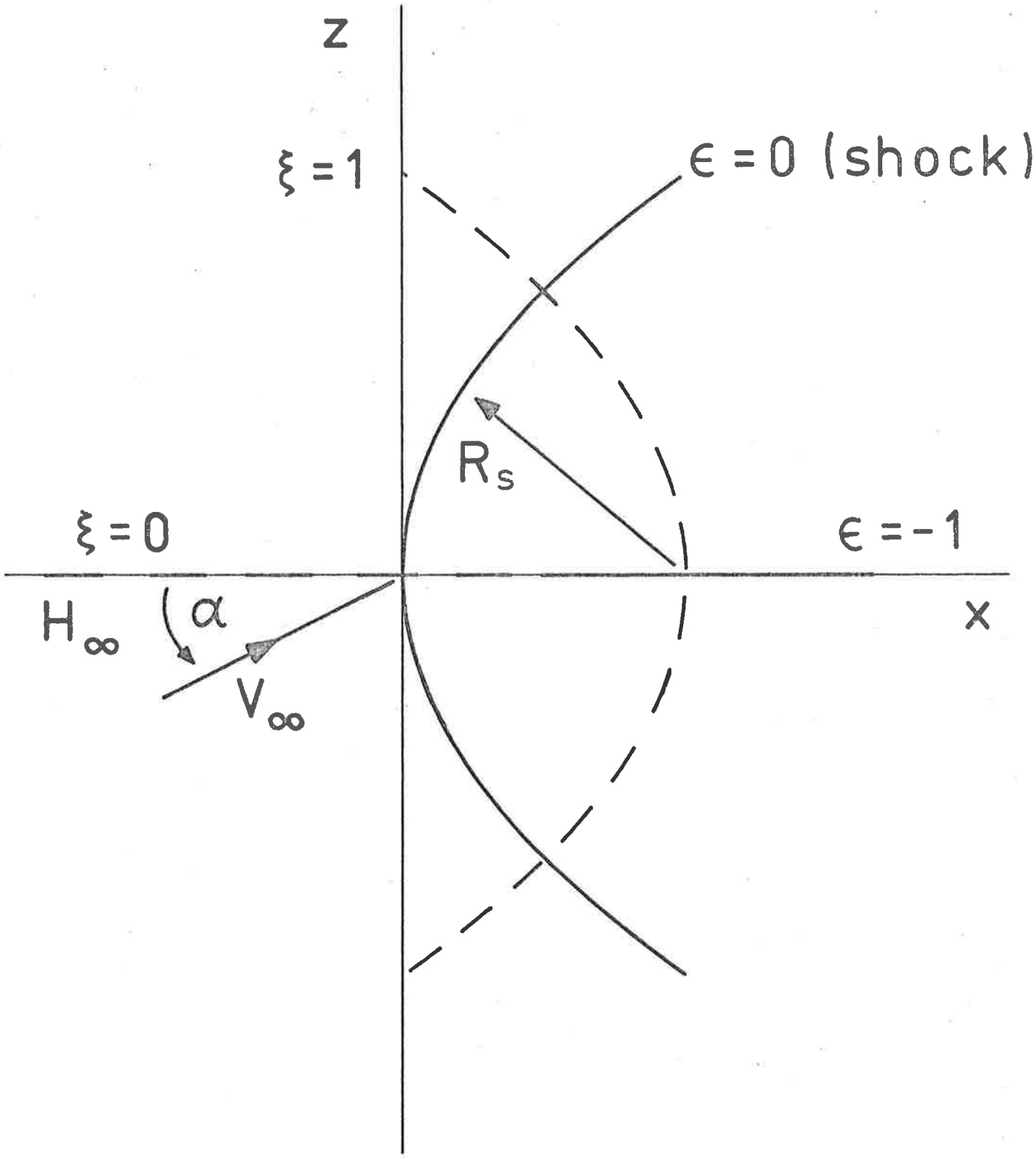

Figure 1.1 The dimensional coordinate system.

Equations (1.1) are now transformed to the coordinate system of Van Dyke (1958b). The shock is assumed to be a conic-section of the form

$$z^2 = 2x - Bx^2 \ ,$$

where B is a measure of the shock bluntness. (Thus $B = 0$ describes a parabola, $B = 1$ a circle, *etc.*) The new orthogonal curvilinear coordinate system is defined by the relations

$$x = \begin{cases} \frac{1}{B}\{1 - [(1 - B\xi^2)(1 + 2B\varepsilon + B\varepsilon^2)]^{\frac{1}{2}}\}, & B \neq 0 \\ \frac{1}{2}(\xi^2 - 2\varepsilon - \varepsilon^2) \ , & B = 0 \end{cases}$$

$$z = \xi(1 + \varepsilon) \ .$$

Thus the shock corresponds to the line $\varepsilon = 0$, as shown in Fig. 1.1. Denoting the components of velocity in the ξ- and ε-directions by u and v respectively, equations (1.1) become

$$R^{(2)}(\xi)\{(uu_\xi + H_\xi/F_\infty^2)[C\xi^2 + (1+\varepsilon)^2] - v^2 C\xi\}$$
$$+ R^{(1)}(\varepsilon)\{vu_\varepsilon[C\xi^2 + (1+\varepsilon)^2] + uv(1+\varepsilon)\} = 0 \quad (1.2a)$$

$$R^{(2)}(\xi)\{uv_\xi[C\xi^2 + (1+\varepsilon)^2] + uvC\xi\}$$
$$+ R^{(1)}(\varepsilon)\{(vv_\varepsilon + H_\varepsilon/F_\infty^2)[C\xi^2 + (1+\varepsilon)^2] - u^2(1+\varepsilon)\} = 0 \quad (1.2b)$$

$$R^{(2)}(\xi)\{C\xi Hu + [C\xi^2 + (1+\varepsilon)^2](Hu)_\xi\}$$
$$+ R^{(1)}(\varepsilon)\{(1+\varepsilon)Hv + [C\xi^2 + (1+\varepsilon)^2](Hv)_\varepsilon\} = 0 \ , \quad (1.2c)$$

where

$$C = 1 - B$$

and

$$R^{(1)}(\varepsilon) = [1 + 2B\varepsilon + B\varepsilon^2]^{\frac{1}{2}} \qquad (1.3a)$$

$$R^{(2)}(\xi) = [1 - B\xi^2]^{\frac{1}{2}} \ . \qquad (1.3b)$$

Equations (1.2a) and (1.2b) are the ξ- and ε-momentum equations, and equation (1.2c) is the mass continuity equation.

The conservation of mass and momentum upon crossing the shock results in the following conditions at $\varepsilon = 0$:

$$H = \tfrac{1}{2}([1 + 8F_\infty^2 \sin^2\theta]^{\frac{1}{2}} - 1) \qquad (1.4a)$$

$$v = - \frac{2\sin\theta}{[1+8F_\infty^2\sin^2\theta]^{\frac{1}{2}} - 1} \qquad (1.4b)$$

$$u = \cos\theta \ , \qquad (1.4c)$$

where θ is the angle between the shock and the free-stream velocity vector, measured anti-clockwise from the latter. Thus

$$\sin\theta = \frac{-\xi \sin\alpha + [1-B\xi^2]^{\frac{1}{2}}\cos\alpha}{[1+C\xi^2]^{\frac{1}{2}}} \ .$$

Equations (1.4) may be obtained from Wehausen and Laitone (1960).

Once the functions u,v and H have been determined from equations (1.2) and (1.4), the streamfunction ψ is obtained by integrating

$$\psi_\varepsilon = \left[\frac{C\xi^2+(1+\varepsilon)^2}{1+2B\varepsilon+B\varepsilon^2}\right]^{\frac{1}{2}} (Hu) \qquad (1.5)$$

subject to the boundary condition

$$\psi(\xi,0) = \begin{cases} \xi\cos\alpha + \frac{1}{B}([1-B\xi^2]^{\frac{1}{2}}-1)\sin\alpha, & B \neq 0 \\ \xi\cos\alpha - \frac{1}{2}\xi^2\sin\alpha , & B = 0. \end{cases} \qquad (1.6)$$

The $\psi = 0$ streamline is assumed to pass through the shock apex.

1.3 Approximate solution for symmetric flow ($\alpha = 0$)

Before proceeding to investigate the exact solution of the full system of equations (1.2) and (1.4), we first present an approximate solution for the position of the stagnation point at the nose of the body, for the case $\alpha = 0$. This result immediately yields the so-called *standoff distance*, which is the minimum distance between the shock and the body, since for $\alpha = 0$ the standoff distance is simply the distance between the stagnation point and the shock apex.

When $\alpha = 0$, the resulting flow field is symmetric about the line $z = 0$, and so the body streamline is $\psi = 0$. By symmetry, W, U_z and H_z are all zero on $z = 0$, and the stagnation point is thus the point on this line for which $U = 0$. On $z = 0$, equation (1.1a) becomes

$$UU_x + H_x/F_\infty^2 = 0 ,$$

which may be integrated immediately to yield

$$\frac{1}{2}U^2 + \frac{H}{F_\infty^2} = \frac{2(2b^2-3b+3)}{(b-1)^2(b+1)} , \qquad (1.7)$$

where

$$b = (1 + 8F_\infty^2)^{\frac{1}{2}} .$$

The constant on the right hand side of equation (1.7) has been determined from the shock conditions at $z = 0$. The height of water at the stagnation point, H_{stag}, is found by setting $U = 0$ in equation (1.7), resulting in the expression

$$H_{stag} = \tfrac{1}{4} \frac{2b^2 - 3b + 3}{b - 1} . \qquad (1.8)$$

Up to this point, no approximations have been introduced.

To obtain an approximate solution for the position of the stagnation point in the flow field, we consider equation (1.1c) evaluated along $z = 0$:

$$U_x H + U H_x + W_z H = 0 . \qquad (1.9)$$

The quantity W_z is a function of x along $z = 0$, and cannot be determined without reverting to the full system of equations. However, if we suppose W_z to be approximately constant along $z = 0$, then the shock conditions give

$$W_z = \frac{b - 3}{b - 1} . \qquad (1.10)$$

Eliminating H and W_z from equation (1.9), by virtue of equations (1.7) and (1.10), yields the following equation for the determination of U along $z = 0$:

$$a_1 U^2 U_x - a_2 U_x + U^2 - a_3 = 0, \qquad (1.11)$$

with

$$a_1 = 3\left(\frac{b-1}{b-3}\right)$$

$$a_2 = \frac{4(2b^2-3b+3)}{(b-1)(b+1)(b-3)}$$

$$a_3 = \frac{4(2b^2-3b+3)}{(b-1)^2(b+1)} .$$

Equation (1.11) is a non-linear ordinary differential equation which may be integrated by separation of variables to yield

$$a_1 U + \frac{a_1 a_3 - a_2}{2\sqrt{a_3}} \ln\left(\frac{\sqrt{a_3}-U}{\sqrt{a_3}+U}\right) = a_4 - x \ ,$$

where the constant of integration, a_4 , is determined from the shock conditions to be

$$a_4 = \frac{2a_1}{b-1} + \frac{a_1 a_3 - a_2}{2\sqrt{a_3}} \ln\left(\frac{(b-1)\sqrt{a_3}-2}{(b-1)\sqrt{a_3}+2}\right) \ . \qquad (1.12)$$

At the stagnation point x_{stag} , $U = 0$, and consequently

$$x_{stag} = a_4 \ , \qquad (1.13)$$

with the constant a_4 given by equation (1.12).

As the upstream flow approaches the critical speed ($F_\infty = 1$), the shock strength tends to zero and equations (1.8) and (1.13) become

$$H_{stag} \to \frac{3}{2} + 0(F_\infty - 1) \ ,$$

$$x_{stag} \to \frac{9}{4}\left[1 + \frac{1}{\sqrt{3}} \ln\left(\frac{\sqrt{3}-1}{\sqrt{3}+1}\right)\right]\frac{1}{F_\infty - 1} + 0(1) \ ,$$

$$\text{as} \quad F_\infty \to 1 \ .$$

Thus the body moves infinitely far downstream as $F_\infty \to 1$.

In the high speed limit ($F_\infty \to \infty$) , equations (1.8) and (1.13) become

$$H_{stag} \to \sqrt{2} F_\infty + 0(1) \ ,$$

$$x_{stag} \to \frac{1}{\sqrt{2}} F_\infty^{-1} + 0(F_\infty^{-3/2}) \ , \quad \text{as} \quad F_\infty \to \infty \ ,$$

so that the shock layer is of infinite height and infinitesimal thickness for $F_\infty \to \infty$.

1.4 The Series Solution

The dependent variables u, v and H in equations (1.2) are expressed as Taylor-series expansions about the shock apex. For example, the velocity u is written

$$u = \sum_{j=0}^{\infty} \sum_{i=0}^{\infty} u_{ij} \, \xi^i \, \varepsilon^j \ .$$

These equations are then substituted into equations (1.2) to yield a system of three recurrence relations, from which the coefficients u_{ij}, v_{ij} and H_{ij} at any order may be determined as sums of products of lower order coefficients. For example, the ε-momentum equation (1.2b) yields the system

$$\sum_{r=0}^{i} R_r^{(2)} F_{i-r,j}^{(3)} + \sum_{s=0}^{j} R_s^{(1)} F_{i,j-s}^{(4)} = 0 \ , \qquad (1.14a)$$

$$i,j = 0,1,2,\ldots$$

where

$$F_{ij}^{(3)} = \sum_{m=0}^{i} \sum_{n=0}^{j} \{(i-m+1) G_{mn}^{(3)} v_{i-m+1,j-n} + C v_{m-1,n} u_{i-m,j-n}\} \qquad (1.14b)$$

$$F_{ij}^{(4)} = \sum_{m=0}^{i} \sum_{n=0}^{j} \{(j-n+1) G_{mn}^{(4)} v_{i-m,j-n+1} - (u_{mn} + u_{m,n-1}) u_{i-m,j-n}\}$$

$$+ \frac{1}{F_\infty^2} \{(j+1)(C H_{i-2,j+1} + H_{i,j+1}) + 2j H_{ij} + (j-1) H_{i,j-1}\}$$

and

$$G_{mn}^{(3)} = C u_{m-2,n} + u_{mn} + 2u_{m,n-1} + u_{m,n-2} \qquad (1.14c)$$

$$G_{mn}^{(4)} = C v_{m-2,n} + v_{mn} + 2v_{m,n-1} + v_{m,n-2} \ .$$

The terms $R_j^{(1)}$ and $R_i^{(2)}$ are the coefficients in the Taylor-series expansions of the functions $R^{(1)}(\varepsilon)$ and $R^{(2)}(\xi)$ defined in equations (1.3). If any element has a negative subscript, then that element takes the value zero.

The system of recurrence relations thus derived from equations (1.2) was programmed in the FORTRAN language on a CDC CYBER 173 computer, to obtain numerical values of the coefficients. Accumulated roundoff error in the coefficients was not a significant concern, since the programs were written for the DOUBLE PRECISION mode, which provides some 28 significant figures accuracy. In order to minimize the total computing time, several intermediate products (such as $F_{ij}^{(3)}$ and $F_{ij}^{(4)}$ in equations (1.14)) were also stored along with the desired coefficients; consequently the total running time is proportional to the fourth power of the order to which the coefficients are calculated. The coefficients were checked by a separate program which resubstituted them into the original equations and verified that these were satisfied at each order.

To begin the computation, the shock conditions (1.4) are expanded as power-series in ξ, up to a chosen order N. In the case of the depth H, for example, this yields the coefficients $H_{00}, H_{10}, \ldots, H_{N0}$. The first application of the recurrence relations derived from equations (1.2) then yields the coefficients $H_{01}, H_{11}, \ldots, H_{N-1,1}$, the second yields $H_{02}, H_{12}, \ldots, H_{N-2,2}$ and so on. Thus after having applied the recurrence relations N times, a triangular array of coefficients for the variable $H(\xi,\varepsilon)$ is obtained. The series for the streamfunction ψ is then constructed by expressing the

right hand side of equation (1.5) in perturbation series form, and integrating term by term with respect to ε .

As with the supersonic blunt body problem, the series expansions for the dependent variables u,v *etc.* fail to converge at the body due to the presence of a limit line in the physically fictitious upstream region, so an approximate method of analytic continuation is required. Following Schwartz (1975), we shall use Padé fractions for this purpose. The double series are first reduced to single series along lines ξ/ε = constant, by the following rearrangement:

$$H(\xi,\varepsilon) = \sum_{j=0}^{\infty}\sum_{i=0}^{\infty} H_{ij}\,\xi^i\varepsilon^j = \sum_{k=0}^{\infty}\left[\sum_{j=0}^{k} H_{j,k-j}\left(\frac{\xi}{\varepsilon}\right)^j\right]\varepsilon^k \ .$$

This form ensures that the most efficient use is made of our triangular arrays of coefficients. The function H is now of the form

$$H\left(\varepsilon;\frac{\xi}{\varepsilon}\right) = H_0 + H_1\varepsilon + H_2\varepsilon^2 + \ldots + H_{m+n}\varepsilon^{m+n} + O(\varepsilon^{m+n+1}), \tag{1.15}$$

where $m+n = N$, the order to which the coefficients are known. This expression can be recast as an [m/n] Padé fraction

$$[m/n]H\left(\varepsilon;\frac{\xi}{\varepsilon}\right) = \frac{a_0+a_1\varepsilon+a_2\varepsilon^2+\ldots+a_m\varepsilon^m}{1+b_1\varepsilon+b_2\varepsilon^2+\ldots+b_n\varepsilon^n}+O(\varepsilon^{m+n+1}) \ . \tag{1.16}$$

The notation [m/n] refers to a rational fraction having m zeros and n poles in the complex ε-plane. The coefficients a_i , $i = 0,1,\ldots,m$ and b_i , $i = 1,\ldots,n$ are those which make the Taylor series expansion of equation (1.16) agree

with equation (1.15) up to order $m+n+1$. Padé fractions can be calculated conveniently by the epsilon algorithm of Wynn (1966).

To find the body corresponding to a given shock, it is first necessary to locate the stagnation point in the flow field, where $u = v = 0$. The coordinates (ξ,ε) of the point satisfying this condition may be found by the two-dimensional Newton-Raphson iteration

$$\xi_{i+1} = \xi_i - \frac{(uv_\epsilon - vu_\epsilon)_i}{(u_\xi v_\epsilon - v_\xi u_\epsilon)_i}$$

$$\varepsilon_{i+1} = \varepsilon_i - \frac{(uv_\xi - vu_\xi)_i}{(u_\epsilon v_\xi - v_\epsilon u_\xi)_i} \quad ,$$

using Padé fractions to sum the series for u,v and their derivatives. Once the position of the stagnation point is known, the value of the streamfunction and the total water depth H may be found there. The body is then obtained by tracing the stagnation streamline by a Newtonian iteration.

The position of the critical line in the flow field may also be obtained from the power-series solution. If F denotes the Froude number in the shock layer, then the critical line is a contour along which $F = 1$, and is analogous to the sonic line in the gas-dynamic blunt-body problem. From the definition of Froude number, we have

$$F^2 = F_\infty^2 \frac{u^2+v^2}{H} \quad . \qquad (1.17)$$

Thus the critical line may be found by expressing the right hand side of equation (1.17) in perturbation series form, and

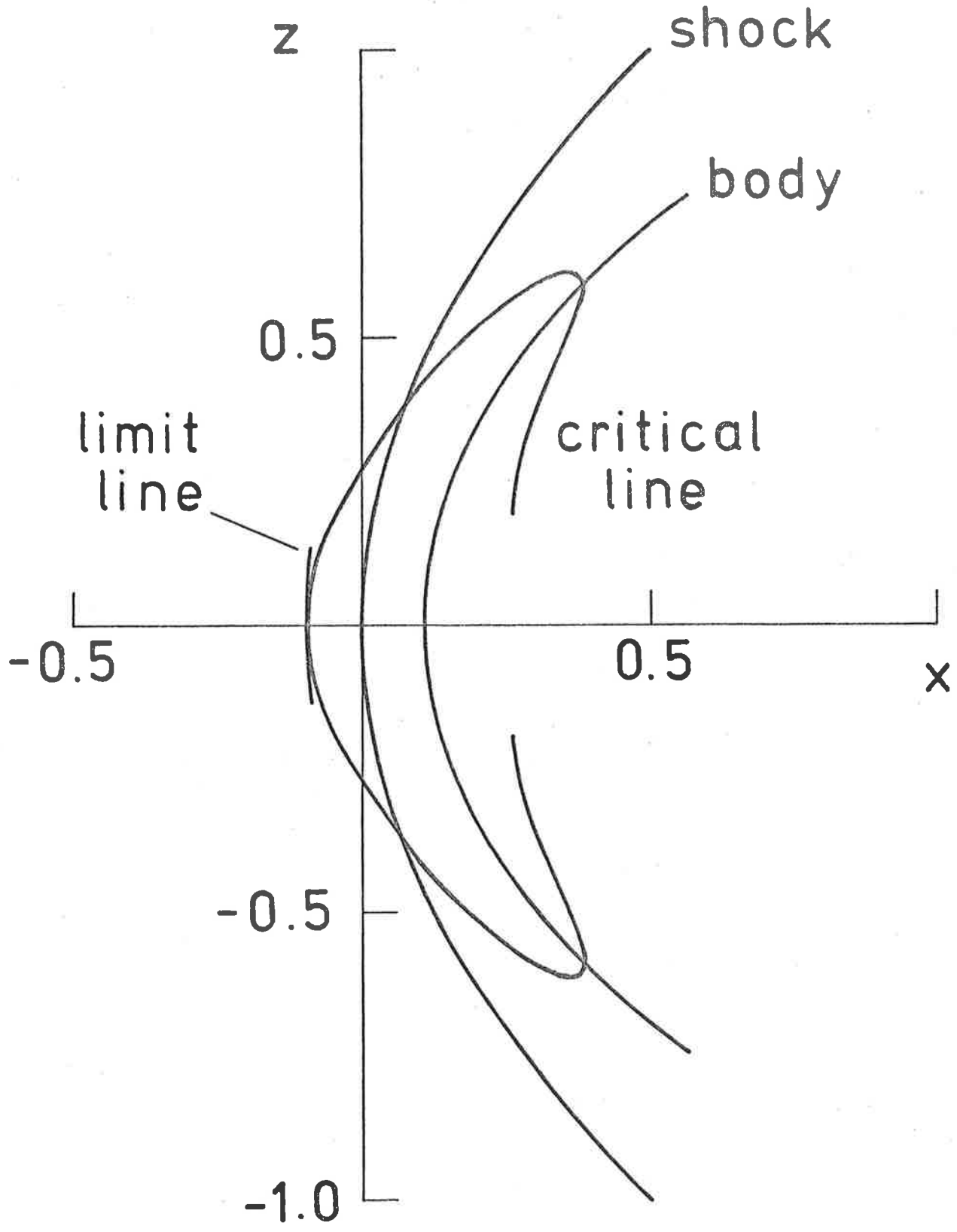

Figure 1.2 The body and flow field for a parabolic shock (B = 0) with $F_\infty = 10$ and $\alpha = 0$.

tracing the contour along which $F^2 = 1$, by a Newtonian iteration. The points where the critical line intersects the shock are known from the shock conditions, and serve as starting points for the tracing.

1.5 Presentation of Results

1.5(a) *Symmetric Case* ($\alpha = 0$).

When the angle α between the free-stream velocity vector and the x-axis is zero, the resultant flow field is symmetric about $z = 0$, and the body streamline is $\psi = 0$. This is illustrated in Fig. 1.2 for the case of a parabolic shock $(B = 0)$ at zero angle of attack to an incident stream with $F_\infty = 10$. Here, the critical line and body streamline were computed as [15/15] Padé approximants, although they are graphically indistinguishable from results produced with much lower order Padé fractions. The critical line has been extended some distance into the body and into the fictitious analytic continuation of the shock layer upstream where it becomes tangent to the upstream limit line shown on the diagram. The position and nature of the limit line were determined by the graphical technique of Domb and Sykes (1957), some examples of which will be given later. As with the supersonic blunt-body problem of gas-dynamics, the upstream limit line is of the square-root type, and is indicative of a fold in the solution surface, similar to that shown by Schwartz (1974a). It may therefore be successfully removed by series reversion; for example if the series for the Froude number F is

$$F(\xi,\varepsilon) = F_0(\xi) + F_1(\xi)\varepsilon + F_2(\xi)\varepsilon^2 + \ldots$$

then inverting the series gives

$$\varepsilon(\xi,F) = \varepsilon_1(F)[F-F_0(\xi)] + \varepsilon_2(F)[F-F_0(\xi)]^2 + \ldots$$

Thus the function $F(\xi,\varepsilon)$, which becomes double-valued at the upstream singular line, is transformed to the single-valued function $\varepsilon(\xi,F)$. Series reversion was used to obtain the critical line in the upstream region, and to check on the accuracy of the body found by Newton's method.

In the blunt body problem of gas-dynamics, the density and ε-direction velocity at the shock both remain finite as the free-stream Mach number is made infinite, provided that the ratio of specific heats, γ, is greater than 1. As a result, the width of the shock layer attains a finite limiting value for infinite free-stream Mach number. This situation is in sharp contrast to the present problem, in which the analogous quantities, H and v, become infinite and zero respectively at the shock as $F_\infty \to \infty$, which may be seen from the shock conditions (1.4). In addition, the width of the shock layer in the present problem becomes zero for infinite free-stream Froude number, a result already anticipated by the approximate solution of Section 1.3.

In Table 1.1, the water depth at the stagnation point, H_{stag}, and the standoff distance, x_{stag}, are presented as functions of the Froude number F_∞. These results were obtained from the 30-th order solution (using [15/15] Padé approximants), for the case of a parabolic shock at zero angle of attack to the upstream flow. Notice that the results for

F_∞	x_{stag}	H_{stag}
2	2.8291935×10^{-1}	2.7276654
3	2.3564145×10^{-1}	4.0882797
10	1.0981844×10^{-1}	1.3919285×10
20	6.6156103×10^{-2}	2.8047687×10
30	4.8572147×10^{-2}	4.2185315×10
10^2	1.8651461×10^{-2}	1.4117401×10^2
10^3	2.6684870×10^{-3}	1.4139638×10^3
10^4	3.4808605×10^{-4}	1.4141866×10^4
10^5	4.2947111×10^{-5}	1.4142111×10^5

TABLE 1.1 Standoff distance and water depth at the stagnation point as functions of F_∞, for parabolic shock at zero angle of attack.

the stagnation depth H_{stag} shown in Table 1.1 agree with the exact result (equation (1.8)) to at least seven significant figures, indicating the degree of convergence of the Padé fractions at the stagnation point.

Fig. 1.3 shows the standoff distance as a function of F_∞, obtained both from the 30-th order series solution, and from the approximate solution of Section 1.3 (equation (1.13)). For large F_∞, the high-order series solution appears to be approaching the result $x_{stag} \sim F_\infty^{-1}$, which is predicted by the approximate solution. However, as $F_\infty \to 1$, the behaviour $x_{stag} \sim (F_\infty - 1)^{-1}$ obtained from the approximate solution is not confirmed by the 30-th order series solution. Instead, the

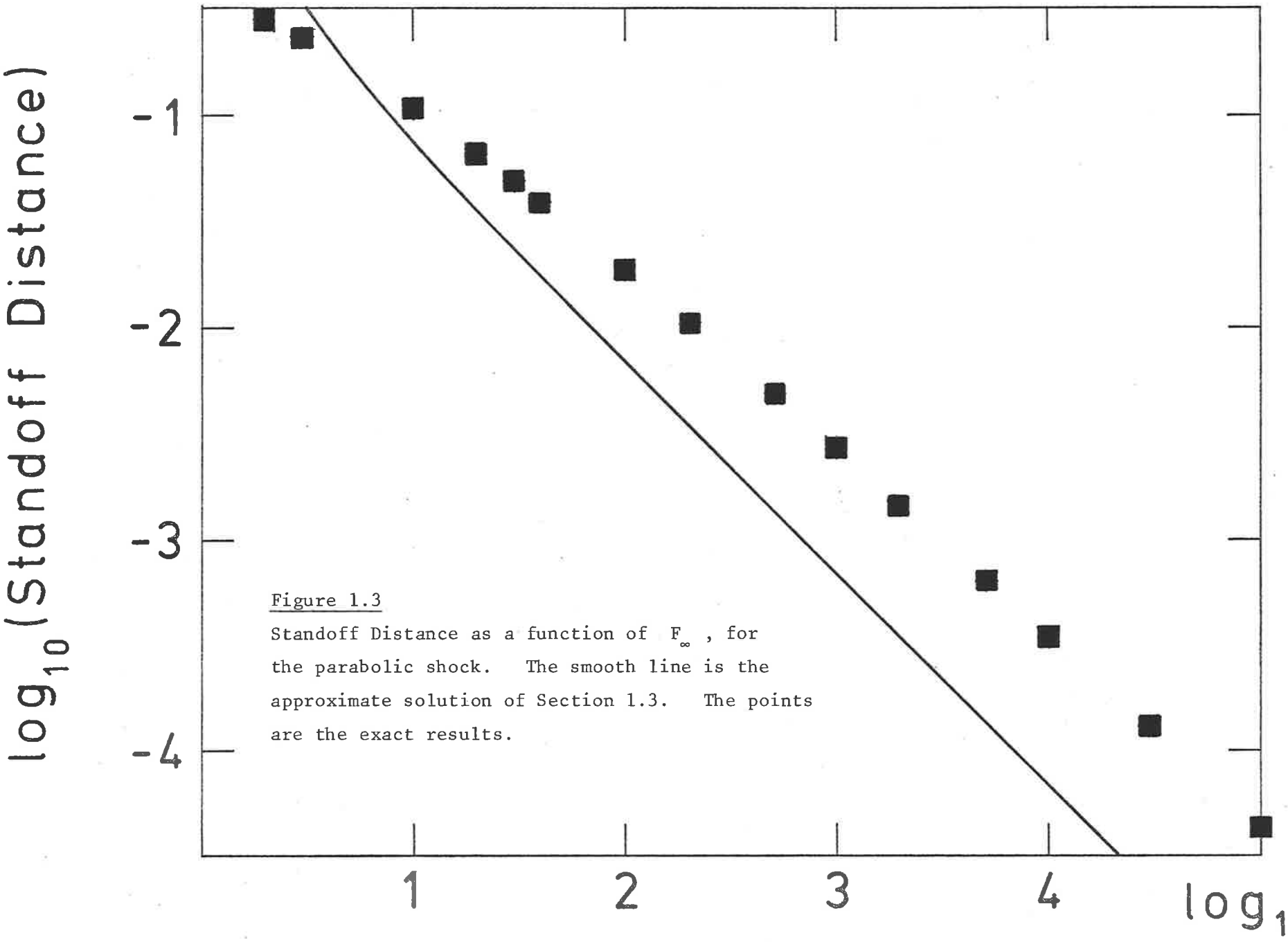

Figure 1.3

Standoff Distance as a function of F_∞ , for the parabolic shock. The smooth line is the approximate solution of Section 1.3. The points are the exact results.

accurate results tend to suggest that the standoff distance may possibly remain finite as $F_\infty \to 1$.

1.5(b) *Asymmetric Case* ($\alpha \neq 0$).

We now consider those situations in which the flow-field is asymmetric, resulting from a non-zero angle of attack α between the free-stream velocity vector and the x-axis. The results for five different test cases are summarized in Table 1.2.

As described in Section 1.1, the power-series solution technique was used by Schwartz (1975) in the blunt-body problem of gas-dynamics to establish conclusively that the maximum entropy streamline which intersects the shock at right angles does not wet the body in asymmetric flows, and may lie either to the windward or the leeward side of the stagnation streamline, depending on the magnitude of the shock bluntness parameter B . An analogous situation exists in shallow water flows, as may be seen from Table 1.2. Here, the value of the streamfunction at the body, ψ_{body} , is contrasted with the streamline normal to the shock, ψ_N , by means of the difference $\Delta\psi = \psi_{body} - \psi_N$. Also tabulated is the difference $\Delta\xi$ between the points where these two streamlines intersect the shock, which may be calculated from equation (1.6). As with the gas-dynamic blunt-body problem, the normal streamline ψ_N passes on the upstream side of the stagnation streamline ψ_{body} when $B < 1$ (giving a positive value for $\Delta\psi$ in Table 1.2), and on the leeward side of the stagnation streamline when $B > 1$ ($\Delta\psi$ negative). For a circular shock ($B = 1$), the stagnation streamline and the normal streamline are, of

Case	F_∞	B	α	ψ_N	ψ_{body}	$\Delta\psi$	$\Delta\xi$
1	5	-1	10°	-0.17917636	-0.17169835	0.00747801	0.00736883
2	5	0	10°	-0.17634764	-0.17274315	0.00360449	0.00355081
3	10	2	10°	-0.17106842	-0.17213020	-0.00106178	-0.00104555
4	5	2	10°	-0.17106842	-0.17439424	-0.00332582	-0.00327429
5	2	2	20°	-0.32305966	-0.34863	-0.02557	-0.02390

TABLE 1.2 The normal streamline and the stagnation streamline for the asymetric problem, computed for five different test cases.

course, identical, by virtue of the special symmetry of the shock in this case. Thus the circular shock case serves as a useful check on the accuracy of our results, and we remark that the agreement between ψ_{body} and ψ_N is usually in excess of eight significant figures when $B = 1$.

As the Froude number F_∞ is increased, the stagnation streamline and the normal streamline move closer together, until in the limiting case $F_\infty \to \infty$, they become indistinguishable. This is because the shock layer now has zero thickness, and by equation (1.4b), $v = 0$ throughout. Thus the stagnation point is simply a point on the shock for which $u = 0$, and from equation (1.4c), this is precisely the point where the flow is incident normal to the shock.

In the paper by Forbes and Schwartz (1981), a discussion is given of the results for case 2, a parabolic bow shock wave at 10° to an incident stream with $F_\infty = 5$. The body and critical line are plotted for the 10th, 20th and 30th order solutions, and it is determined that, although the 10th order solution is incapable of yielding the entire critical line, the 20th and 30th order solutions are completely indistinguishable at least over the subcritical region at the nose of the body, indicating that the [10/10] Padé fractions of the 20th order solution have converged sufficiently well to describe the region of interest near the nose of the body.

The results for case 1 are shown in Fig. 1.4, for the 30th order solution. The flow-field produced downstream of the shock is somewhat atypical of flow-fields obtained with other shock shapes, since for this case, the subcritical region on the upstream side of the body apparently extends

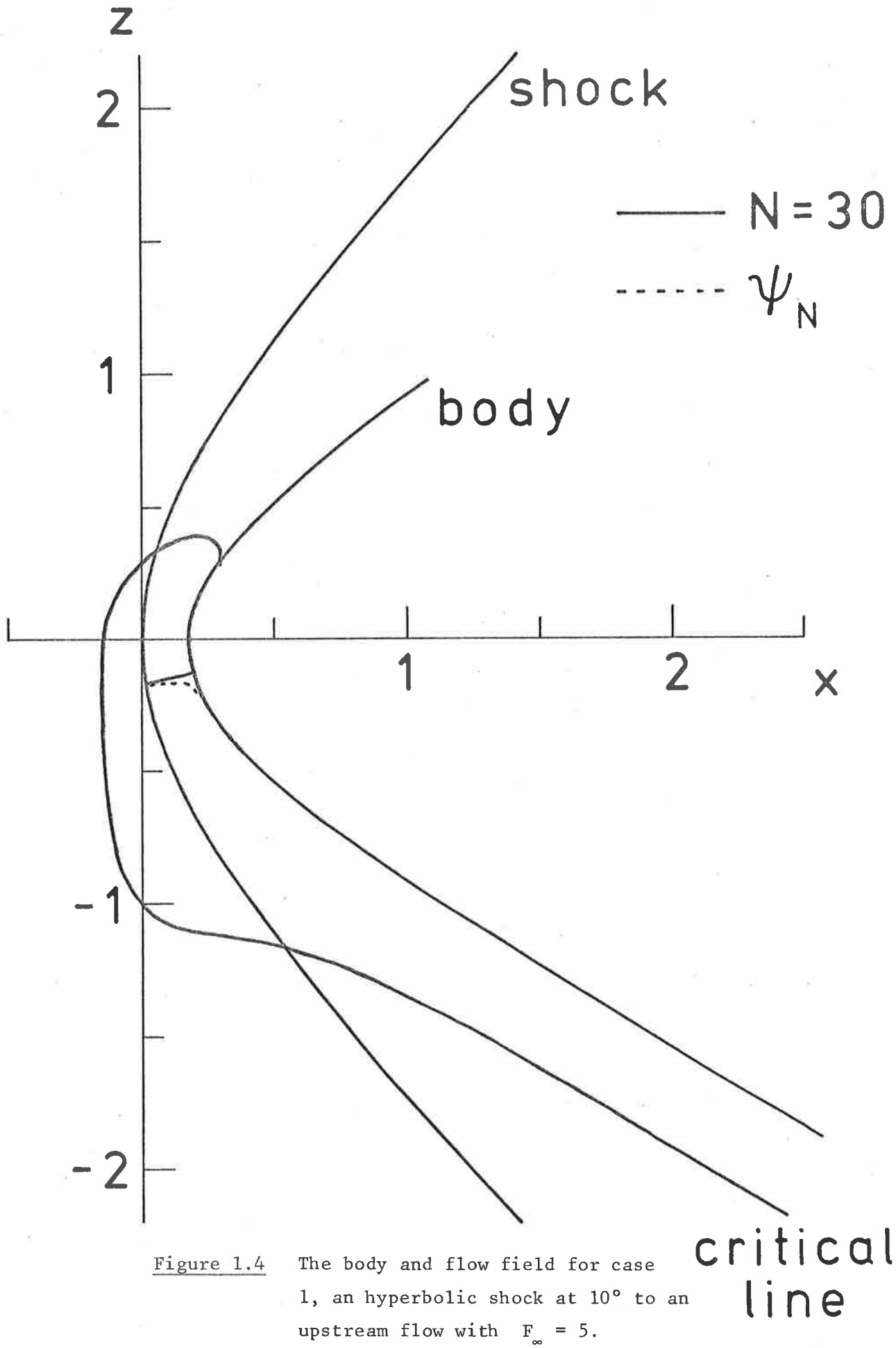

Figure 1.4 The body and flow field for case 1, an hyperbolic shock at 10° to an upstream flow with $F_\infty = 5$.

downstream to infinity, so that the critical line never intersects the body. On the leeward side of the flow, the body and critical line do intersect, however, due to the asymmetry of the flow. The hyperbolic bow shock wave depicted in Fig. 1.4 possibly represents an unrealistic situation, since the shock always makes a non-zero angle with the incident free-stream; consequently the amount of energy required to maintain such a shock is presumably infinite, because the shock strength remains finite even as $z^2 \to \infty$. However, it may nevertheless still be possible for the shock to be locally hyperbolic near the nose of the body in real situations where such flows occur.

In Fig. 1.5 we display the results for case 4, an oblate elliptical bow shock wave at 10° to an incident stream with $F_\infty = 5$. The body, the critical line and the normal streamline are all shown on the diagram, and were obtained with [15/15] Padé approximants formed from a 30th order solution. It is evident that even a solution of this high order is incapable of locating the entire critical line within the shock layer, due to the closeness of certain downstream singular lines to the subcritical region. However, since these singular lines cannot penetrate the subcritical region, by virtue of the fact that the differential equations of motion are of elliptic type there, we expect solutions of higher order to be capable of yielding the critical line up to the point where it intersects the body.

In an attempt to fathom the mathematical structure of the solution for case 4, we have endeavoured to locate all the nearest singular lines, so defining the extent of the

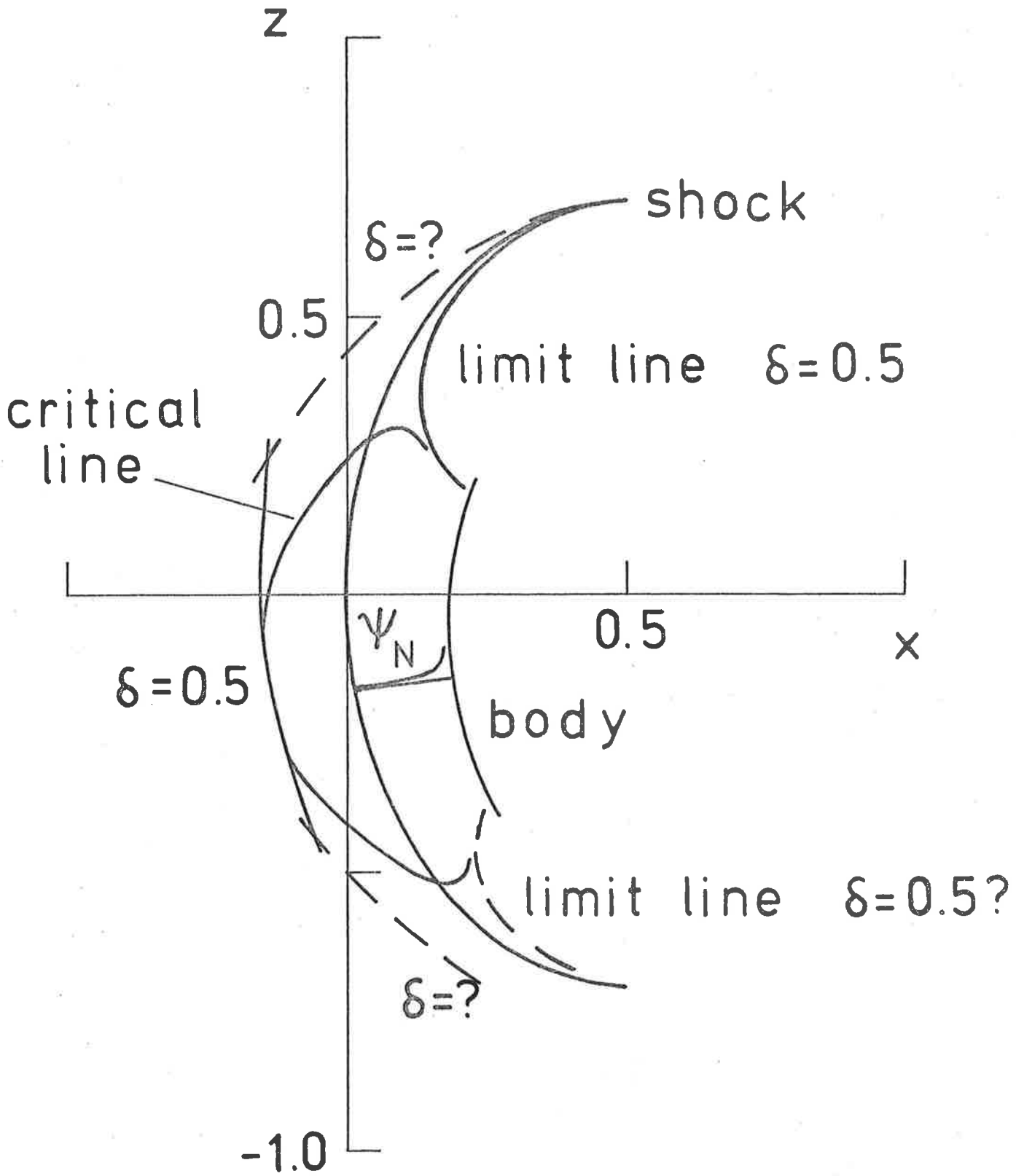

Figure 1.5 The body and flow field supporting an oblate elliptical shock (B = 2) with $\alpha = 10°$ and $F_\infty = 5$. The locations of five different singular lines are also indicated.

region available to any inverse solution technique. To do this, we have examined the function $H(\xi,\varepsilon)$ evaluated along contours ξ/ε = constant , as in equation (1.15). Along these lines, H becomes a function of the single independent variable ε , and accordingly, the coefficients $H_0, H_1, H_2, \ldots$ in the series (1.15) for $H(\varepsilon;\xi/\varepsilon)$ may be examined to find the nature and location of the nearest singularity in the complex ε-plane. To this end, we employ the graphical ratio test of Domb and Sykes (1957). They observed that, for functions of the type

$$f(\varepsilon) = \sum_{n=0}^{\infty} c_n \varepsilon^n = \begin{cases} K(\varepsilon_0-\varepsilon)^{\delta} & , \delta \neq 0,1,2,\ldots \\ K(\varepsilon_0-\varepsilon)^{\delta} \ln(\varepsilon_0-\varepsilon) & , \delta = 0,1,2,\ldots \end{cases} \tag{1.18}$$

a plot of c_n/c_{n-1} against $1/n$ is linear, with vertical intercept $1/\varepsilon_0$ and slope $-(1+\delta)/\varepsilon_0$, because the binomial theorem yields

$$\frac{c_n}{c_{n-1}} = \frac{1}{\varepsilon_0}\left(1 - \frac{1+\delta}{n}\right)$$

for these functions. Thus if the singularity ε_0 of the function $H(\varepsilon;\xi/\varepsilon)$ closest to the origin in the complex ε-plane is of the type (1.18), then a plot of H_n/H_{n-1} against $1/n$ asymptotically approaches a straight line as $n \to \infty$. From the intercept and slope of this line, the radius of convergence ε_0 of the series and the exponent δ of the singularity are estimated.

We have constructed a number of Domb-Sykes plots for the function $H(\varepsilon;\xi/\varepsilon)$ for different values of ξ/ε . Two of these are shown in Fig. 1.6. When $\xi/\varepsilon = -0.6$, the coeffic-

ients H_i in equation (1.15) are all of the same sign, and so the nearest singularity lies on the positive real axis of ε, and represents a point on the upstream limit line. The Domb-Sykes plot indicates that this singularity is of the square-root type ($\delta = 0.5$) and this is confirmed by the fact that it may be successfully removed by series reversion. When $\xi/\varepsilon = -4$, the coefficients H_i have alternating signs, and so the Domb-Sykes plot reveals a singularity downstream of the shock which is again of the square-root type. Two limit lines have been obtained in this fashion, and are indicated in Fig. 1.5. The regular oscillations at lower orders in both the Domb-Sykes plots in Fig. 1.6 are due to the existence of secondary singularities in the function $H(\varepsilon;\xi/\varepsilon)$.

Having thus located the primary singularity ε_0 of the function $H(\varepsilon;\xi/\varepsilon)$ for a range of values of ξ/ε, it is often possible to increase the radius of convergence by mapping the point ε_0 away to infinity using an Euler transformation. This is achieved by changing to the new independent variable

$$\bar{\varepsilon} = \frac{\varepsilon}{\varepsilon-\varepsilon_0} .$$

Domb-Sykes plots may now be constructed for the new function $\bar{H}(\bar{\varepsilon};\xi/\varepsilon)$ to locate secondary singularities occurring in the complex $\bar{\varepsilon}$-plane.

The Domb-Sykes plots constructed for the function $\bar{H}(\bar{\varepsilon};\xi/\varepsilon)$ from the 30-th order solution are in general imprecise, so that the position of the new singularity can only be obtained very approximately. The dashed lines in Fig. 1.5 indicate the

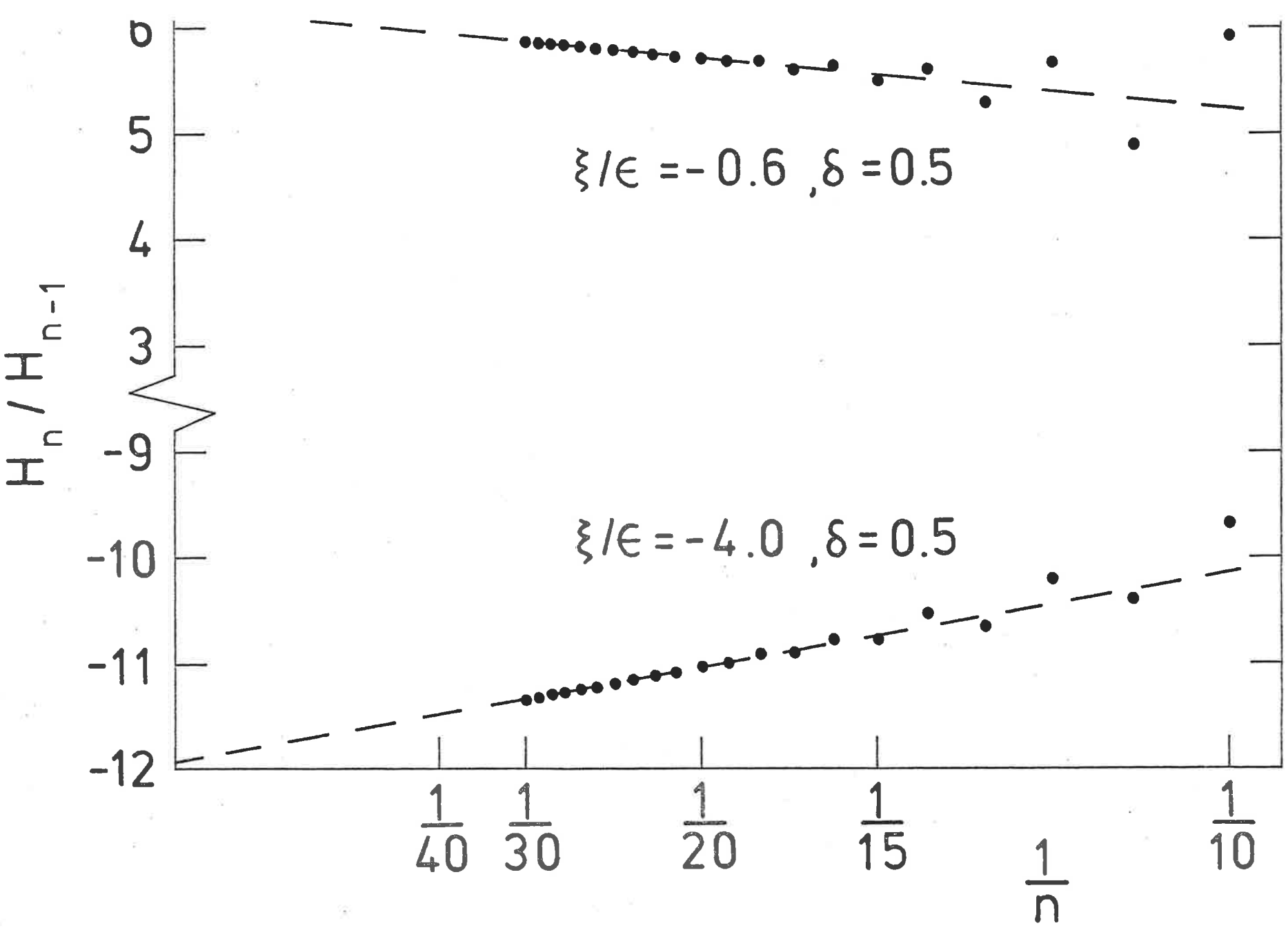

Figure 1.6 Two Domb-Sykes plots constructed from the coefficients of the series for H, for case 4.

suspected locations of three singular lines obtained from these plots. A limit line is expected downstream of the shock on the upstream side of the flow at roughly the position indicated on the diagram. A comparison of Fig. 1.5 with other similar flows tends to suggest that this downstream limit line is most probably of the square-root type, with $\delta = 0.5$. In addition, the Domb-Sykes plots appear to indicate the existence of two upstream limit lines distributed roughly symmetrically about the stagnation streamline, and sketched in Fig. 1.5. The value of the exponent δ along these lines cannot be determined to within acceptable error bounds, although its sign would appear to be negative. It is possible that this exponent may have the approximate value $\delta = - 0.43$ found by Schwartz (1975) for the analogous upstream limit lines in the gas-dynamic blunt-body problem. Note that the limit lines on the leeward side of the flow intersect the shock at the singular point where the shock becomes parallel to the upstream uniform flow.

Unlike the upstream limit lines which exist only in a physically fictitious flow region, limit lines downstream of the shock occur in a region of physical interest, and indicate the boundary of the region downstream in which the flow variables are analytic. To proceed further downstream it is presumably necessary to postulate some non-analytic behaviour in the flow variables, such as a secondary embedded shock connecting the two regions.

1.6 Summary and Further Remarks

The supercritical shallow-water blunt-body problem has been solved inversely by a power-series coordinate expansion, for shocks which are assumed to be members of a one-parameter family of conic sections. Certain similarities exist between these flows and their gas-dynamic counterparts, although the analogy with gas-dynamics is not exact, since the shock jump conditions are different for the two problems. In particular, in the infinite Froude number limit, the shock layer is of infinitesimal thickness and infinite height, and the normal streamline and body streamline have become indistinguishable, although they are normally separate and distinct for asymmetric flows at finite Froude number.

When $B \geqslant 0$, limit lines, associated with the jump conditions at the shock, are apparently always present downstream and may become very close to the subcritical region at the nose of the body when F_∞ is small and B is large. Unlike their gas-dynamic counterparts, however, the downstream limit lines in the present problem appear to move infinitely far downstream as $F_\infty \to \infty$, when the shock wave is parabolic ($B = 0$). For hyperbolic shocks ($B < 0$), the shock wave is free of singular points, and so the region downstream of the shock evidently does not possess limit lines; in fact, it appears that the subcritical region may extend infinitely far downstream for these cases. However, hyperbolic shocks possibly do not represent a realistic situation, since they presumably require an infinite amount of energy to maintain.

In this chapter, we have discussed only the flow about blunt, three-dimensional obstacles in a shallow stream with a flat, horizontal bottom. In principle, the techniques employed in this chapter may be used to study the flow about such obstacles in a stream with arbitrary smooth bottom topography, although the analogy with gas dynamics would no longer apply. In addition, some difficulty may be encountered with the shock jump conditions, and the choice of realistic shock shapes.

The equations of shallow-water theory are, of course, unlike those of gas dynamics in that they are only an approximation to the full inviscid equations of motion. The work discussed in this chapter therefore reveals two interesting limiting cases where the assumptions of shallow-water theory might not be expected to hold. The first such case is the limit $F_\infty \to \infty$, where the shock layer degenerates to an infinitely thin water jet of infinite height in front of the body. Whilst the assumption of zero vertical velocity implicit in shallow-water theory is clearly violated, the predictions of this theory are, however, not entirely unrealistic. Indeed, a very thin jet of great height in front of the body is actually observed in such situations, although this jet usually curves down and re-enters the upstream portion of the flow. In addition, we might expect such a jet to be significantly influenced by viscosity and surface tension.

The second situation in which shallow-water theory would appear to be inadequate is the limit $F_\infty \to 1$. In this case, the standoff distance becomes large and the shock strength

small, so that the bore itself might perhaps become of the undular type, being followed by a train of non-linear downstream waves. Although the analysis of this situation would undoubtedly be of great theoretical and practical interest, the complexity of this problem apparently places it beyond the range of present techniques (and computers). Specifically, the surface waves that are expected to appear within the shock layer as $F_\infty \to 1$ cannot be described by the simple shallow-water theory of this chapter, and so some higher order theory must be developed in which surface displacements on a scale comparable to the water depth are taken into account. This would appear to be a difficult task, and it may even be necessary to return to the full three-dimensional inviscid equations of motion. In either case, it would no longer seem possible to impose boundary conditions at an assumed shock wave upstream of the body, since the very concept of a shock discontinuity within the flow is only valid within the context of the shallow-water theory. The higher order theories needed to describe the formation of waves in the region near the body would require detailed knowledge of the shock *structure* if boundary conditions are to be imposed at the shock; since this information is not known à *priori*, being sought as part of the solution, some attempt would ultimately have to be made to impose uniform flow conditions at upstream infinity.

Rather than attempt to treat this difficult problem further, we instead retreat to the somewhat simpler, and not entirely unrelated, consideration of *two-dimensional* flows about submerged bodies. In the remaining chapters of this thesis,

the non-linear surface waves generated by various types of irregularity in the bed of a stream will be discussed.

CHAPTER TWO

TWO-DIMENSIONAL GRAVITY FLOW ABOUT A SUBMERGED SEMI-CIRCLE

2.1 Introduction

In this chapter, we consider the flow under gravity of an incompressible, inviscid fluid in a channel, affixed to the bottom of which is a semi-circular cylinder lying across the channel bed at right angles to the oncoming flow. The flow is steady with uniform flow conditions far upstream, and may be regarded as two-dimensional, since there is no variation in flow conditions across the channel. The solution to this problem may be of interest in determining the forces on a cable lying on the ocean floor, for example. It may also serve to indicate the mechanisms by which waves are generated by submerged bodies, such as submarines.

The motion of concentrated singularities beneath a free surface is an old problem in fluid mechanics, and is closely related to the topic of this chapter. Havelock (1927) calculated a linearized solution to the problem in which a dipole moves with constant velocity beneath the surface of an infinitely deep fluid at rest. He then assumed that, at some first order of approximation, his solution would also describe the flow about a circular cylinder beneath the surface of an infinitely deep fluid, as well as the flow about a semi-circular obstruction on the bottom of an horizontal canal. Various

other authors have presented similar linearized solutions to problems of this type. The book by Kochin, Kibel' and Roze (1964) contains detailed and elegant solutions for the cases of a point vortex, a point source and a dipole moving beneath the surface of an infinitely deep fluid. The corresponding solutions for a fluid of fixed finite depth are given in Wehausen and Laitone (1960).

The Havelock solution to the motion of a dipole beneath a free surface was reconsidered by Tuck (1965). He showed that the "body" produced in the fluid by the dipole is in fact not closed, so that the front and back stagnation points lie on different streamlines. Thus a linearized solution to the present problem, to be discussed in Section 2.3, will necessarily differ from Havelock's, since we shall require a closed body at all orders of approximation. In addition, Havelock's solution results in a dispersion relation which describes waves in an infinitely deep fluid, while the dispersion relation resulting from our linearized solution describes a fluid of finite depth. This fact is responsible for the existence of a second class of solutions to our problem, when the fluid flow is supercritical, which are symmetric about the semi-circle and possess no waves.

Recently, a number of investigators have sought to retain the free-surface condition in its exact non-linear form when dealing with problems of this type. Von Kerczek and Salvesen (1977) present a numerical solution to the two-dimensional steady problem in which waves are produced on the surface of a stream of finite depth by a given pressure distribution

on the surface. The numerical method they employ is one which they have successfully used in the solution of other similar problems, and consists of placing a finite-difference grid over the region of interest in the physical plane, and then iterating to find the location of the free surface such that all the flow equations and boundary conditions are satisfied. Haussling and Coleman (1977) describe the numerical solution of time-dependent potential flow problems of great generality by a boundary-fitting technique, in which a curvilinear coordinate system is generated numerically, so that lines in the new coordinate system correspond to physical boundaries. Shanks and Thompson (1977) show how this technique may be used to solve free-surface problems numerically in which time-dependence and even viscosity are included.

The problem of flow about a triangular wedge on the bed of a stream has been investigated by Aitchison (1979)*, using a variable finite-element technique. For subcritical flows, solutions possessing a train of downstream waves are obtained, while for supercritical flows, the surface is free of waves. In addition, a family of solutions has been obtained for which the flow is subcritical on one side of the wedge and super-critical on the other side.

In the present study, we treat the physical coordinates as the unknowns of the motion, with the velocity potential and streamfunction as the independent variables. Thus the location of the free surface in the inverse plane is now known. The problem is then solved by a boundary-integral technique, so that points in the numerical scheme need only be placed on

---

* - I express my appreciation to Dr. J.M. Aitchison for making a copy of her report available.

the boundaries, rather than throughout the entire fluid region. In addition, conformal mapping is used to transform the channel bed into a straight line; consequently, the boundary-integral formulation of the problem involves only values of the flow variables at the free surface, with the bottom condition being satisfied automatically. As a result, it is now only necessary to place points in the numerical scheme at the free surface. This formulation ensures maximum computational efficiency when obtaining non-linear free-surface profiles.

2.2 Formulation of the Problem

We consider the steady, two-dimensional potential flow of an inviscid, incompressible fluid. Far upstream, the flow is uniform, with constant velocity c and fixed depth H. The fluid is subject to the downward acceleration of gravity g, and the radius of the disturbing semi-circle is R_c.

The problem may immediately be non-dimensionalized with respect to the velocity c and depth H. The velocity potential ϕ and streamfunction ψ are normalized with respect to the product cH. The channel bottom is taken to be the $\psi = 0$ streamline, so that the free surface is $\psi = 1$. There is thus a two-parameter family of solutions to this problem, dependent upon the depth-based Froude number

$$F = \frac{c}{(gH)^{\frac{1}{2}}}$$

and the dimensionless circle radius

$$\alpha = \frac{R_c}{H} .$$

A sketch of the non-dimensional coordinate system is given in Fig. 2.1.

The irrotationality and incompressibility of the fluid in the interior is expressed by the usual Cauchy-Riemann equations

$$\begin{aligned} \phi_x &= \psi_y \\ \phi_y &= -\psi_x , \end{aligned} \tag{2.1}$$

where the subscripts denote partial differentiation. The condition of no flow normal to the bottom $y = h(x)$ may be written

$$uh_x = v \quad \text{at} \quad y = h(x), \tag{2.2}$$

where

$$h(x) = \begin{cases} (\alpha^2 - x^2)^{1/2}, & |x| \leqslant \alpha \\ 0 , & |x| > \alpha \end{cases}$$

and u and v are the horizontal and vertical components of velocity respectively. At the free surface of the fluid, we must impose the Bernoulli equation

$$\tfrac{1}{2}F^2(u^2+v^2) + y = \tfrac{1}{2}F^2 + 1 . \tag{2.3}$$

It is convenient at this stage to introduce the complex variables $z = x + iy$ and $f = \phi + i\psi$, and the conjugate complex velocity

$$w = \frac{df}{dz} = u - iv .$$

Now the solution of the above stated problem can be greatly

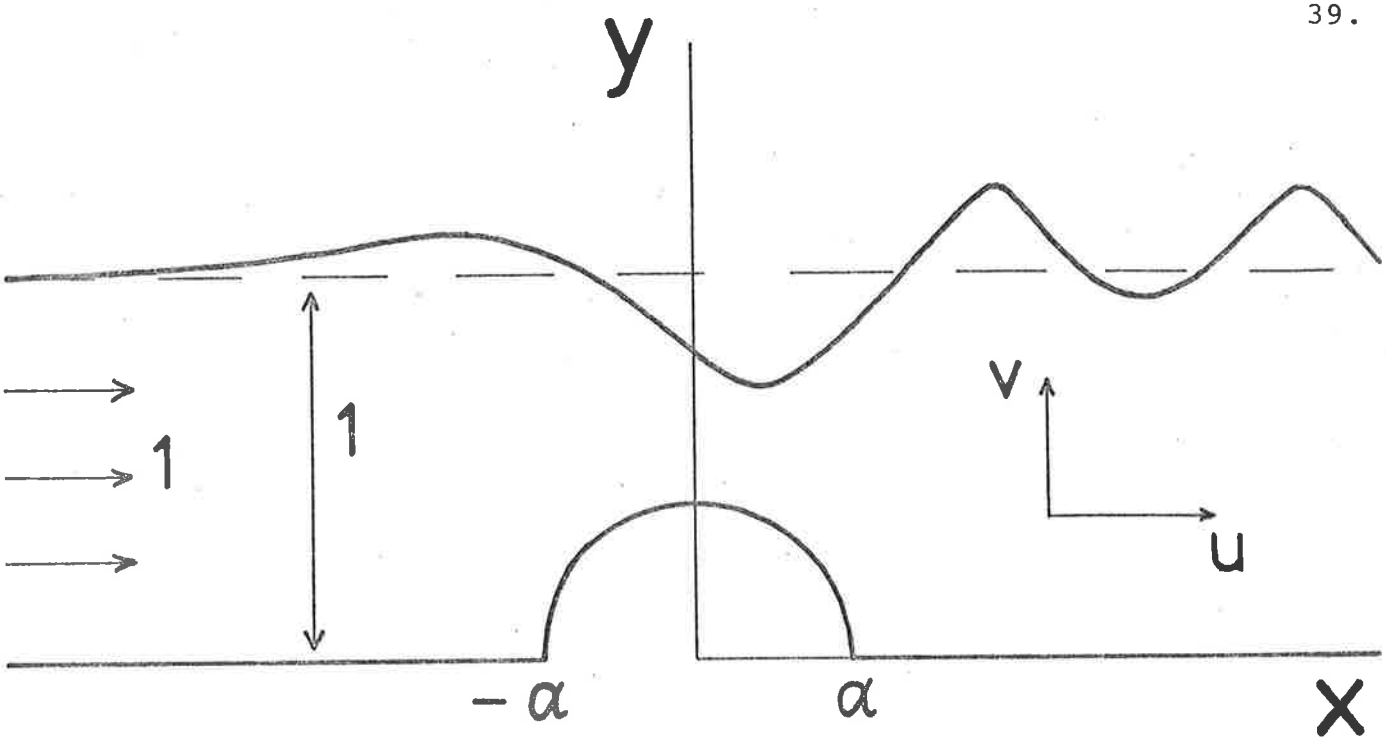

Figure 2.1 The non-dimensionalized problem and coordinate system.

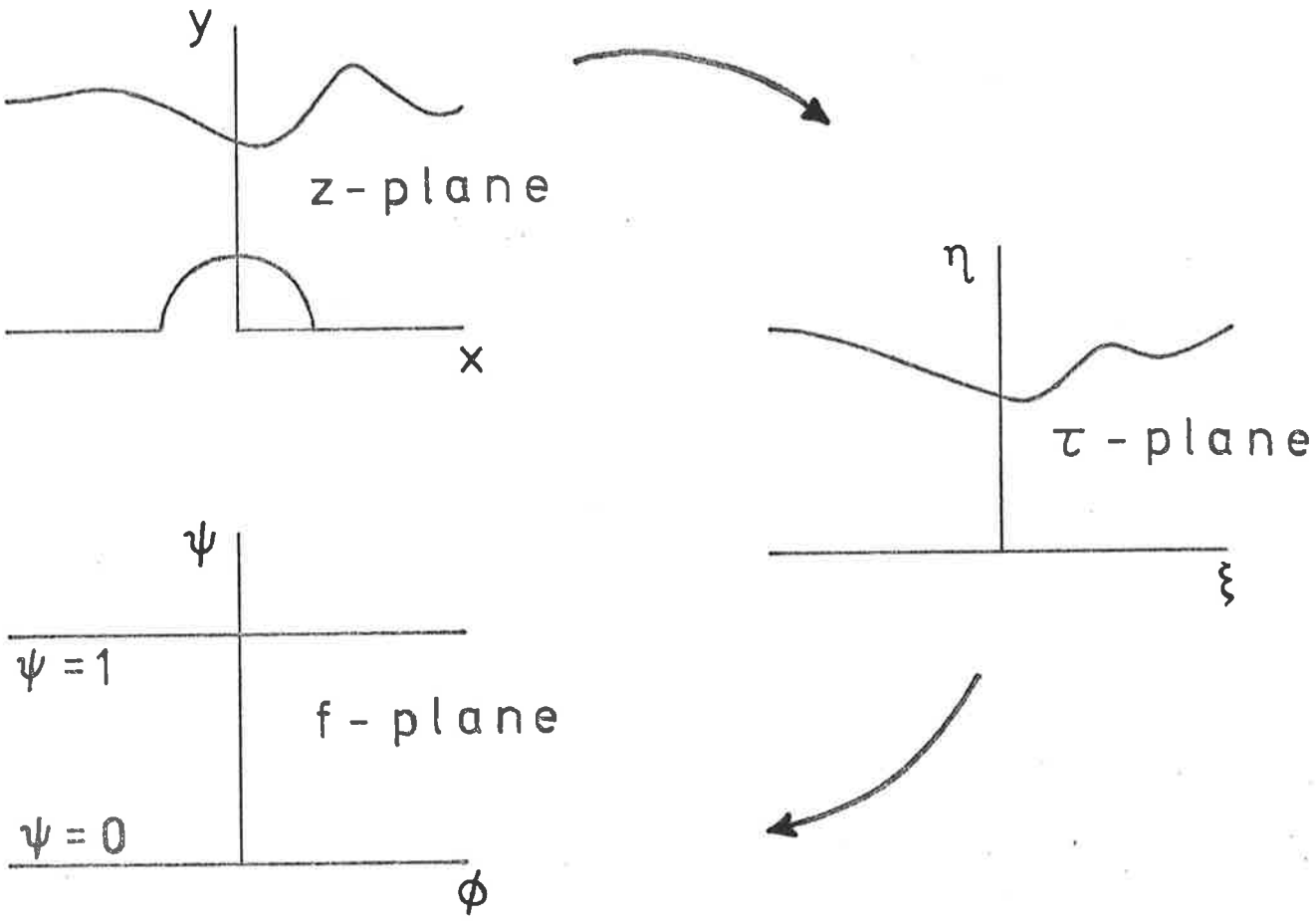

Figure 2.2 The various coordinate systems used in the formulation of the problem.

assisted by the choice of f as independent variable, rather than z. This choice, first suggested by Stokes (1880), has the obvious advantage of removing the difficulty associated with the free-surface condition, since, although the location of the surface is unknown in the z-plane, it has the *known* location $\psi = 1$ in the f-plane. However, we note that the Jacobian of the transformation from the z-plane to the f-plane becomes zero at the two stagnation points on the semi-circle. These points would thus map into singularities in the f-plane. This undesirable situation may be avoided by first mapping the z-plane into a τ-plane in which the bottom streamline is a straight line, free of singular points. The mapping required is the familiar Joukowski transformation

$$\tau = \tfrac{1}{2}\left(z + \frac{\alpha^2}{z}\right) ,$$

where the new variable τ is written as $\tau = \xi + i\eta$. Fig. 2.2 shows the mappings involved in the formulation of this problem.

By defining a new τ-plane conjugate velocity

$$W = \frac{df}{d\tau} = U - iV ,$$

we may transform the z-plane equations (2.1) - (2.3) into the τ-plane. Thus we seek an analytic function $f(\tau)$ satisfying the bottom condition

$$V = 0 \quad \text{on} \quad \eta = 0 ,$$

and the appropriately transformed Bernoulli equation at the free surface.

As there are now no singular points either within the fluid or on the fluid boundaries in the τ-plane, we may interchange the roles of τ and f. In the f-plane, we seek an analytic function $\tau(f)$ satisfying the bottom condition

$$\eta = 0 \quad \text{on} \quad \psi = 0 \quad . \tag{2.4}$$

The final form of the Bernoulli equation in the f-plane is

$$\frac{1}{8}F^2 \frac{(z^2-\alpha^2)(\bar{z}^2-\alpha^2)}{(z\bar{z})^2(\xi_\phi^2+\eta_\phi^2)} + \mathrm{Im}\{z\} - 1 - \tfrac{1}{2}F^2 = 0$$

$$\text{on} \quad \psi = 1, \tag{2.5}$$

where $z(\tau)$ is found from

$$z = \tau + (\tau^2-\alpha^2)^{1/2} \tag{2.6}$$

and the bars signify complex conjugation. The branch of the radical in equation (2.6) is chosen so that $z = 2\tau$ when $\alpha = 0$.

We now derive an integral equation relating the real and imaginary parts of $\tau'(f)$ along the free surface $\psi = 1$. Consider the function

$$\chi(f) = \frac{d\tau}{df} - \tfrac{1}{2} \quad .$$

This function is analytic in the f-plane strip $0 \leqslant \psi \leqslant 1$ and vanishes as $\phi \to -\infty$. Far downstream, its mean value is zero. By the bottom condition (2.4), we have $\mathrm{Im}\{\tau'(f)\} = 0$ on $\psi = 0$; consequently, the strip $0 \leqslant \psi \leqslant 1$ may be extended by reflection about $\psi = 0$ to form the augmented section $-1 \leqslant \psi \leqslant 1$. The satisfaction of the bottom condition (2.4) then requires that values of τ' on the image strip be related to values on the true strip by the formula

$$\tau'(\bar{f}) = \bar{\tau}'(f) \ . \qquad (2.7)$$

When Cauchy's Integral Theorem is applied to the function $\chi(f)$ on a rectangular path consisting of the free surface $\psi = 1$ and its image $\psi = -1$ connected by vertical lines at $\phi \to \pm \infty$, we obtain

$$\chi(f) = \frac{1}{2\pi i}\left\{ - \int_{-\infty}^{\infty} \frac{\chi(\theta+i)\,d\theta}{\theta+i-f} + \int_{-\infty}^{\infty} \frac{\chi(\theta-i)\,d\theta}{\theta-i-f}\right\} \ , \qquad (2.8)$$

for points $f = \phi + i\psi$ within the path of integration. We now let f become a point on the true free surface, so that $f = \phi + i$. The path of integration is as before, except that the point $f = \phi + i$ is bypassed by a semi-circular path of vanishingly small radius. For points on the free surface, we have

$$\chi(\phi+i) = \frac{1}{\pi i}\left\{ - \int_{-\infty}^{\infty} \frac{\chi(\theta+i)\,d\theta}{\theta-\phi} + \int_{-\infty}^{\infty} \frac{\chi(\theta-i)\,d\theta}{\theta-\phi-2i}\right\} \ . \qquad (2.9)$$

The desired relation is obtained by taking the real part of equation (2.9), using (2.7) to eliminate quantities at the image free surface. This yields

$$[\xi_\phi(\phi,1) - \tfrac{1}{2}] - \frac{2}{\pi}\int_{-\infty}^{\infty} [\xi_\theta(\theta,1) - \tfrac{1}{2}]\frac{d\theta}{(\theta-\phi)^2+4}$$

$$= -\frac{1}{\pi}\left\{ \int_{-\infty}^{\infty} \frac{\eta_\theta(\theta,1)\,d\theta}{\theta-\phi} + \int_{-\infty}^{\infty} \frac{\eta_\theta(\theta,1)(\theta-\phi)\,d\theta}{(\theta-\phi)^2+4}\right\} \ . \qquad (2.10)$$

The free-surface profile is thus obtained by solving the Bernoulli equation (2.5) coupled with equation (2.10) and subject to the radiation condition

$$\tau \to \tfrac{1}{2}f \quad \text{as} \quad \phi \to -\infty \,. \tag{2.11}$$

Once the shape of the free surface has been determined, all other flow quantities may be obtained. Of particular interest are the horizontal component of the force acting on unit width of the semi-circular cylinder (the drag) and the vertical component (the lift). We shall use the symbols D and L to denote the drag and lift forces respectively, made dimensionless by reference to the quantity $\rho g H^2$, where ρ is the fluid density. Thus

$$D = \int_{-\alpha}^{\alpha} p\, h'(x)\, dx$$

$$= \tfrac{1}{2}F^2 \int_{-\alpha}^{\alpha} (u^2 + v^2) \frac{x}{(\alpha^2 - x^2)^{1/2}}\, dx$$

and

$$L = \int_{-\alpha}^{\alpha} p\, dx$$

$$= \tfrac{1}{2}F^2 \int_{-\alpha}^{\alpha} (u^2 + v^2)\, dx - \alpha F^2 + \frac{\pi}{2}\alpha^2 - 2\alpha,$$

where p is the pressure on the surface of the semi-circle (in units of $\rho g H$). Transforming these equations into the τ-plane yields

$$D = \tfrac{1}{2}\frac{F^2}{\alpha^2} \int_{-\alpha}^{\alpha} U^2\, \xi (\alpha^2 - \xi^2)^{1/2} d\xi \tag{2.12a}$$

and

$$L = \tfrac{1}{2}\frac{F^2}{\alpha^2} \int_{-\alpha}^{\alpha} U^2 (\alpha^2 - \xi^2)\, d\xi - \alpha F^2 + \frac{\pi}{2}\alpha^2 - 2\alpha \,. \tag{2.12b}$$

In the f-plane, these formulae become

$$D = \tfrac{1}{2}\frac{F^2}{\alpha^2}\int_{\phi_{-\alpha}}^{\phi_{+\alpha}} \frac{\xi(\alpha^2-\xi^2)^{1/2}}{\xi_\phi}\,d\phi \qquad (2.13a)$$

and

$$L = \tfrac{1}{2}\frac{F^2}{\alpha^2}\int_{\phi_{-\alpha}}^{\phi_{+\alpha}} \frac{(\alpha^2-\xi^2)}{\xi_\phi}\,d\phi - \alpha F^2 + \frac{\pi}{2}\alpha^2 - 2\alpha\ , \qquad (2.13b)$$

where the quantities $\phi_{\pm\alpha}$ are the solutions to the equations

$$\xi(\phi_{\pm\alpha},0) = \pm\alpha\ . \qquad (2.14)$$

2.3 The Linearized Solution

In this section, we derive an approximate solution to the equations of motion by assuming that the square of the circle radius, α^2, is a small quantity. This solution is in fact the first-order term in a regular series expansion in the parameter α^2; in principle, the series may be continued to any desired order, although the complexity of the equations to be solved becomes prohibitive for any order greater than the first.

We express the solution $\tau(f)$ as the regular perturbation expansion

$$\tau(f) = \tfrac{1}{2}f + \alpha^2 F_1(f) + O(\alpha^4), \qquad (2.15)$$

and seek to determine the function $F_1(f)$ in the form

$$F_1(f) = \int_0^\infty C(\kappa)\sin(\kappa f)\,d\kappa\ . \qquad (2.16)$$

We observe that equation (2.16) satisfies the bottom condition $\mathrm{Im}\{F_1\} = 0$ on $\psi = 0$. By applying the linearized free-surface condition

$$\mathrm{Re}\left\{\frac{dF_1}{df} + \frac{i}{F^2} F_1\right\} = \frac{1}{2F^2(\phi^2+1)} + \tfrac{1}{2}\frac{1-\phi^2}{(\phi^2+1)^2}$$

$$\text{on } \psi = 1, \qquad (2.17)$$

the real function $C(\kappa)$ is determined to be

$$C(\kappa) = \tfrac{1}{2} \frac{e^{-\kappa}(\kappa + \frac{1}{F^2})}{\kappa\cosh(\kappa) - \frac{1}{F^2}\sinh(\kappa)} \quad .$$

The free-surface condition (2.17) and the assumed form of the solution (2.16) both require that the real and imaginary parts of the function F_1 be odd and even functions of ϕ respectively. However, this condition is only satisfied when $F^2 > 1$, since in this case the function $C(\kappa)$ is non-singular, and so the right hand side of equation (2.16) is well defined. A free-surface profile is predicted which is symmetric about $\phi = 0$ and possesses no waves.

For the critical case $F^2 = 1$, there is no solution, since F_1 becomes unbounded due to a singularity in the function $C(\kappa)$ at $\kappa = 0$.

When $F^2 < 1$, the function $C(\kappa)$ possesses a singularity at $\kappa = \kappa_0$, where κ_0 is the positive real root of the dispersion relation

$$\tanh(\kappa_0) = F^2\kappa_0 \quad , \qquad (2.18)$$

and so the Fourier integral in equation (2.16) fails to exist in the usual sense. It is thus necessary to interpret equation (2.16) as a contour integral in the complex κ-plane, with the path of integration bypassing the pole singularity at κ_0 in a semi-circular path of vanishingly small radius. The function

$\sin(\kappa f)$ appearing in the integrand of equation (2.16) is first written as $\sin(\kappa\phi)\cosh(\kappa\psi) + i\cos(\kappa\phi)\sinh(\kappa\psi)$ and the functions $\cos(\kappa\phi)$ and $\sin(\kappa\phi)$ are recognized as the real and imaginary parts of $e^{i\kappa\phi}$. Thus the solution (2.15) may be written as

$$\xi = \tfrac{1}{2}\phi + \alpha^2\,\mathrm{Im}\left\{\int_0^\infty C(\kappa)\cosh(\kappa\psi)\,e^{i\kappa\phi}\,d\kappa\right\} + O(\alpha^4)$$
$$\eta = \tfrac{1}{2}\psi + \alpha^2\,\mathrm{Re}\left\{\int_0^\infty C(\kappa)\sinh(\kappa\psi)\,e^{i\kappa\phi}\,d\kappa\right\} + O(\alpha^4). \qquad (2.19)$$

Now since waves are expected on the downstream side of the semi-circle, the path of integration in equations (2.19) must be taken to pass beneath the pole singularity at $\kappa = \kappa_0$. Thus the integrals in equations (2.19) may be expressed as the Cauchy Principal Value integral of the same integrand plus πi times the residue of the integrand at $\kappa = \kappa_0$. After then taking the indicated real and imaginary parts in equations (2.19) and recombining these expressions for ξ and η, the solution (2.15) may be written in the form

$$\tau(f) = \tfrac{1}{2}f + \tfrac{1}{2}\alpha^2\left\{\int_0^\infty \frac{e^{-\kappa}(\kappa + \frac{1}{F^2})\sin(\kappa f)\,d\kappa}{\kappa\cosh(\kappa) - \frac{1}{F^2}\sinh(\kappa)}\right.$$
$$\left. + \frac{\pi e^{-\kappa_0}(\kappa_0 + \frac{1}{F^2})\cos(\kappa_0 f)}{(1 - \frac{1}{F^2} + \kappa_0^2 F^2)\cosh(\kappa_0)}\right\} + O(\alpha^4)\,. \qquad (2.20)$$

Far upstream, the two terms within the brackets in equation (2.20) cancel, so that the radiation condition (2.11) is satisfied. Far downstream however, the terms within the brackets reinforce, summing to twice the value of the second term. Thus the limiting form of equation (2.20) downstream is

$$\tau(f) \to \tfrac{1}{2}f + \tfrac{1}{2}\frac{A_1}{\sinh(\kappa_0)}\cos(\kappa_0 f) + 0(\alpha^4) \text{ as } \phi \to +\infty \ , \tag{2.21}$$

where the wave amplitude A_1 is given by

$$A_1 = 2\alpha^2 \frac{\pi e^{-\kappa_0}(\kappa_0 + \frac{1}{F^2})\sinh(\kappa_0)}{(1 - \frac{1}{F^2} + \kappa_0^2 F^2)\cosh(\kappa_0)} \ . \tag{2.22}$$

The free-surface profile is obtained by setting $\psi = 1$ in equation (2.20) and then using equation (2.6) to obtain $z(\tau)$. The surface possesses a regular wave train downstream of the bump, but is free of waves upstream. Far downstream, equation (2.21) yields the free-surface profile

$$y \to 1 - A_1 \sin(\kappa_0 x) + 0(\alpha^4) \quad \text{as} \quad x \to +\infty \ .$$

Note that the wave amplitude A_1 defined by equation (2.22) is twice the value calculated by Lamb (1932, p.410, eq.(9)). In Lamb's theory, a linearized solution to flow over an "arbitrary" bump on the bed of a stream is created from the solution to flow over a sinusoidal bed by Fourier superposition. Yet this solution for the flow over a sinusoidal bed already invokes the assumption that the ratio of the amplitude of these sinusoidal undulations to their wavelength must be a small quantity. Thus Lamb's theory might only be expected to provide reasonable results for smooth disturbances of small elevation above the channel bed and of a length which is of the same order of magnitude as the undisturbed fluid depth. Lamb's theory is evidently not applicable to the semi-circular bump for two reasons; firstly, the presence of stagnation points each side of the semi-circular obstacle apparently

locally violates the assumption in Lamb's theory that the flow may be regarded as a small perturbation to uniform flow, and secondly, both the height and length of the semi-circular bump are small quantities. A consequence of this second point is that the velocity at the top of the semi-circle is approximately *twice* the velocity far upstream (for the bodies treated by Lamb's theory, the two velocities are expected to be roughly equal), which offers at least a crude explanation as to why the amplitude of the downstream waves computed in this section is twice that of the waves computed by Lamb's theory.

The linearized wave drag D is calculated by inverting equation (2.20) to obtain a relation of the form $f = f(\tau)$, and then substituting into equation (2.12a) with $\eta = 0$ $(\psi = 0)$. This results in the classical formula

$$D = \tfrac{1}{4} A_1^2 \left[1 - \frac{2\kappa_0}{\sinh(2\kappa_0)} \right] , \qquad (2.23)$$

which may be found in Lamb (1932, p.415).

The lift force L may similarly be calculated from the linearized solution by inverting equation (2.20) and substituting into equation (2.12b) with $\eta = 0$. This yields

$$L = \frac{5}{3}\alpha F^2 + \frac{\pi}{2}\alpha^2 - 2\alpha - \frac{16}{3}\alpha^3 F^2 \int_0^\infty \frac{e^{-\kappa}(\kappa + \frac{1}{F^2})\kappa \, d\kappa}{\kappa \cosh(\kappa) - \frac{1}{F^2}\sinh(\kappa)} + O(\alpha^5) . \qquad (2.24)$$

2.4 Numerical Methods

2.4(a) *Evaluation of the linearized solution.*

The linearized solution may be evaluated without difficulty from equation (2.20), by first truncating the semi-infinite range of integration to an appropriately large, but finite, range. The singular integral is then evaluated numerically, using Trapezoidal Rule integration, and spacing the abscissae symmetrically about the singularity at $\kappa = \kappa_0$, so that the effect of the singularity may be ignored by virtue of Monacella's (1967) theorem. Equation (2.24) for the linearized lift force is also evaluated in this fashion.

At the free surface, the expressions for ξ and η simplify somewhat, and in fact the integrals may be evaluated in closed form as sums of exponential terms that decay rapidly provided that $\phi \neq 0$. Thus, considerable computational advantages result from exploiting this fact. At the surface, equations (2.19) become

$$\xi(\phi,1) = \tfrac{1}{2}\phi\left(1 + \frac{\alpha^2}{\phi^2+1}\right) + \tfrac{1}{4}\frac{\alpha^2}{F^2}\,\mathrm{Im}\left\{\int_{-\infty}^{\infty} \frac{e^{i\kappa\phi}\,d\kappa}{\kappa\cosh(\kappa) - \frac{1}{F^2}\sinh(\kappa)}\right\} + O(\alpha^4) \qquad (2.25a)$$

and

$$\eta(\phi,1) = \tfrac{1}{2}\left(1 - \frac{\alpha^2}{\phi^2+1}\right) + \tfrac{1}{4}\alpha^2\,\mathrm{Re}\left\{\int_{-\infty}^{\infty} \frac{\kappa e^{i\kappa\phi}\,d\kappa}{\kappa\cosh(\kappa) - \frac{1}{F^2}\sinh(\kappa)}\right\} + O(\alpha^4)\,. \qquad (2.25b)$$

We shall denote the improper integral in equation (2.25a) as I_1 and that in equation (2.25b) as I_2; the interpretation of the singular integrals is exactly as described in Section

2.3, with the path of integration in the complex κ-plane deformed to pass beneath the pole singularities at $\kappa = \pm \kappa_0$, where κ_0 is the real positive solution to the dispersion relation (2.18).

The integrals I_1 and I_2 may be evaluated by the residue theorem, following exactly the same procedure described by Lamb (1932, Art. 245). For example, the imaginary part of the integral I_1 in equation (2.25a) may be written

$$\mathrm{Im}\{I_1\} = \begin{cases} -2\pi \sum_{r=2}^{\infty} \dfrac{e^{m_r\phi}}{(1 - F^2 m_r^2 - \frac{1}{F^2})\cos(m_r)}, & \phi < 0 \\ \dfrac{4\pi\cos(\kappa_0\phi)}{(1 + F^2\kappa_0^2 - \frac{1}{F^2})\cosh(\kappa_0)} & \\ +2\pi \sum_{r=2}^{\infty} \dfrac{e^{-m_r\phi}}{(1 - F^2 m_r^2 - \frac{1}{F^2})\cos(m_r)}, & \phi > 0, \end{cases} \tag{2.26}$$

where the quantity m_r is the appropriate solution to the equation

$$\tan(m_r) = F^2 m_r ,$$

which may be found without difficulty using Newton's method. Note that for $F^2 > 1$, the term involving κ_0 in equation (2.26) vanishes and the sums start at $r = 1$. For $\phi \neq 0$, convergence to ten-figure accuracy is usually obtained by including only three or four terms of the series. When $\phi = 0$ however, the linearized solution at the surface must be evaluated numerically from equation (2.20).

2.4(b) *Solution of the non-linear problem.*

We now consider the numerical solution of the non-linear system of equations (2.5), (2.10) and (2.11) at $N + 1$ equally spaced surface points $\phi_0, \phi_1, \ldots, \phi_N$. The quantities ϕ_0 and ϕ_N are chosen to represent $-\infty$ and $+\infty$ respectively.

The integrodifferential equation (2.10) is first truncated upstream and downstream at the points ϕ_0 and ϕ_N. The error introduced by this process will be discussed in Section 2.5. Now the singularity is subtracted from the Cauchy Principal Value integral, leaving a non-singular integral plus a natural logarithm term. Thus the integrodifferential equation (2.10) takes the approximate form

$$[\xi'(\phi) - \tfrac{1}{2}] - \frac{2}{\pi}\int_{\phi_0}^{\phi_N} [\xi'(\theta) - \tfrac{1}{2}]\frac{d\theta}{(\theta-\phi)^2+4}$$

$$\approx -\frac{1}{\pi}\left\{\int_{\phi_0}^{\phi_N}\frac{\eta'(\theta)-\eta'(\phi)}{\theta-\phi}d\theta + \int_{\phi_0}^{\phi_N}\frac{\eta'(\theta)(\theta-\phi)d\theta}{(\theta-\phi)^2+4}\right\}$$

$$-\frac{1}{\pi}\eta'(\phi)\ln\left(\frac{\phi_N-\phi}{\phi-\phi_0}\right) \quad , \qquad (2.27)$$

where the primes denote differentiation with respect to argument, along $\psi = 1$.

To obtain a numerical approximation to equation (2.27), the functions $\xi'(\phi)$ and $\eta'(\phi)$ at the free surface $\psi = 1$ are represented by the vectors of unknown discrete function values ξ_i' and η_i' $(i = 0,1,\ldots,N)$ at the free-surface points $\phi_0, \phi_1, \ldots, \phi_N$. Equation (2.27) is now discretized in a manner which allows freedom to specify conditions at the first point ϕ_0 in accordance with the radiation condition (2.11). This is achieved by evaluating the integrodifferential

equation (2.27) at the N midpoints $\phi_{k-\frac{1}{2}}$, k = 1,...,N . After discretization, we obtain a matrix system of the form

$$[\xi'_{k-\frac{1}{2}} - \tfrac{1}{2}] - \frac{2}{\pi} \sum_{j=0}^{N} a_{kj} [\xi'_j - \tfrac{1}{2}]$$

$$= - \frac{1}{\pi} \sum_{j=0}^{N} b_{kj} (\eta'_j - \eta'_{k-\frac{1}{2}}) - \frac{1}{\pi} \sum_{j=0}^{N} c_{kj} \eta'_j$$

$$- \frac{1}{\pi} \eta'_{k-\frac{1}{2}} \ell n\left(\frac{\phi_N - \phi_{k-\frac{1}{2}}}{\phi_{k-\frac{1}{2}} - \phi_0}\right) , \quad k = 1,...,N . \qquad (2.28)$$

The coefficients a_{kj} , b_{kj} and c_{kj} are known functions of $\phi_{k-\frac{1}{2}}$ and ϕ_j , and depend upon the quadrature formula used to discretize the integrals. We have used Simpson's Rule for this purpose. The quantities $\xi'_{k-\frac{1}{2}}$ and $\eta'_{k-\frac{1}{2}}$ are now written in terms of values of $\xi'(\phi)$ and $\eta'(\phi)$ at neighbouring whole points ϕ_{k-1} , ϕ_k , ϕ_{k+1} *etc.* by means of a three-point interpolation formula. This interpolation formula must be chosen to be consistent with the parabolae fitted by the Simpson's Rule integration used in obtaining equation (2.28), otherwise unacceptably large errors may result. Equation (2.28) becomes

$$\sum_{j=0}^{N} d_{kj} [\xi'_j - \tfrac{1}{2}] = \sum_{j=0}^{N} e_{kj} \eta'_j , \quad k = 1,...,N . \qquad (2.29)$$

If ξ'_0 and η'_0 are assumed known, equation (2.29) may be inverted to yield the solution

$$\xi'_i = \tfrac{1}{2} + \sum_{j=1}^{N} H_{ij} \eta'_j + H_{i,N+1} [\xi'_0 - \tfrac{1}{2}] + H_{i,N+2} \eta'_0 ,$$

$$i = 1,...,N . \qquad (2.30)$$

In practice, we usually obtain η_0', η_0 and ξ_0 from the linearized solution, and then calculate ξ_0' from the Bernoulli equation (2.5) evaluated at the first point ϕ_0 .

The vectors ξ_i and η_i are now obtained by numerical integration, using Gregory's correction to the Trapezoidal Rule. Thus

$$\xi_i = \xi_0 + \sum_{j=0}^{N} w_{ij}\, \xi_j' \qquad (2.31)$$

$$\eta_i = \eta_0 + \sum_{j=0}^{N} w_{ij}\, \eta_j', \quad i = 1,\ldots,N,$$

where the w_{ij} are appropriate weights.

The Bernoulli equation (2.5) evaluated at each of the N points $\phi_1,\ldots,\phi_N$ yields a system of N non-linear algebraic equations in the N unknowns $\eta_1',\ldots,\eta_N'$, after the functions ξ',ξ and η have all been eliminated using equations (2.30) and (2.31). This system is then solved by a modified Newton iteration scheme. Denoting the pressure at the i-th free-surface point by P_i , we seek to solve

$$P_i(\eta_j') = 0, \quad i,j = 1,\ldots,N.$$

We begin the iteration process with suitable estimates for the unknowns η_j' . These are usually provided by the linearized solution. The estimate $\eta_j'^{(k)}$ at the k-th iteration is updated according to the formula

$$\eta_j'^{(k+1)} = \eta_j'^{(k)} + \Delta_j^{(k)},$$

where the correction step $\Delta_j^{(k)}$ is the solution to the matrix equation

$$\sum_{j=1}^{N} \left[\frac{\partial P_i}{\partial \eta_j'}\right]^{(k)} \Delta_j^{(k)} = - P_i^{(k)} \quad .$$

The elements of the Jacobian matrix $\partial P_i / \partial \eta_j'$ may be obtained either approximately, by replacing the derivatives with finite-difference approximations, or exactly, by differentiation of the functions P_i , $i = 1,\ldots,N$. Of course the solution obtained is unaffected by the method used in obtaining these derivatives, and in general the convergence rates are the same for both methods. However, in marginal cases where convergence of Newton's method is uncertain, the Jacobian matrix must be known accurately, and thus the use of exact derivatives is preferable in these cases.

If at some iteration in the Newton process a worse estimate of the solution is obtained than before, in the sense that $P_{rms}^{(k+1)} > P_{rms}^{(k)}$ where P_{rms} is the root-mean-squared residual pressure

$$P_{rms} = \frac{1}{N}\left(\sum_{i=1}^{N} P_i^2 \right)^{1/2} ,$$

then the correction step $\Delta_j^{(k)}$ is halved and the iteration is repeated. However, if the step $\Delta_j^{(k)}$ has been halved more than a certain specified number of times still with no reduction of P_{rms} over its value at the previous iteration, then the Newton process is stopped and a diagnostic is issued.

The above scheme has usually been found to be quadratically convergent; typically, a converged non-linear solution with $P_{rms} < 10^{-10}$ is obtained from the linearized solution in five iterations. When 131 points are used, the process of obtaining the linearized solution and the converged non-

linear solution requires about three minutes of computing time on a CDC CYBER 173 machine.

For large values of the circle radius α , it is often not possible to obtain a converged non-linear solution using the linearized results as an initial approximation in the Newton scheme. For these cases, a previously-computed non-linear solution is used instead.

2.4(c) *Computation of the non-linear drag and lift.*

The wave drag D and lift L are computed from the converged non-linear free-surface profile using equation (2.8) to generate values of ξ' at points along the bottom $\psi = 0$. These values are then integrated to obtain ξ at the points on the bottom, using the linearized solution result for $\xi(\phi,0)$ at the first point upstream. A cubic spline is then fitted through these values of ξ so that equations (2.14) may be solved for $\phi_{\pm\alpha}$ by Newton's method. Once these quantities are known, the drag and lift are evaluated from equations (2.13) using Simpson's Rule integration.

2.5 Presentation of Results

2.5(a) *Subcritical case.* ($F < 1$)

In Fig. 2.3, the linearized and non-linear solutions for $F = 0.5$, $\alpha = 0.2$ are compared. The linearized free surface possesses a wave-free region upstream of the semi-circular bump, followed by a regular wave train downstream. These general features are confirmed by the non-linear result, although the amplitude of the non-linear waves downstream is

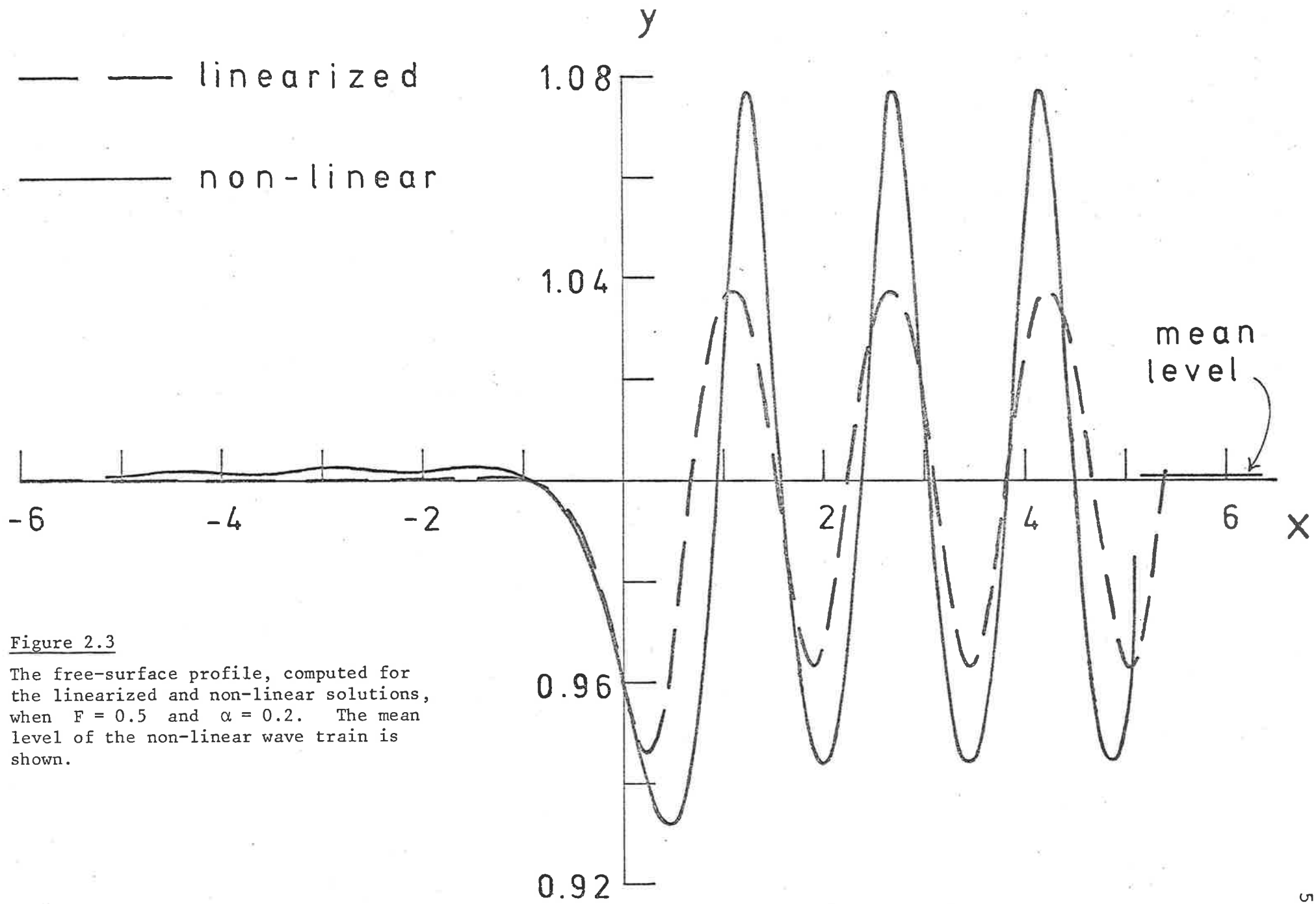

Figure 2.3

The free-surface profile, computed for the linearized and non-linear solutions, when $F = 0.5$ and $\alpha = 0.2$. The mean level of the non-linear wave train is shown.

considerably larger than that predicted by linearized theory. In addition, the non-linear waves are noticeably non-sinusoidal, with narrow crests and broad troughs. The mean height of the free surface downstream of the semi-circle is shown for the non-linear case, and will be discussed in Section 2.6.

For the non-linear waves in Fig. 2.3, the steepness (*i.e.*, the ratio of peak-to-trough wave height to the wavelength) is approximately 0.091. Since Newton's method fails to converge for larger values of the circle radius α, these are the steepest waves that we are presently able to compute at this value of the Froude number. By contrast, the steepness of the Stokes wave of maximum theoretical height at $F \sim 0.5$ is known to be approximately 0.14 (see, for example, Cokelet (1977)). This inability of the present scheme to compute very steep waves is simply a consequence of the relatively small number of free-surface points (about 20 points per wave cycle) to which we are restricted by the storage limits of the computer, and the inclusion of more points at the free surface would doubtless allow waves of much greater steepness to be obtained.

In addition to the downstream waves, the non-linear surface profile in Fig. 2.3 exhibits a small wave train *upstream* of the semi-circle. This is a numerical error caused by the truncation of the integrodifferential equation (2.10) at the point ϕ_0, and the subsequent imposition of the radiation condition (2.11) there. The amplitude of these spurious upstream waves, although extremely small, can be altered by making small changes to the values of η_0, η_0' *etc.*

imposed at the first point ϕ_0 , while the downstream portion of the flow remains unchanged. The presence of the upstream waves in the numerical solution seems to be mainly due to the fact that the imposition of the radiation condition (2.11) at the point ϕ_0 does not correctly account for the local rise in the free-surface level ahead of the semi-circular bump (see Benjamin (1970)). Consequently, it is to be expected that the upstream wave amplitude may be reduced somewhat by increasing η_0 slightly above the value suggested by equation (2.11), and the amplitude of the upstream waves in Fig. 2.3 has indeed been controlled in precisely this fashion. The non-linear surface profile of Fig. 2.3 also exhibits a small error due to the truncation of the integro-differential equation (2.10) at the last point ϕ_N downstream. The effects of this appear to be very slight, however, being confined to the last quarter wavelength or so downstream, and do not affect the rest of the surface profile.

Figs. 2.4 show the dependence of the drag D and lift L upon the circle radius α , for $F = 0.5$. In Fig. 2.4(a) the linearized drag, calculated from equation (2.23), is compared with the drag obtained from the non-linear solution, using equation (2.13a). The linearized and non-linear results agree well up until a circle radius of about 0.12 is reached. Thereafter, non-linear effects dominate, producing a force on the semi-circle which is well in excess of the predictions of linearized theory.

The lift force acting on the semi-circle is shown in Fig. 2.4(b) . This is the force due only to the motion of

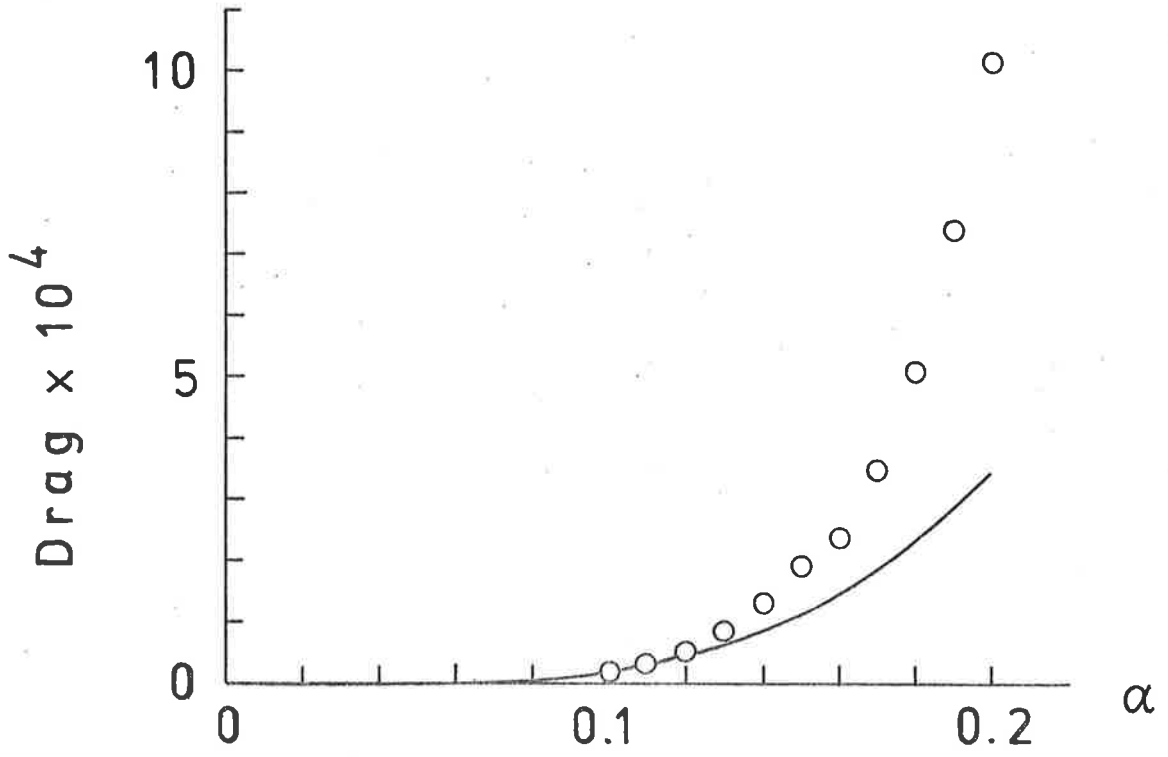

Figure 2.4(a) Wave drag as a function of α, for the linearized and non-linear solutions, when $F = 0.5$.

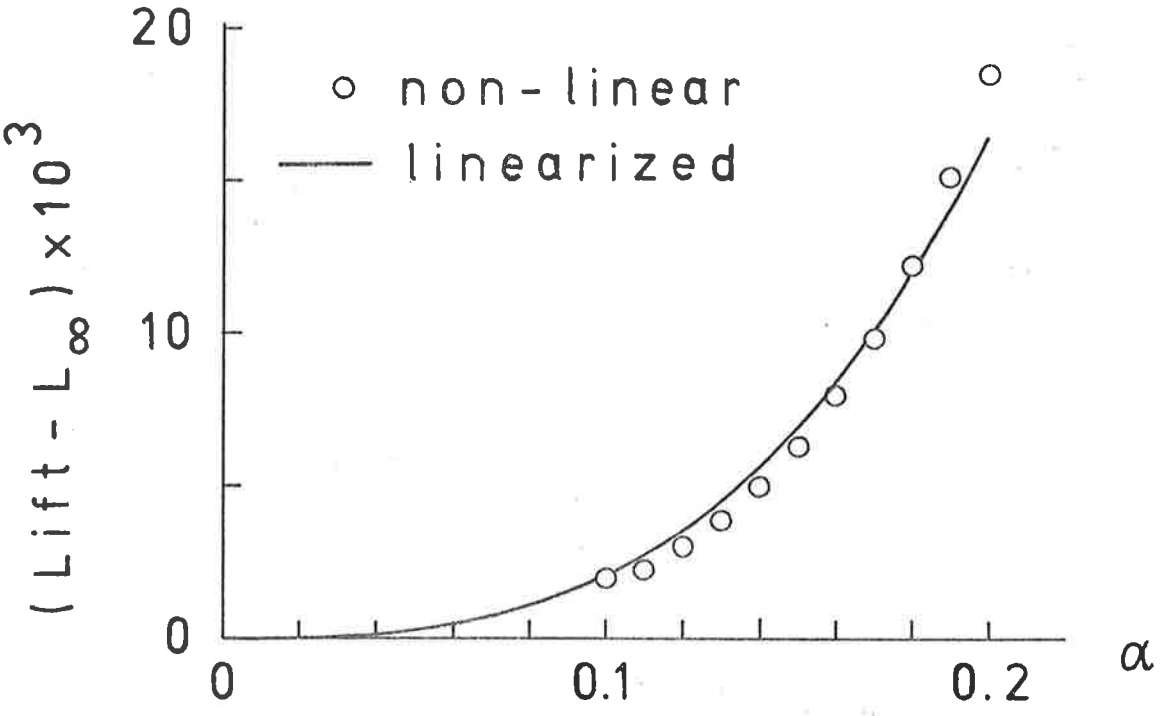

Figure 2.4(b) Lift as a function of α, for the linearized and non-linear solutions, when $F = 0.5$.

the fluid and to gravity, and does not take into account any buoyancy properties that the semi-circle itself may possess. (Thus, instances in which the semi-circular bump is a gas-filled balloon, for example, are not considered.) For convenience, the reference value

$$L_\infty = \frac{5}{3}\alpha F^2 + \frac{\pi}{2}\alpha^2 - 2\alpha$$

has been subtracted from the overall lift force. The quantity L_∞ is the lift that would be observed if the solution were simply $f = 2\tau$ (which is the solution for flow about a circle in a fluid of infinite extent). The linearized lift force, calculated from equation (2.24), appears to provide a reasonable approximation over the entire range of values of α shown in Fig. 2.4(b).

The pressure on the surface of the circle for the non-linear solution is shown as a function of y in Fig. 2.5, for the case considered in Fig. 2.3. The drag and lift forces acting on the semi-circle for this case may be found from Figs. 2.4 ($\alpha = 0.2$). To show more clearly the differences between the pressure distributions on the upstream and downstream portions of the semi-circle, the pressure has been subtracted from the reference value

$$P_\infty = -2\frac{F^2}{\alpha^2}(\alpha^2 - x^2) - (\alpha^2 - x^2)^{1/2} + 1 + \tfrac{1}{2}F^2 ,$$

which is the pressure that would be observed on the surface of the semi-circle if the streamline $\psi = 1$ had the same shape as is obtained for two-dimensional potential flow about a circle in an infinite fluid ($f = 2\tau$). Since P_∞ is

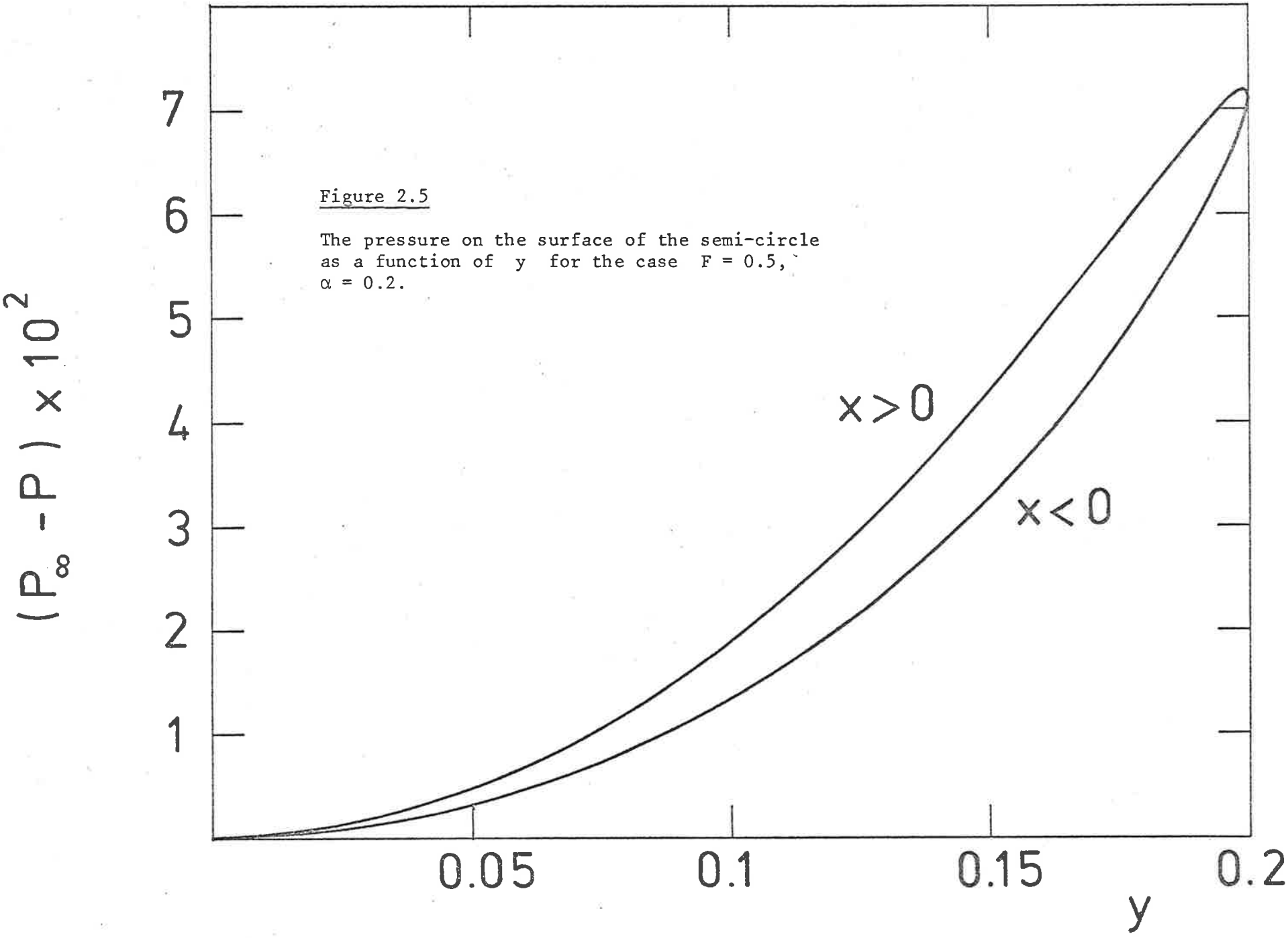

Figure 2.5

The pressure on the surface of the semi-circle as a function of y for the case $F = 0.5$, $\alpha = 0.2$.

symmetric about $x = 0$, it makes no contribution to the wave drag D , which is therefore the area enclosed by the curve in Fig. 2.5.

In Fig. 2.6(a), the wave drag is shown as a function of F , for $\alpha = 0.1$. When the Froude number is small, the linearized and non-linear results are in good agreement, but the difference between them becomes steadily greater as the Froude number is brought closer to the critical value $F = 1$. Note that the linearized drag has the limiting behaviour

$$D \to \frac{3}{2} \pi^2 \alpha^4 \quad \text{as} \quad F \to 1 \ ,$$

even though the linearized wavelength and wave height become infinite at this value of the Froude number.

Fig. 2.6(b) shows the lift force acting on the semi-circle as a function of F , for $\alpha = 0.1$. The quantity L_∞ has again been subtracted to show more clearly the differences between the linearized and non-linear results. For low values of the Froude number, the linearized solution provides a good estimate of the lift, although the effects of non-linearity appear to become more significant for Froude numbers greater than about 0.5.

2.5(b) *Supercritical case* ($F > 1$)

In the linearized theory, the critical value $F = 1$ is associated with the emergence of a fundamentally different type of solution, symmetric about $x = 0$ and possessing no waves. The non-linear results confirm the existence of such a solution. Despite its appearance, this solution bears

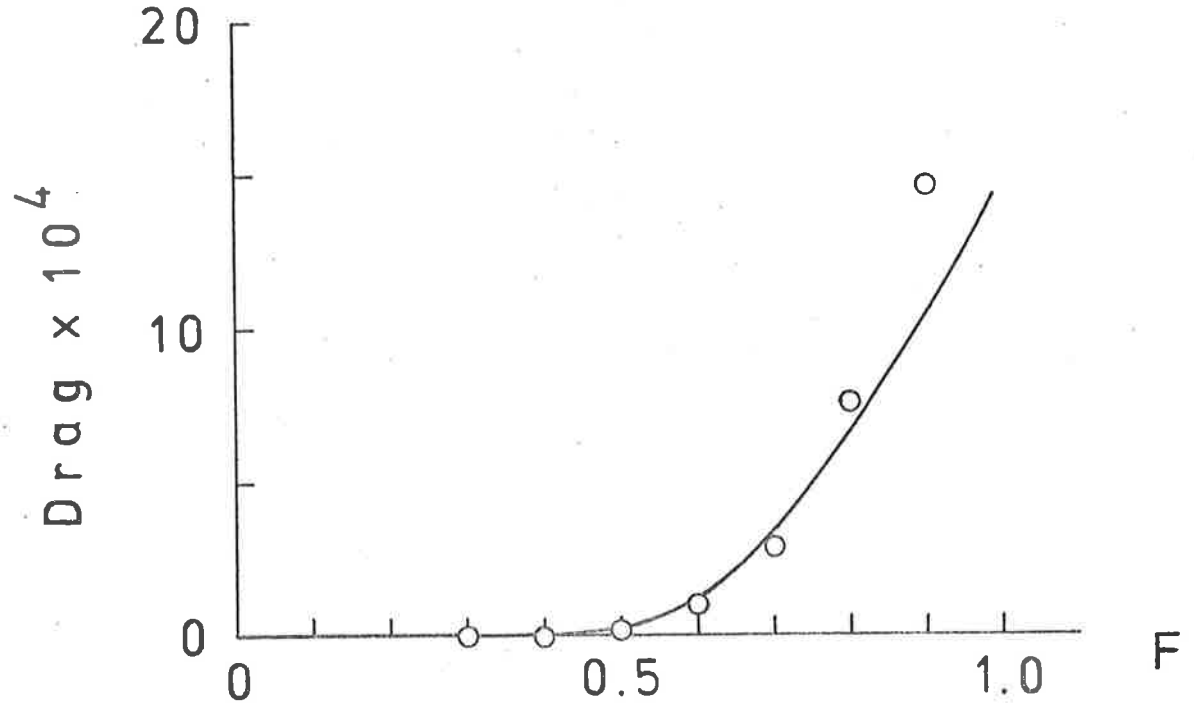

Figure 2.6(a) The dependence of the wave drag upon F for the linearized and non-linear solutions, when $\alpha = 0.1$.

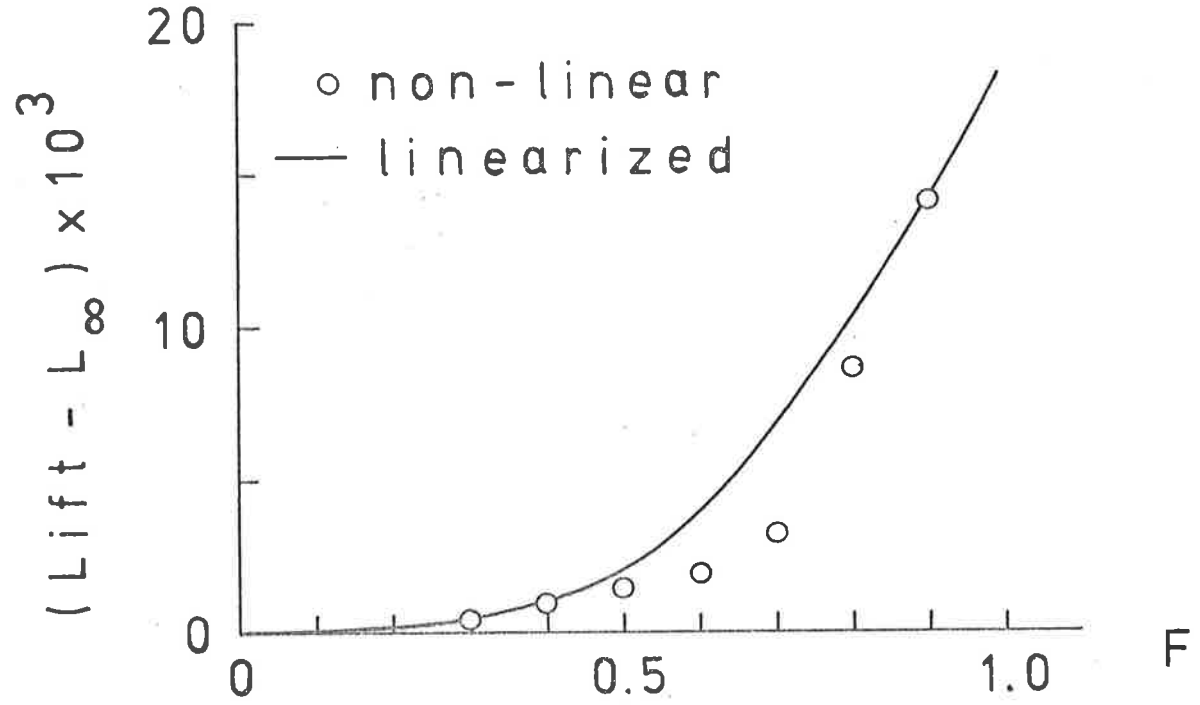

Figure 2.6(b) The dependence of the lift upon F for the linearized and non-linear solutions, when $\alpha = 0.1$.

no relation to the solitary wave, since it reduces to uniform flow as $\alpha \to 0$.

In Fig. 2.7, non-linear free-surface profiles are presented at $F = 2.1$, and for the three different circle radii $\alpha = 0.7$, $\alpha = 1.1$ and $\alpha = 1.32$. The last of these values is the largest circle radius for which Newton's method converged at this value of the Froude number. Thus it appears that, unlike the linearized solution, non-linear results may only be obtained within a certain range of values of α , for each value of the Froude number.

The physical mechanism which prevents non-linear solutions of this type from being found when α is larger than some critical value is apparently the formation of a sharp crest at the surface, with an included angle of 120°, exactly as in the case of Stokes waves. Indeed, Stokes' (1880) original analysis is local to the crest, and takes no account of whether or not the rest of the fluid contains waves. The crest is a stagnation point, at which the fluid velocity is zero, so that by Bernoulli's equation (2.3), the height of the surface there attains the maximum value $y_{max} = \frac{1}{2}F^2 + 1$. A portion of the conjectured limiting profile, with its included angle of 120°, is sketched in Fig. 2.7. Of course, the present numerical technique is not capable of resolving such a region of very high curvature in the vicinity of the crest, but it is possible that this difficulty may be overcome by spacing points unevenly at the free surface, with a high concentration of points near the crest. This possibility is presently being explored.

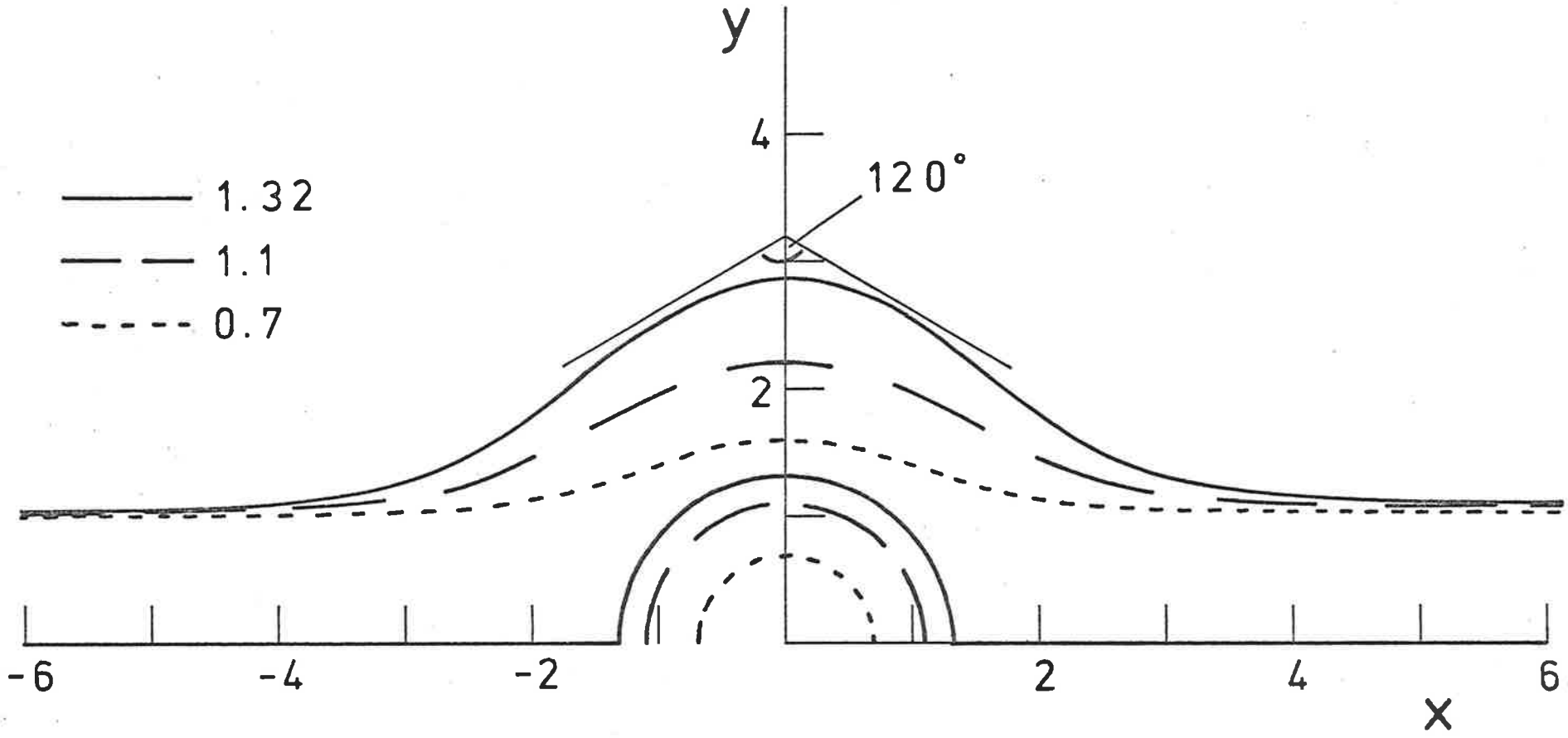

Figure 2.7 Non-linear solutions for $F = 2.1$, and $\alpha = 0.7, 1.1, 1.32$. A portion of the conjectured limiting profile with a 120° angle at the crest is also shown. The fluid is flowing from left to right.

2.6 Some Remarks on the Properties of the Downstream Wave Train.

In this section, we examine the effects of non-linearity upon the wavelength of the downstream waves, and upon the mean level of the free surface downstream.

The unsteady problem in which a body beneath the free surface is impulsively started from rest in a stationary fluid has been considered by Benjamin (1970). By applying the mass and momentum conservation equations, Benjamin demonstrated that non-linear effects result in a forward surge ahead of the body, and a corresponding drop in the mean free-surface level behind the body, in the region in which the waves are present. The flow in a certain region near the body may be regarded as steady, although outside this region, the upstream surge continues to propagate further upstream, and waves are continually being added to the downstream wave train. After the passage of an infinite amount of time, the free surface ahead of the bump is expected to be uniformly elevated, whilst on the downstream side, the wave train extends infinitely far, and the mean level of the fluid in this wave train is expected to be lower than in the undisturbed fluid.

The effects of non-linearity on the downstream wave-length have been discussed by Salvesen and von Kerczek (1978). These authors consider the case in which the disturbance beneath the free surface is a point vortex, and solve the resulting non-linear problem both by a perturbation technique, and by a direct numerical approach. Their results appear to indicate that, as the downstream wave height is increased

(by increasing the vortex strength), the downstream wavelength decreases for $F < 0.75$, but *increases* for $F > 0.75$. However, the accuracy of their results is uncertain beyond $F = 0.75$, and they remark that, for large values of F, the wavelength may perhaps increase initially and then decrease as the downstream wave height is made to increase.

The steady problem formulated and solved in this chapter differs in one respect from the problem considered by Benjamin. In the present problem, the upstream depth and velocity are assumed to be known, and are taken as reference quantities for the other variables in the problem. However, in Benjamin's problem, the upstream conditions after infinite time has elapsed are no longer known. Thus the upstream depth in the present problem is presumably the sum of Benjamin's undisturbed depth plus the height of the forward surge which has advanced upstream. Accordingly, the free-stream Froude number in the present problem possibly differs slightly from Benjamin's.

To compute the mean free-surface height and the wavelength of the downstream waves from our numerically obtained free-surface profile $(x(\phi,1), y(\phi,1))$, a cubic spline function $y_S(x)$ is fitted through the points (x_0,y_0), (x_1,y_1),..., (x_N,y_N). The positions $x_t^{(1)}$ and $x_t^{(2)}$ of two successive wave troughs are found by solving

$$\frac{dy_S}{dx}(x_t^{(i)}) = 0 , \quad i = 1,2 ,$$

by Newton's method and exact differentiation of the cubic spline function $y_S(x)$. The wavelength is thus

$$\lambda = x_t^{(2)} - x_t^{(1)} \quad , \tag{2.32}$$

and the mean level of the free surface is

$$y_{mean} = \frac{1}{\lambda} \int_{x_t^{(1)}}^{x_t^{(2)}} y \, dx \quad . \tag{2.33}$$

The integral in equation (2.33) is evaluated using the Trapezoidal Rule.

Two non-linear free-surface profiles are shown in Fig. 2.8, for $F = 0.9$ and the two values of the circle radius $\alpha = 0.1$ and $\alpha = 0.15$. These solutions exhibit a strong non-linear rise in the free-surface level ahead of the obstacle. However, unlike the problem considered by Benjamin, the free surface here must ultimately return to the equilibrium position $y = 1$ as $x \to -\infty$, in accordance with the upstream condition (2.11). Nevertheless, the imposition of either the linearized solution or uniform flow conditions at the first point ϕ_0 ceases to be an acceptable approximation for this high value of the Froude number and so, in order to control the size of the upstream waves, the value of η_0 imposed at this point must be increased significantly above the value suggested by linearized theory. In view of the relatively small number of free-surface points in the numerical scheme to which we are restricted by the storage limits of the computer, it has not been possible to cluster a sufficient number of points about the very sharp wave crests obtained for the case $\alpha = 0.15$, and consequently, the solution for this value of α is slightly affected by numerical error. This value of the Froude number ($F = 0.9$) is possibly the largest value of F

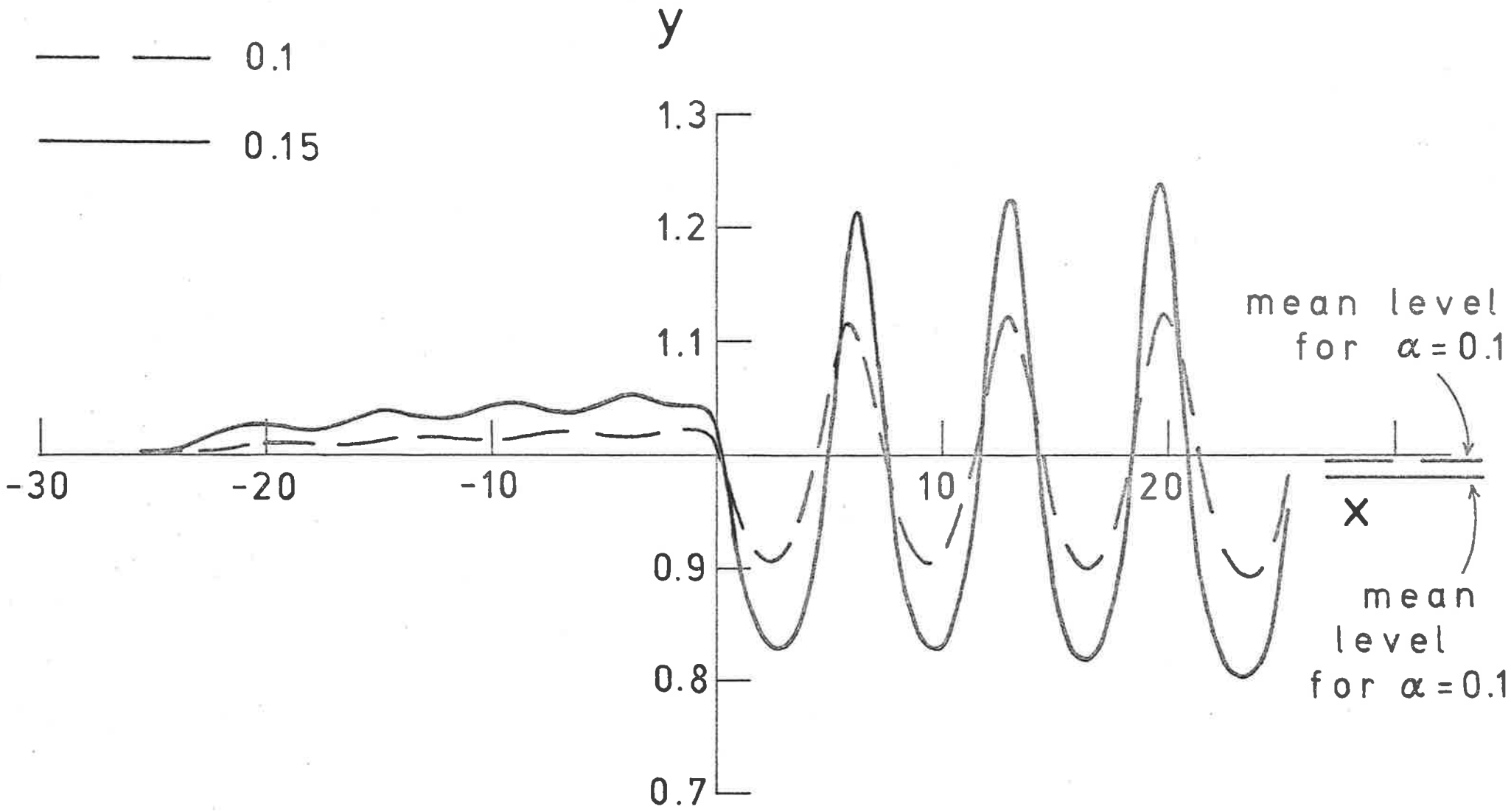

Figure 2.8 Non-linear solutions for F = 0.9, and α = 0.1, 0.15. The mean levels of the downstream wave trains are also indicated.

F	α	λ	y_{mean}	y_{mean} (Benjamin)
0.9	0.02	7.28	1.000	0.99999
0.9	0.04	7.24	1.001	0.99964
0.9	0.06	7.19	1.001	0.99816
0.9	0.08	7.14	0.999	0.99415
0.9	0.1	7.10	0.995	0.98570
0.9	0.12	6.89	0.990	0.97036
0.9	0.14	6.77	0.985	0.94507
0.9	0.15	6.71	0.980	0.92761

TABLE 2.1: The effect of non-linearity on wavelength and mean depth. Results obtained from the formula of Benjamin are also shown.

for which accurate non-linear solutions may be obtained with the present number of free-surface points, and to proceed to higher values of F would undoubtedly require many more points at the free surface.

In Table 2.1, the downstream wavelength and mean free-surface level are presented as functions of the circle radius α, for $F = 0.9$. Also tabulated is the mean free-surface level approximated from the formula of Benjamin (1970). For the mean level of the fluid in the wave train, Benjamin gives the expression

$$y_{mean} = 1 - \frac{6\gamma+F(1-\gamma)(2\gamma-1)}{8(1+F)(1-\gamma F)} A_1^2 , \qquad (2.34)$$

where

$$\gamma = \tfrac{1}{2}\left(1 + \frac{2\kappa_0}{\sinh(2\kappa_0)}\right) ,$$

and the quantity κ_0 is related to the Froude number F by the dispersion relation (2.18). The symbol A_1 in equation (2.34) denotes the linearized downstream wave amplitude, and is defined in equation (2.22).

The results presented by Salvesen and von Kerczek (1978) for a Froude number of 0.871 suggest that the wavelength *increases* with increasing disturbance strength. This trend is not observed in the results displayed in Table 2.1, for the very similar value of Froude number F = 0.9. Instead, the wavelength computed from our converged non-linear surface profiles by means of equation (2.32) is observed to *decrease* monotonically as the disturbance strength α is increased. A shortening of the wavelength with increasing α is also evident in Fig. 2.8.

From Table 2.1, it is evident that Benjamin's formula (2.34) for the mean free-surface level downstream gives results which are consistently lower than the value of y_{mean} obtained from the numerical results. Of course, equation (2.34) is only valid to second order in the wave amplitude, and so possibly ceases to be applicable to the cases in which α is large. More importantly, however, the quantity y_{mean} is influenced by two opposing non-linear effects, one of which has been ignored by Benjamin. The first such effect is described by Benjamin, and results in the tendency for the mean free-surface level to be lower than the undisturbed level, detailed in equation (2.34). There is, however, a second consequence of non-linearity, ignored by Benjamin, which tends to *raise* the mean free-surface level. This effect, which is also of second order in the wave amplitude, is a property of

all Stokes waves, and is described by Schwartz (1974b) and Cokelet (1977). For low values of the Froude number, this second effect dominates, resulting in a nett rise in the mean surface level downstream. Such a situation exists for the solution presented in Fig 2.3, for example.

2.7 The possibility of multiple solutions

In Fig. 2.9, we display the range of values of the independent parameters F and α for which it has been possible to compute non-linear solutions possessing a train of downstream waves. The highest values of α for which the Newton process converged are marked on the diagram, for a range of different Froude numbers. It has not been possible to obtain solutions for very small Froude numbers ($F < 0.3$), since the extremely short wavelength of the downstream waves in this instance renders it impossible to maintain a sufficient number of free-surface points per wavelength while still including an appropriate section of the free surface upstream and downstream of the semi-circle. Similarly, results for $F > 0.9$ are of doubtful accuracy, since we are unable to provide a sufficient number of points at the free surface to describe adequately the very sharp wave crests formed in this case.

The dashed line in Fig. 2.9 indicates the approximate position of the boundary of the region within which we conjecture the existence of non-linear solutions possessing a train of downstream waves. The position of this line was determined by assuming that the Froude number of the down-

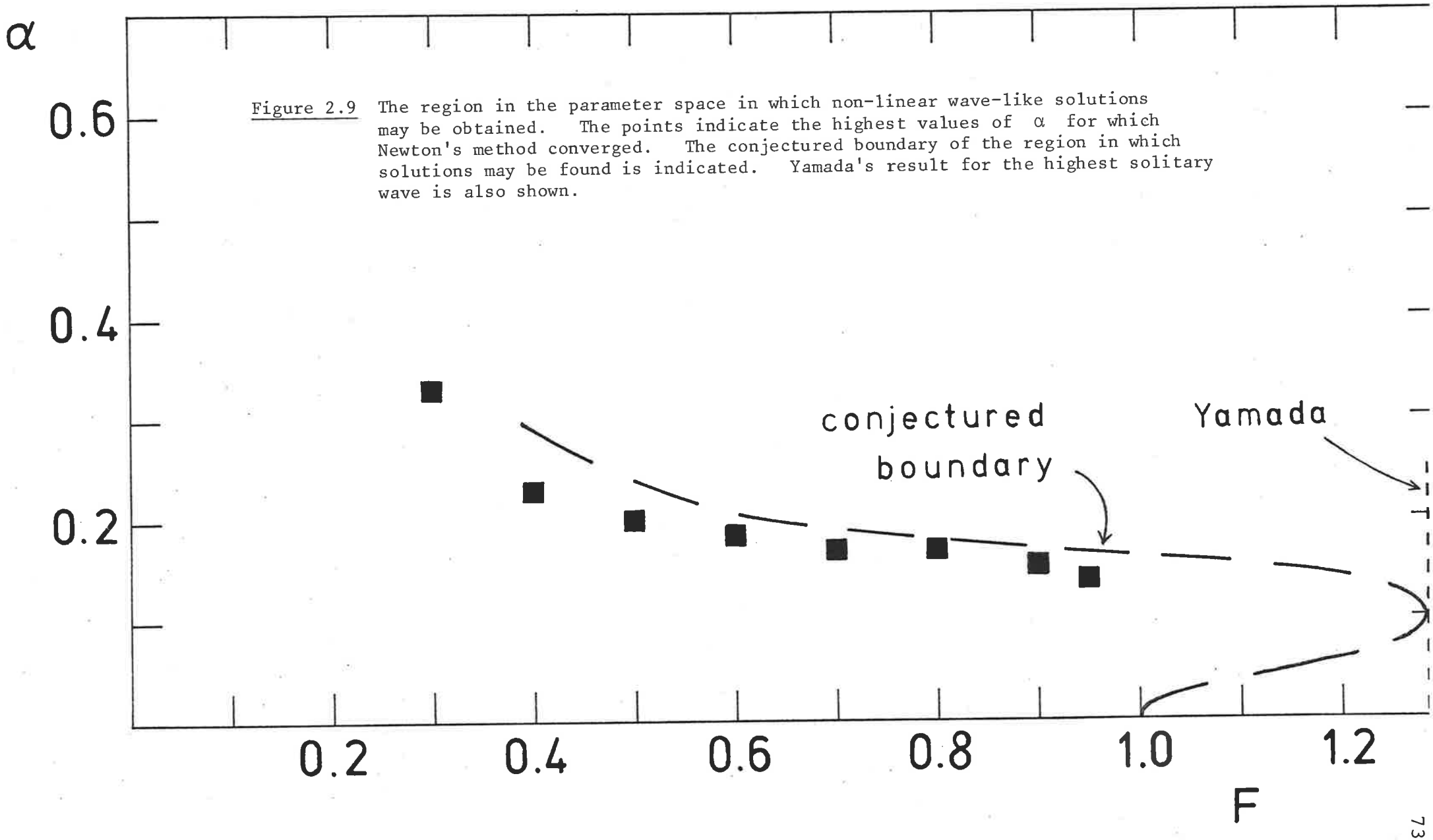

Figure 2.9 The region in the parameter space in which non-linear wave-like solutions may be obtained. The points indicate the highest values of α for which Newton's method converged. The conjectured boundary of the region in which solutions may be found is indicated. Yamada's result for the highest solitary wave is also shown.

stream Stokes wave train is the same as the free-stream Froude number F ; this is an excellent approximation for small F and we expect it to provide reasonable results over the range of Froude numbers $0.3 < F < 0.95$ for which numerical results have been presented in Fig. 2.9. However, for larger values of the Froude number F , the approximation may perhaps cease to be as good, by virtue of the tendency of the mean free-surface level downstream to drop when the downstream wave amplitude is large, as described in Section 2.6. The portion of the dashed line in Fig. 2.9 lying in the region $F < 1$ was obtained from our numerical results by extrapolating plots of wave height *versus* α^2 up to the maximum wave height for Stokes waves, with approximate Froude number F , computed by Schwartz (1974b) and Cokelet (1977). Note that the region in which solutions are conjectured to exist extends well into the supercritical regime $F > 1$, and in Fig. 2.9 it is shown as terminating at $F = 1.286$, which is Yamada's (1957) result for the highest solitary wave. However, since the downstream Froude number is not the same as the free-stream Froude number F , it is likely that this region actually terminates at a slightly smaller value of F than this.

The region of the parameter space (F,α) in which non-linear solutions may be found is similarly restricted for the supercritical wave-free branch of solutions described in Section 2.5(b). In Fig. 2.10, the highest values of α for which the Newton process converged are shown for a range of different Froude numbers. The dashed line on this diagram indicates the approximate position of the boundary of the region

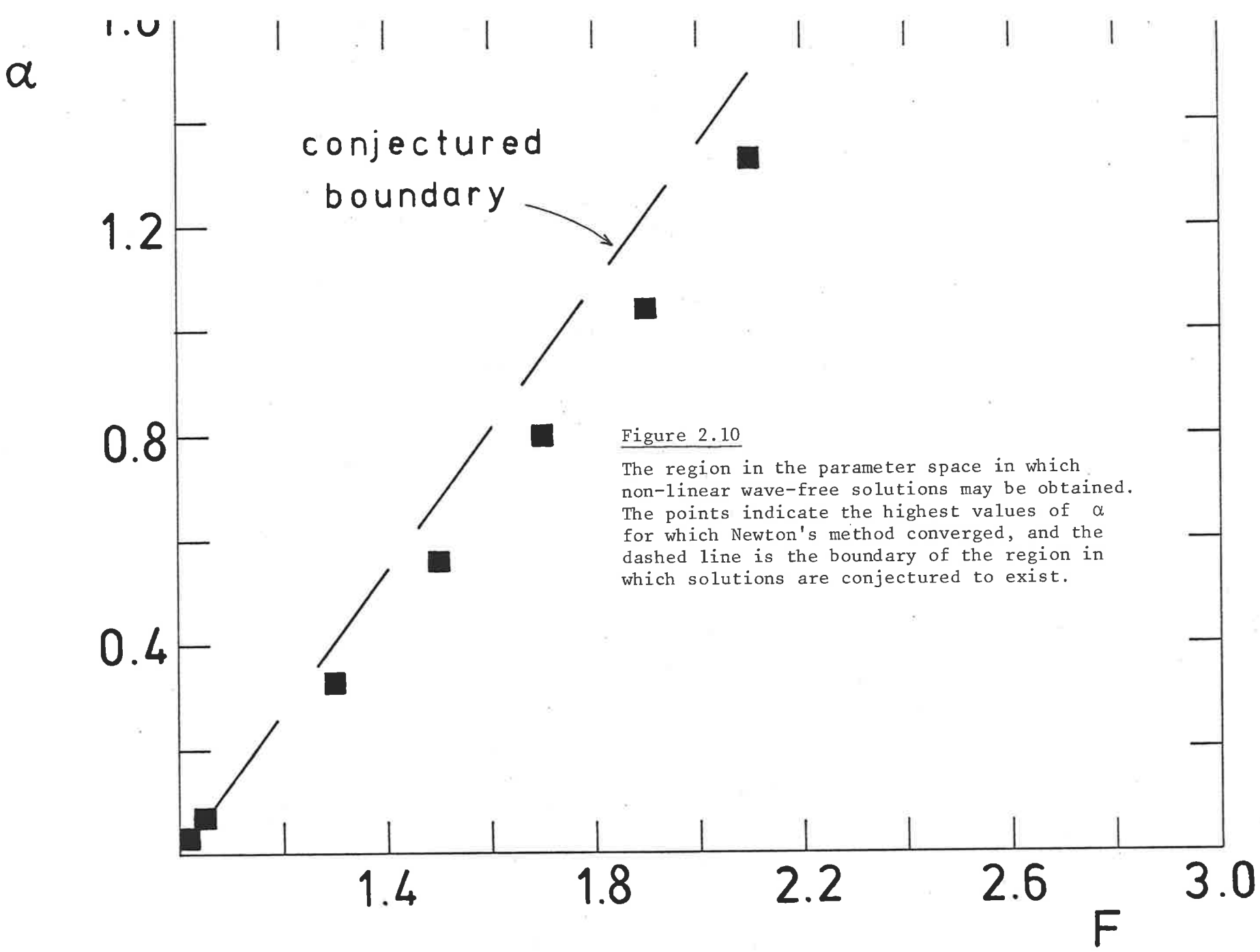

Figure 2.10

The region in the parameter space in which non-linear wave-free solutions may be obtained. The points indicate the highest values of α for which Newton's method converged, and the dashed line is the boundary of the region in which solutions are conjectured to exist.

within which non-linear solutions are conjectured to exist. Solutions for which the parameters F and α describe a point on this line are expected to possess a sharp crest at the free surface, where the fluid is at rest at the maximum height $y_{max} = \frac{1}{2}F^2 + 1$. This dashed line has been obtained from our numerical results by extrapolating plots of maximum free-surface elevation *versus* α^2 up to the height y_{max} at which the crest occurs. As with the linearized solution, non-linear solutions of this type appear only to exist for $F > 1$.

A comparison of Fig. 2.9 and Fig. 2.10 indicates that, in a portion of the supercritical flow regime $F > 1$, there exists a region of overlap between the regions within which the two different branches of solution are conjectured to exist. It would therefore appear that, in this portion of the supercritical flow regime, there is a lack of uniqueness in the solutions to this problem, since both the symmetric wave-free solution and a solution containing a train of Stokes waves downstream are both possible outcomes.

Of course, there is no guarantee that these two branches of solution are the *only* possible outcomes in this situation. Other types of solution are perhaps possible; for example, it may be possible to compute solutions of the type obtained by Aitchison (1979), in which the flow is subcritical on one side of the semi-circular bump and supercritical on the other side, although we have not so far obtained such results. The computation of such a family of solutions would most probably involve a different numerical formulation to that described in this chapter.

2.8 Summary and Discussion

In this chapter, two-dimensional fluid flow over a submerged semi-circle has been investigated. The solution is facilitated by the choice of the complex potential $f = \phi + i\psi$, rather than physical plane coordinates, as the independent variable.

A linearized solution has been developed by retaining the first term of a regular series expansion in the square of the circle radius, α^2 . For subcritical flow $F < 1$, a wave-free region is predicted upstream, followed by a regular wave train downstream. For supercritical flow $F > 1$, a symmetric wave-free solution is predicted. There is no solution for $F = 1$.

The exact non-linear equations are solved numerically at the free surface, by a process of Newtonian iteration. In the subcritical case $F < 1$, an essentially wave-free region is obtained upstream, followed by a train of non-linear Stokes waves downstream. The accuracy of these results is confirmed by observing that the free-surface profile obtained is largely insensitive to further reductions in the size of the spacing between points at the free surface. In addition, the downstream wave train is unaffected by the choice of downstream truncation point, except within a distance of about half a wavelength upstream of this point. However, due to the relatively small number of free-surface points to which we are restricted, we are unable to compute the very steep waves obtained when α is large or F is close to one. The major disadvantage of the present method, in which ϕ is

chosen to be the independent variable at the free surface, is that points in the numerical scheme tend to cluster unnecessarily about the wave troughs, but are distributed very sparsely at the wave crests, where they are most needed. When α is large, the linearized theory severely under-predicts the value of the drag force on the semi-circle, indicating the importance of non-linear effects in these cases.

In the supercritical case $F > 1$, the symmetric wave-free profile predicted by the linearized solution is confirmed by the non-linear results. However, the physical existence of a stable solution of this type seems somewhat implausible. It appears that the non-linear free-surface profile is ultimately limited by the formation of a sharp crest with sides that enclose an angle of 120°.

Although the linearized solution fails to exist for $F = 1$, there is no reason to suppose à *priori* that the non-linear solution should likewise fail at this value of the Froude number, for finite downstream wave amplitude (although the linearized solution must become asymptotically correct as $\alpha \to 0$). Indeed we expect that non-linear solutions possessing a train of downstream Stokes waves may be found both for $F = 1$ and also in a portion of the supercritical flow regime $F > 1$. Since the symmetric wave-free solution also exists for $F > 1$, there is thus the possibility that a lack of uniqueness may exist in the non-linear solutions to this problem, for certain values of the independent variables F and α. In addition, other branches of solution might perhaps be possible, such as those described by Aitchison (1979).

CHAPTER THREE

TWO-DIMENSIONAL GRAVITY FLOW ABOUT A SUBMERGED SEMI-ELLIPSE

3.1 Introduction

The problem to be examined in this chapter concerns the steady two-dimensional flow of an ideal fluid in a horizontal stream, attached to the bottom of which is a semi-elliptical body. This problem represents an obvious extension of the work presented in the previous chapter, and accordingly, results from chapter two will be utilized throughout.

When the free-stream Froude number F is less than unity, the surface downstream of the semi-ellipse is generally expected to consist of a train of waves extending infinitely far downstream. The energy radiated away to infinity by this wave train is exactly balanced by a horizontal force component (the wave resistance) acting upon the semi-ellipse. When $F > 1$, a branch of solutions exists for which no downstream waves are present. In this regard, solutions to the present problem are similar to those obtained in chapter two, for flow about a submerged semi-circle. However, non-linear solutions to the present problem for $F < 1$ appear to exhibit the additional property that, for ellipses of certain special lengths, the downstream wave train may be made to vanish, resulting in zero wave resist-

ance experienced by the body. This result may be of significance in the design of certain underwater craft, for example. In the present chapter, attention will be focussed on the subcritical regime $F < 1$, with particular emphasis on those solutions for which the downstream wave train apparently vanishes.

A linearized solution to the present problem was developed by Lamb (1932, p.409) and will be discussed in Section 3.3(b). One of the features of this linearized solution is that, for a given value of the upstream Froude number, the free surface is predicted to be free of downstream waves for ellipses of certain special lengths, resulting in zero drag force acting on the ellipse in these cases. In fact, the plot of wave resistance *versus* ellipse length for fixed upstream Froude number and ellipse height is undulatory and passes through zero infinitely often, giving rise to a countably infinite set of ellipse lengths for which the wave resistance is zero, at each value of the upstream Froude number.

The question of whether a wave-making disturbance may ever give rise to a *non-linear* wave resistance of precisely zero has been investigated recently by Schwartz (1981). He considered the problem of waves induced in a fluid of infinite depth by a moving pressure distribution applied to the free surface, and demonstrated that, for certain values of the pressure length, the non-linear wave resistance obtained was indeed extremely small, with a value of the order of 10^{-5} times the maximum resistance obtained with the same value of non-dimensional overpressure. The

corresponding problem for a fluid of fixed finite depth was considered by von Kerczek and Salvesen (1977). Their results also appear to indicate very small values of wave resistance for certain pressure lengths.

In the present study, the problem is formulated as in chapter two, using conformal mapping to transform the bottom into a straight line, free of singular points. The velocity potential and streamfunction are treated as the independent variables, and a boundary-integral technique is used to obtain non-linear free-surface profiles.

3.2 Formulation of the Problem

We consider two-dimensional, steady flow of an ideal fluid in a channel in which the flow infinitely far upstream is uniform, with depth H and velocity c. The fluid flows from left to right. A semi-elliptical object of length $2R_X$ and height R_Y is attached to the channel bed, which is otherwise flat and horizontal, and is placed symmetrically about the y-axis, which points vertically. The fluid is subject to the downward acceleration of gravity, g.

The problem is expressed in terms of dimensionless variables forthwith, by referencing all lengths and velocities to the quantities H and c respectively, as in Section 2.2. The velocity potential ϕ and streamfunction ψ are non-dimensionalized with respect to the quantity cH ; in terms of dimensionless variables, the bottom is chosen to be the streamline $\psi = 0$, and the free surface is thus $\psi = 1$. Solutions to this problem are thus dependent upon the three dimensionless parameters

$$F = \frac{c}{(gH)^{\frac{1}{2}}}, \quad \alpha = \frac{R_X}{H} \quad \text{and} \quad \beta = \frac{R_Y}{H} .$$

The quantity F is the upstream depth-based Froude number, and α and β are respectively the dimensionless ellipse half-length and the ellipse height. The non-dimensional flow situation is depicted in Fig. 3.1.

Since the fluid is incompressible and flows without rotation, it follows that the velocity potential and stream-function obey the Cauchy-Riemann equations (2.1) in the fluid interior. Thus the complex function $f = \phi + i\psi$ is to be sought as an analytic function of the variable $z = x + iy$. The motion of the fluid at the free surface is governed by the Bernoulli equation

$$\tfrac{1}{2}F^2 w\bar{w} + y = \tfrac{1}{2}F^2 + 1 \qquad (3.1)$$

where

$$w = \frac{df}{dz} = u - iv ,$$

and u,v are the horizontal and vertical components of velocity. The bar denotes complex conjugation. The condition of no flow normal to the bottom is expressed as

$$u \frac{dh}{dx} = v \quad \text{on} \quad y = h(x) , \qquad (3.2)$$

where the bottom $y = h(x)$ is described by the equation

$$h(x) = \begin{cases} \frac{\beta}{\alpha}(\alpha^2 - x^2)^{\frac{1}{2}} , & |x| \leqslant \alpha \\ 0 , & |x| > \alpha \end{cases} .$$

The bottom is now transformed into a straight line, using conformal mapping, as in chapter two. A new variable

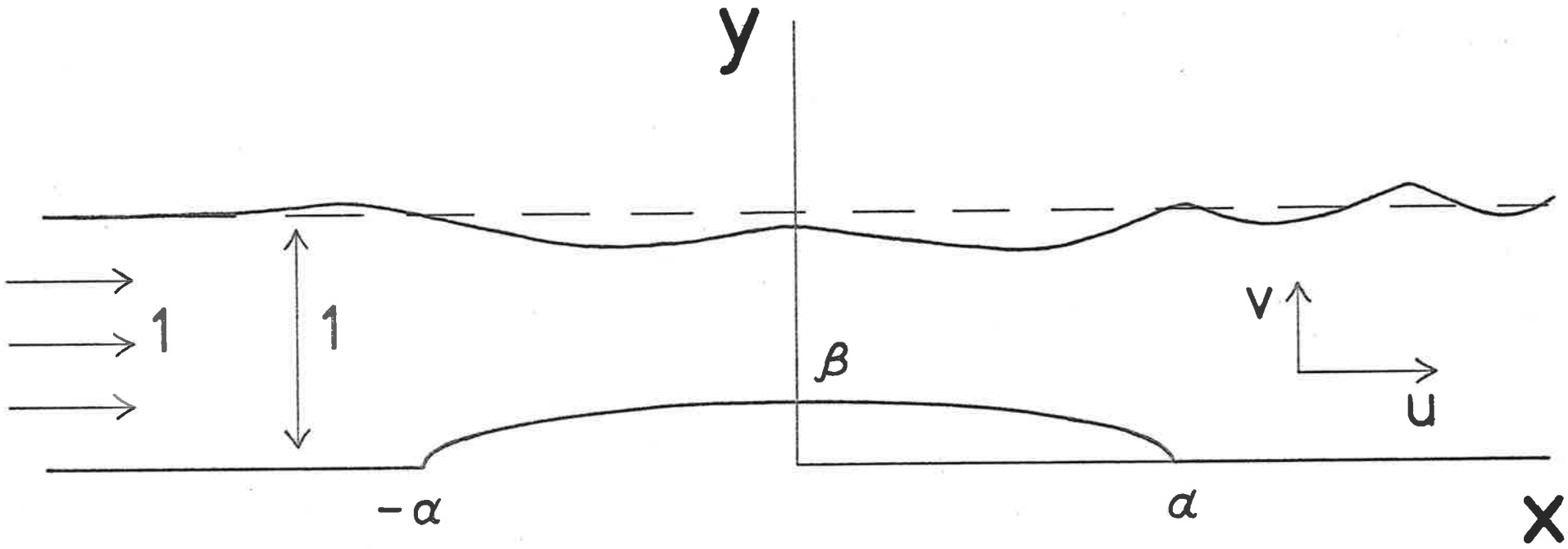

Figure 3.1 The non-dimensional flow situation in the z-plane.

$\tau = \xi + i\eta$ is defined by the relation

$$z = \tau + \frac{\beta}{\alpha}(\tau^2-\alpha^2)^{\frac{1}{2}} \ , \qquad (3.3)$$

which is a straightforward generalization of the Joukowski transformation (2.6). Thus the complex potential f is now to be sought as an analytic function of τ, subject to the appropriately transformed Bernoulli equation (3.1) and bottom condition (3.2).

Since the bottom is now free of stagnation points in the τ-plane, the roles of τ and f may again be interchanged, as in chapter two. The analytic function $\tau(f)$ is thus required to satisfy the f-plane bottom condition

$$\eta = 0 \quad \text{on} \quad \psi = 0 \ , \qquad (3.4)$$

and the Bernoulli equation

$$\tfrac{1}{2}F^2 \frac{\alpha^2(A^2+B^2)}{(\alpha A+\beta\xi)^2+(\alpha B+\beta\eta)^2} \quad \frac{1}{\tau_\phi \bar{\tau}_\phi} + \eta + \frac{\beta}{\alpha}B = \tfrac{1}{2}F^2 + 1$$

$$\text{on} \quad \psi = 1 \ , \qquad (3.5)$$

where we have defined

$$(\tau^2-\alpha^2)^{\frac{1}{2}} = A + iB \ ,$$

and the subscripts denote partial differentiation. Far upstream, the flow is uniform, which results in the radiation condition

$$\tau \to f\left(1 + \frac{\beta}{\alpha}\right)^{-1} \quad \text{as} \quad \phi \to -\infty \ . \qquad (3.6)$$

The integral equation relating the real and imaginary parts of $\tau'(f)$ along the free surface $\psi = 1$ is derived

exactly as in chapter two. The f-plane strip $0 \leqslant \psi \leqslant 1$ is first extended by reflection about the bottom $\eta = 0$ to form an augmented section $-1 \leqslant \psi \leqslant 1$. The bottom condition (3.4) is satisfied automatically, by requiring values of τ' on the image strip $-1 \leqslant \psi \leqslant 0$ to be related to values on the true strip $0 \leqslant \psi \leqslant 1$ by means of equation (2.7). Cauchy's Integral Theorem is now applied to the analytic function

$$\chi(f) = \frac{d\tau}{df} - \left(1 + \frac{\beta}{\alpha}\right)^{-1}$$

along the same path of integration in the f-plane as before. Taking the real part of the resulting equation gives

$$\left[\xi_\phi(\phi,1) - \left(1 + \frac{\beta}{\alpha}\right)^{-1}\right] - \frac{2}{\pi}\int_{-\infty}^{\infty}\left[\xi_\theta(\theta,1) - \left(1 + \frac{\beta}{\alpha}\right)^{-1}\right]\frac{d\theta}{(\theta-\phi)^2+4}$$

$$= -\frac{1}{\pi}\left\{\int_{-\infty}^{\infty}\frac{\eta_\theta(\theta,1)\,d\theta}{\theta-\phi} + \int_{-\infty}^{\infty}\frac{\eta_\theta(\theta,1)(\theta-\phi)\,d\theta}{(\theta-\phi)^2+4}\right\}. \qquad (3.7)$$

This equation is an obvious generalization of equation (2.10).

The free-surface profile is thus found parametrically in the form $(\xi(\phi,1), \eta(\phi,1))$ by solving the system of equations (3.5), (3.6) and (3.7). The variables x and y may be recovered from equation (3.3).

The wave drag D and the lift L are computed by integrating the product of the pressure p with the appropriate component of the normal vector over the surface of the ellipse. Here, p has been made dimensionless by reference to the quantity $\rho g H$, whilst D and L are referred to the quantity $\rho g H^2$. The density of the fluid is ρ. Thus

$$D = \int_{-\alpha}^{\alpha} ph'(x)\,dx$$

$$= \tfrac{1}{2}F^2 \frac{\beta}{\alpha} \int_{-\alpha}^{\alpha} (u^2+v^2) \frac{x}{(\alpha^2-x^2)^{1/2}}\,dx \qquad (3.8a)$$

and

$$L = \int_{-\alpha}^{\alpha} p\,dx$$

$$= \tfrac{1}{2}F^2 \int_{-\alpha}^{\alpha} (u^2+v^2)\,dx - \alpha F^2 + \frac{\pi}{2}\alpha\beta - 2\alpha \,. \qquad (3.8b)$$

Transforming these equations into the τ-plane yields

$$D = \tfrac{1}{2}F^2\frac{\beta}{\alpha} \int_{-\alpha}^{\alpha} \frac{\xi(\alpha^2-\xi^2)^{1/2}}{\left[\left(\frac{\beta}{\alpha}\right)^2-1\right]\xi^2+\alpha^2} \left(\frac{\partial\phi}{\partial\xi}\right)^2_{\eta=0} d\xi \qquad (3.9a)$$

and

$$L = \tfrac{1}{2}F^2 \int_{-\alpha}^{\alpha} \frac{\alpha^2-\xi^2}{\left[\left(\frac{\beta}{\alpha}\right)^2-1\right]\xi^2+\alpha^2} \left(\frac{\partial\phi}{\partial\xi}\right)^2_{\eta=0} d\xi - \alpha F^2 + \frac{\pi}{2}\alpha\beta - 2\alpha \,. \qquad (3.9b)$$

Finally, these equations are transformed into the f-plane, where they become

$$D = \tfrac{1}{2}F^2\frac{\beta}{\alpha} \int_{\phi_{-\alpha}}^{\phi_{+\alpha}} \frac{\xi(\alpha^2-\xi^2)^{1/2}}{\left[\left(\frac{\beta}{\alpha}\right)^2-1\right]\xi^2+\alpha^2} \frac{1}{\xi_\phi}\,d\phi \qquad (3.10a)$$

and

$$L = \tfrac{1}{2}F^2 \int_{\phi_{-\alpha}}^{\phi_{+\alpha}} \frac{\alpha^2-\xi^2}{\left[\left(\frac{\beta}{\alpha}\right)^2-1\right]\xi^2+\alpha^2} \frac{1}{\xi_\phi}\,d\phi - \alpha F^2 + \frac{\pi}{2}\alpha\beta - 2\alpha \,. \qquad (3.10b)$$

The functions ξ and ξ_ϕ in equations (3.10) are to be evaluated along the bottom $\psi = 0$, and the quantities $\phi_{\pm\alpha}$ are the solutions to the equations

$$\xi(\phi_{\pm\alpha}, 0) = \pm\alpha \,. \qquad (3.11)$$

3.3 Two linearized theories

3.3(a) *An essentially circular ellipse*

If the ellipse is small and has an aspect ratio $R = \beta/\alpha$ of order 1, a linearized theory may be developed after the fashion of Section 2.3, by expanding the solution $\tau(f)$ in a regular perturbation expansion with small parameter α^2, and retaining only terms of first order in this quantity.

The solution $\tau(f)$ is taken to be of the form

$$\tau(f) = f(1+R)^{-1} + \alpha^2 F_1(f) + O(\alpha^4). \qquad (3.12)$$

Inserting equation (3.12) into the Bernoulli equation (3.5) and retaining only terms of first order in α^2 results in the linearized free-surface condition

$$\mathrm{Re}\left\{\frac{dF_1}{df} + \frac{i}{F^2} F_1\right\} = \frac{R}{2F^2(\phi^2+1)} + \frac{R}{2}\frac{1-\phi^2}{(\phi^2+1)^2}$$

$$\text{on} \quad \psi = 1 . \qquad (3.13)$$

The function $F_1(f)$ is to be sought as a Fourier integral, of the form

$$F_1(f) = \int_0^\infty C(\kappa)\sin(\kappa f)\,d\kappa , \qquad (3.14)$$

and the real function $C(\kappa)$ is determined by substituting equation (3.14) into equation (3.13). Thus

$$C(\kappa) = \frac{R}{2}\,\frac{e^{-\kappa}\left(\kappa + \frac{1}{F^2}\right)}{\kappa\cosh(\kappa) - \frac{1}{F^2}\sinh(\kappa)} .$$

It is evident that the function $C(\kappa)$ in equation (3.14) differs only by a factor of R from the expression

obtained in Section 2.3. Thus the interpretation of the integral in equation (3.14) has already been discussed in that section. For $F > 1$, a symmetric, wave-free solution is obtained. There is no solution for $F = 1$. For $F < 1$, a wave-free region is predicted upstream of the ellipse, followed by a train of linear, downstream waves. In this case, the solution (3.12) may be written

$$\tau(f) = f(1+R)^{-1} + \tfrac{1}{2}R\alpha^2\left\{\int_0^\infty \frac{e^{-\kappa}(\kappa + \frac{1}{F^2})\sin(\kappa f)\,d\kappa}{\kappa\cosh(\kappa) - \frac{1}{F^2}\sinh(\kappa)}\right.$$

$$\left. + \frac{\pi e^{-\kappa_0}(\kappa_0 + \frac{1}{F^2})\cos(\kappa_0 f)}{(1 - \frac{1}{F^2} + \kappa_0^2 F^2)\cosh(\kappa_0)}\right\} + O(\alpha^4), \qquad (3.15)$$

where κ_0 is determined from the dispersion relation (2.18). Far downstream, equation (3.15) yields the free-surface profile

$$y \to 1 - A_1 \sin(\kappa_0 x) + O(\alpha^4) \quad \text{as} \quad x \to +\infty,$$

where the wave amplitude A_1 is given by

$$A_1 = \alpha^2 R(1+R)\,\frac{\pi e^{-\kappa_0}(\kappa_0 + \frac{1}{F^2})\sinh(\kappa_0)}{(1 - \frac{1}{F^2} + \kappa_0^2 F^2)\cosh(\kappa_0)}\,. \qquad (3.16)$$

An expression for the linearized wave drag D is derived as in Section 2.3, by inverting equation (3.15) to obtain a relation of the form $f = f(\tau)$, and then substituting into equation (3.9a), with $\eta = 0$ ($\psi = 0$). This results in the classical formula

$$D = \tfrac{1}{4}A_1^2\left[1 - \frac{2\kappa_0}{\sinh(2\kappa_0)}\right] + O(\alpha^6), \qquad (3.17)$$

given by Lamb (1932), in which the wave amplitude A_1 is obtained from equation (3.16).

The linearized lift force L is likewise obtained from equation (3.15) by inverting and substituting into equation (3.9b), with $\eta = 0$. This yields

$$L = \tfrac{1}{2}\alpha(1+R)^2F^2I - \tfrac{1}{2}\alpha^3R(1+R)^3F^2I \int_0^\infty \frac{e^{-\kappa}(\kappa + \frac{1}{F^2})\kappa\, d\kappa}{\kappa\cosh(\kappa) - \frac{1}{F^2}\sinh(\kappa)}$$

$$- \alpha F^2 + \frac{\pi}{2}\alpha\beta - 2\alpha + 0(\alpha^5) \quad , \qquad (3.18)$$

where

$$I = \begin{cases} \dfrac{2}{1-R^2} + \dfrac{R^2}{(1-R^2)^{3/2}} \ln\left(\dfrac{1-(1-R^2)^{1/2}}{1+(1-R^2)^{1/2}}\right) & , \quad R < 1 \\ \dfrac{2}{1-R^2} + \dfrac{2R^2}{(R^2-1)^{3/2}} \arctan\,(R^2-1)^{1/2} & , \quad R > 1 \end{cases} \qquad (3.19)$$

In the limit $\alpha \to 0$, the semi-elliptical body degenerates to a vertical plate of height β and zero thickness attached to the bottom. This plate still disturbs the upstream uniform flow, and thus generates a downstream wave train. The wave resistance experienced by the plate is obtained from equation (3.17) by allowing $\alpha \to 0 (R \to \infty)$, and takes the finite value

$$D \to \tfrac{1}{4}\beta^4 F^2 \frac{\pi^2\kappa_0^2 e^{-\kappa_0}(\kappa_0 + \frac{1}{F^2})}{(1 - \frac{1}{F^2} + \kappa_0^2F^2)\cosh(\kappa_0)} \quad \text{as} \quad \alpha \to 0 \ .$$

The lift experienced by the ellipse is also finite in the limit $\alpha \to 0$, as a consequence of the effects of *leading edge suction*. In this limiting case, the ellipse has become

a vertical plate of zero thickness, upon the surface of which the fluid velocity has infinite magnitude. By Bernoulli's equation, the pressure on the surface of this plate is negative infinite, but acts on a body of zero width, resulting in a finite upward lift force acting on the plate. The magnitude of this lift force is obtained from the present linearized solution by allowing $\alpha \to 0 (R \to \infty)$ in equation (3.18). Thus

$$L \to \tfrac{1}{2}\beta\pi F^2 - \tfrac{1}{2}\beta^3 \pi F^2 \int_0^\infty \frac{e^{-\kappa}(\kappa + \frac{1}{F^2})\kappa \, d\kappa}{\kappa \cosh(\kappa) - \frac{1}{F^2}\sinh(\kappa)}$$

as $\alpha \to 0$.

3.3(b) *A long, thin ellipse.*

The linearized theory appropriate in this case is derived by regarding β as a small parameter and expressing the solution $\tau(f)$ as a regular perturbation expansion in this quantity. Upon substituting into the flow equations and retaining only lowest order terms in β , a linear system of equations is obtained which, however, appears to be too difficult to solve in closed form. Accordingly, this theory will not be pursued further.

An alternative approach has been adopted by Lamb((1932, p.409), and was mentioned in Section 2.3. In this theory, it is assumed that the solution may be expressed as a small perturbation to the uniform flow $f = z$. This assumption is obviously not valid near the stagnation points at $z = \pm\alpha$, and the consequent failure of this theory for small α has already been described in Section 2.3. For the solution $f(z)$, Lamb's theory gives

$$f = z - \beta \int_0^\infty \frac{J_1(\alpha\kappa)}{\kappa} \frac{\frac{1}{F^2}\sin(\kappa z - i\kappa) + i\kappa\cos(\kappa z - i\kappa)}{\kappa\cosh(\kappa) - \frac{1}{F^2}\sinh(\kappa)}\, d\kappa . \qquad (3.20)$$

The free-surface elevation may be obtained from Lamb ((1932), p.410, eq.(8)). With the present choice of coordinate system, this becomes

$$y = 1 + \beta \int_0^\infty \frac{J_1(\alpha\kappa)\cos(\kappa x)}{\kappa\cosh(\kappa) - \frac{1}{F^2}\sinh(\kappa)}\, d\kappa . \qquad (3.21)$$

The function J_1 appearing in equations (3.20) and (3.21) is the first kind Bessel function of order one.

The interpretation of integrals of the type shown in equations (3.20) and (3.21) has already been discussed in Sections 2.3 and 3.3(a). For $F > 1$, a symmetric, wave-free solution is predicted. There is no solution for $F = 1$. When $F < 1$, the integrands in equations (3.20) and (3.21) possess singularities at $\kappa = \kappa_0$, where the positive real number κ_0 is the solution to the dispersion relation (2.18). Thus the solution (3.20) may be written

$$f = z - \beta\left\{ \int\!\!\!\!\!\!-_0^\infty \frac{J_1(\alpha\kappa)}{\kappa} \frac{\frac{1}{F^2}\sin(\kappa z - i\kappa) + i\kappa\cos(\kappa z - i\kappa)}{\kappa\cosh(\kappa) - \frac{1}{F^2}\sinh(\kappa)}\, d\kappa \right.$$

$$\left. + \frac{\pi J_1(\alpha\kappa_0)}{\kappa_0} \frac{\frac{1}{F^2}\cos(\kappa_0 z - i\kappa_0) - i\kappa_0\sin(\kappa_0 z - i\kappa_0)}{[1 + F^2\kappa_0^2 - \frac{1}{F^2}]\cosh(\kappa_0)} \right\} , \qquad (3.22)$$

and the free-surface elevation (3.21) becomes

$$y = 1 + \beta\left\{ \int\!\!\!\!\!\!-_0^\infty \frac{J_1(\alpha\kappa)\cos(\kappa x)}{\kappa\cosh(\kappa) - \frac{1}{F^2}\sinh(\kappa)}\, d\kappa \right.$$

$$\left. - \frac{\pi J_1(\alpha\kappa_0)\sin(\kappa_0 x)}{[1 + F^2\kappa_0^2 - \frac{1}{F^2}]\cosh(\kappa_0)} \right\} . \qquad (3.23)$$

For $F < 1$, the free surface thus consists of a wave-free region upstream of the semi-ellipse, followed in general by a train of downstream sine waves. Far downstream, equation (3.23) indicates that the free-surface elevation is of the form

$$y \to 1 - A_1 \sin(\kappa_0 x) \quad \text{as} \quad x \to +\infty,$$

in which the wave amplitude A_1 is given by

$$A_1 = \frac{2\pi\beta\, J_1(\alpha\kappa_0)}{[1 + F^2\kappa_0^2 - \frac{1}{F^2}]\cosh(\kappa_0)} \quad . \tag{3.24}$$

The wave drag D and lift L for this linearized theory are computed by substituting equation (3.22) into equations (3.8a) and (3.8b) respectively, resulting in the expressions

$$D = \tfrac{1}{4}A_1^2\left[1 - \frac{2\kappa_0}{\sinh(2\kappa_0)}\right] + 0(\beta^3) \tag{3.25a}$$

and

$$L = \frac{\pi}{2}\alpha\beta - 2\alpha - 2\beta F^2 \int_0^\infty \frac{J_1(\alpha\kappa)}{\kappa} \frac{[\frac{1}{F^2}\cosh(\kappa) - \kappa\sinh(\kappa)]\sin(\alpha\kappa)}{\kappa\cosh(\kappa) - \frac{1}{F^2}\sinh(\kappa)} d\kappa$$

$$+ 0(\beta^2) \quad . \tag{3.25b}$$

A remarkable feature of this theory is that the wave amplitude A_1 and linearized wave resistance D may become zero. This occurs each time the ellipse half-length α takes the value

$$\alpha = \frac{j_{1,s}}{\kappa_0} \quad , \quad s = 0,1,\ldots,$$

where $j_{1,s}$ is the s-th zero of the Bessel function J_1. Note that, as $\alpha \to 0$, the wave amplitude A_1 and drag D predicted by this theory also become zero.

3.4 Numerical Methods

To evaluate the linearized solution for an essentially circular ellipse, described in Section 3.3(a), it is necessary to obtain numerical values for the integral on the right hand side of equation (3.15). This integral is identical to the integral in equation (2.20), and may thus be evaluated at the surface by the technique described in Section 2.4(a).

Lamb's solution for a long, thin ellipse, described in Section 3.3(b), is evaluated from equations (3.22) and (3.23) by truncating the semi-infinite range of integration to a large, finite range. The Cauchy Principal Value integrals are then evaluated using the Trapezoidal Rule and Monacella's (1967) theorem, spacing points symmetrically about the singularity at $\kappa = \kappa_0$ so that the effect of the singularity may be ignored. Accurate polynomial approximations to the Bessel function J_1 are given in Abramowitz and Stegun (1972).

The numerical solution of the non-linear equations (3.5), (3.6) and (3.7) is exactly as described in Section 2.4(b). A vector of discrete function values $(\eta_0', \eta_1', \ldots, \eta_N')$ is used to represent the function $\eta_\phi(\phi, 1)$ at the $N + 1$ equally spaced free-surface points $\phi_0, \phi_1, \ldots, \phi_N$. The integro-differential equation (3.7) differs only trivially from equation (2.10), and the same process is therefore used to reduce it to a matrix equation for the quantities $\xi_1', \ldots, \xi_N'$

in terms of the unknowns $\eta'_1,\ldots,\eta'_N$. The radiation condition is now imposed at the first point ϕ_0 upstream; thus the quantities ξ_0, η_0 and η'_0 are obtained from equation (3.6) and the Bernoulli equation (3.5) then gives ξ'_0 . Finally, the Bernoulli equation (3.5) evaluated at each of the points $\phi_1,\ldots,\phi_N$ gives a system of N non-linear, algebraic equations in the N unknowns $\eta'_1,\ldots,\eta'_N$, which is solved by a process of Newtonian iteration. Solutions are usually obtained rapidly, due to the quadratic convergence of Newton's method, and when N = 130, converged non-linear free-surface profiles are usually obtained in five iterations, and require about two minutes of computing time on a CDC CYBER 173 machine. It is often sufficient to start the iteration process with an initially flat profile ($\eta' = 0$), although occasionally, a previously-computed non-linear solution is used for this purpose.

The wave resistance D and lift L experienced by the semi-elliptical body are computed from the non-linear free-surface profile using Cauchy's Integral Theorem to generate values of ξ' at points along the bottom $\psi = 0$. These values are numerically integrated to obtain ξ , using equation (3.6) to supply the value of ξ at the first point ϕ_0 upstream. Equations (3.11) are now solved by cubic-spline interpolation and Newton's method, and the drag D and lift L are evaluated from equations (3.10a) and (3.10b) respectively, using Simpson's Rule integration.

3.5 Presentation of Results

When $F < 1$, the linearized theories of Section 3.3 predict a surface profile free of waves upstream of the semi-ellipse, and in general possessing a downstream wave train. For $F > 1$, however, the surface is predicted to be symmetric about $x = 0$, and to possess no waves. These general features are confirmed by the non-linear results; in particular, a symmetric non-linear solution which is free of waves exists in a portion of the supercritical flow regime $F > 1$, and is similar to the solutions described in Section 2.5(b). We shall not consider these solutions further.

In Fig. 3.2(a), the wave drag D is shown as a function of the ellipse half-length α, for an ellipse of height $\beta = 0.02$ in a stream with $F = 0.8$. The dotted line indicates the predictions of the linearized theory of Section 3.3(a), in which the ellipse is assumed to be small and roughly circular, and was obtained from equation (3.17), whilst the results of Lamb's theory, computed from equation (3.25a), are indicated with a dashed line on the diagram. The points represent values of the drag computed from converged non-linear free-surface profiles, obtained for 36 different values of α. When α is large, the non-linear drag curve exhibits a marked shift to the right, which is in agreement with previously observed trends (see Schwartz (1981) and von Kerczek and Salvesen (1977)). Note that the non-linear drag is very small indeed at the two minima indicated on the diagram.

The lift L is shown as a function of α in Fig. 3.2(b), for both the linearized theories of Section 3.3, and for the 36 values of α at which the non-linear solution

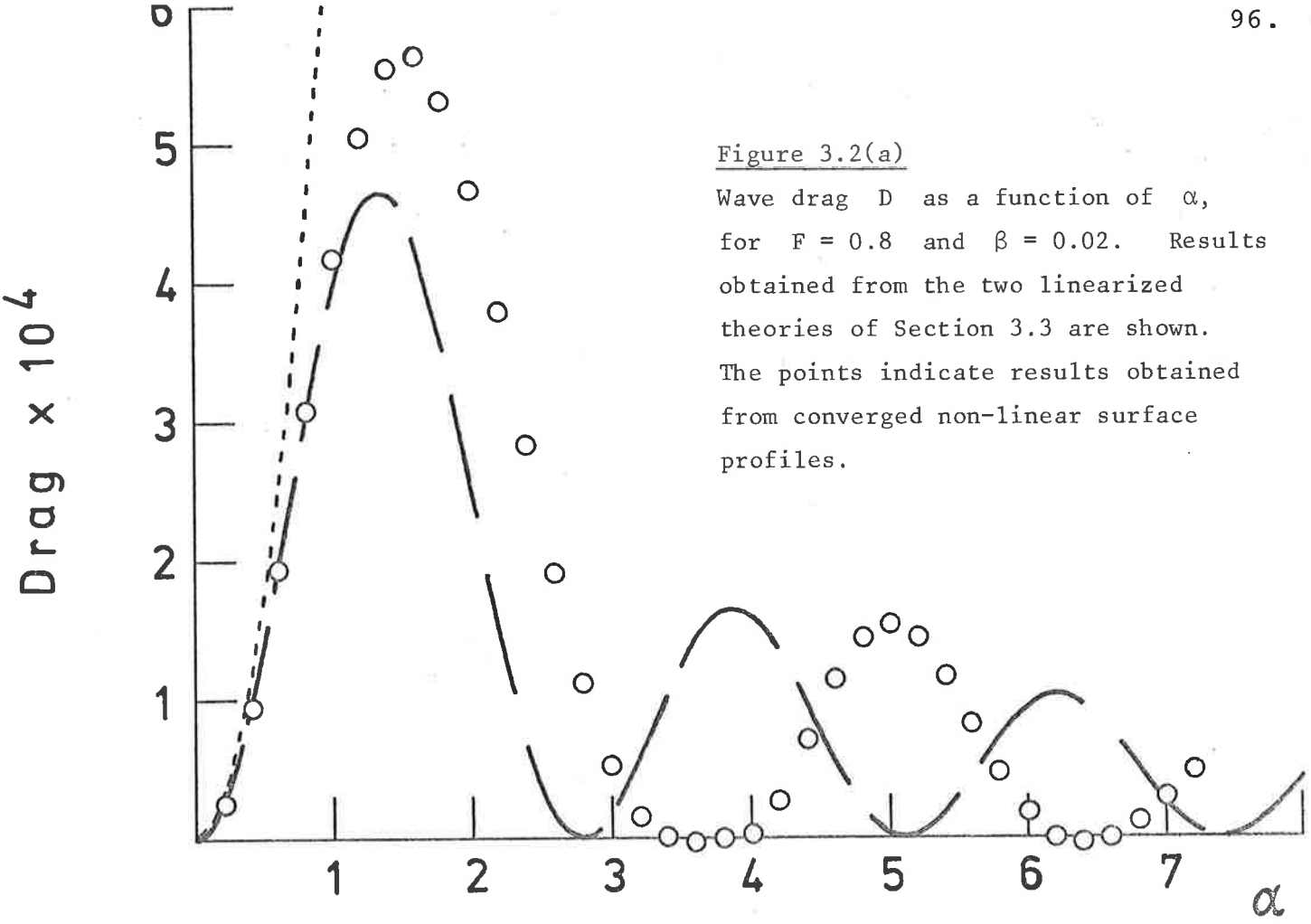

Figure 3.2(a)
Wave drag D as a function of α, for F = 0.8 and β = 0.02. Results obtained from the two linearized theories of Section 3.3 are shown. The points indicate results obtained from converged non-linear surface profiles.

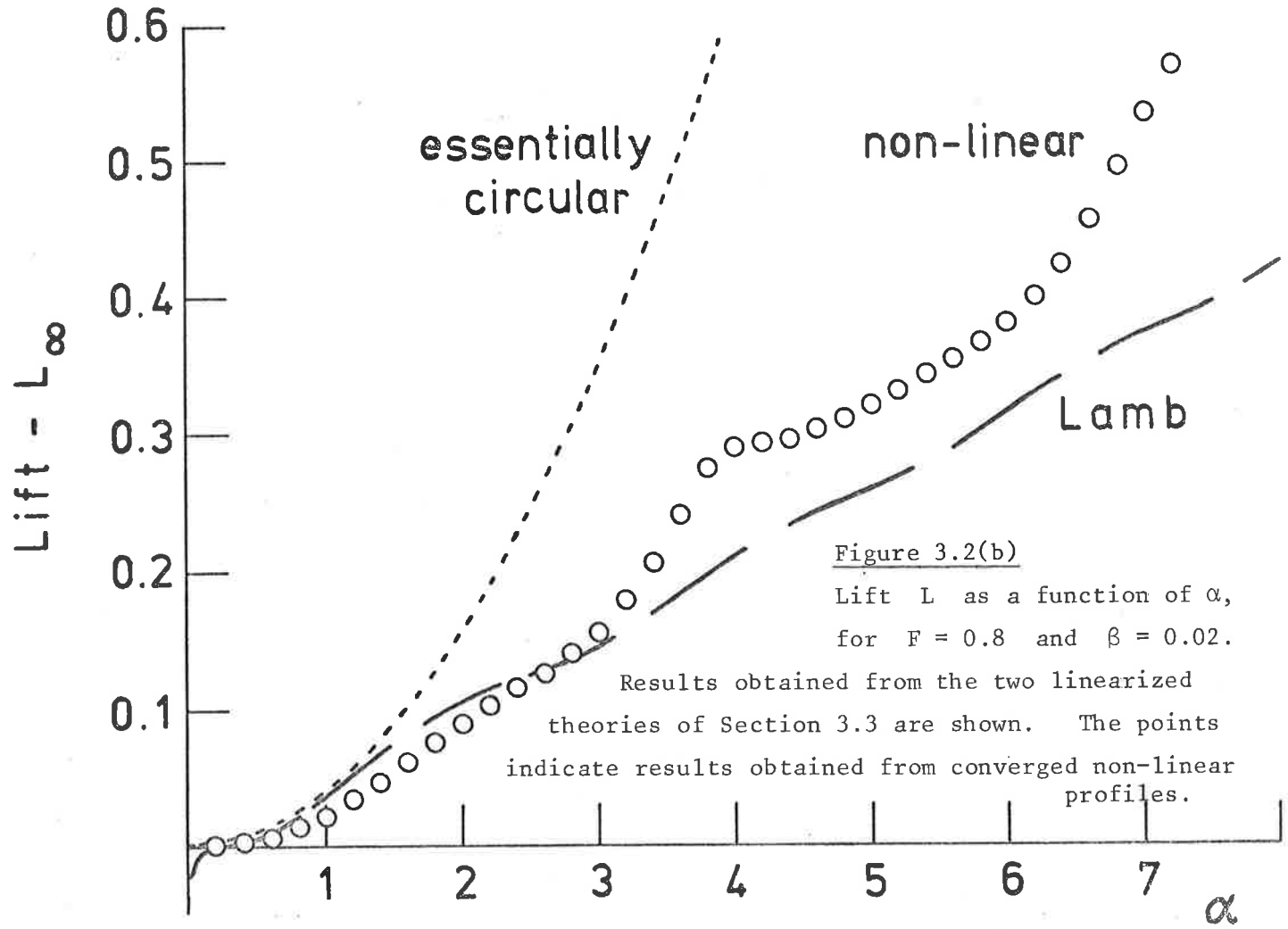

Figure 3.2(b)
Lift L as a function of α, for F = 0.8 and β = 0.02. Results obtained from the two linearized theories of Section 3.3 are shown. The points indicate results obtained from converged non-linear profiles.

was computed, with $F = 0.8$ and $\beta = 0.02$. To show more clearly the difference between the non-linear results and those of the two linearized theories, the reference value

$$L_\infty = \tfrac{1}{2}\alpha\left(1 + \frac{\beta}{\alpha}\right)^2 F^2 I - \alpha F^2 + \frac{\pi}{2}\alpha\beta - 2\alpha \ ,$$

where I is the quantity defined in equation (3.19), has been subtracted from the overall lift force. The quantity L_∞ is the lift that would be experienced by the semi-ellipse if the flow were the same as for flow about an ellipse in a fluid of infinite extent, for which the solution is $f = \tau(1 + \beta/\alpha)$. Note that

$$L_\infty \to \tfrac{1}{2}\beta\pi F^2 \quad \text{as} \quad \alpha \to 0 \ .$$

Lamb's theory, which has already been seen to fail for small α, predicts a lift force of zero in the limit $\alpha \to 0$. However, this result is not confirmed by either the linearized solution of Section 3.3(a) or apparently by the non-linear results; instead, these both predict a finite upward lift force as $\alpha \to 0$, as a consequence of the effects of leading edge suction. The non-linear lift force appears to exhibit local maxima at about the same values of α for which the non-linear drag vanishes.

In Fig. 3.3, the extent to which the non-linear downstream wave train may be made to vanish for special choices of α, β and F is investigated. Here, $F = 0.8$ and $\beta = 0.02$, as in Figs. 3.2. In Fig. 3.3, three non-linear free-surface profiles have been plotted; when $\alpha = 1.6$, the downstream wave amplitude, and hence also the wave drag in

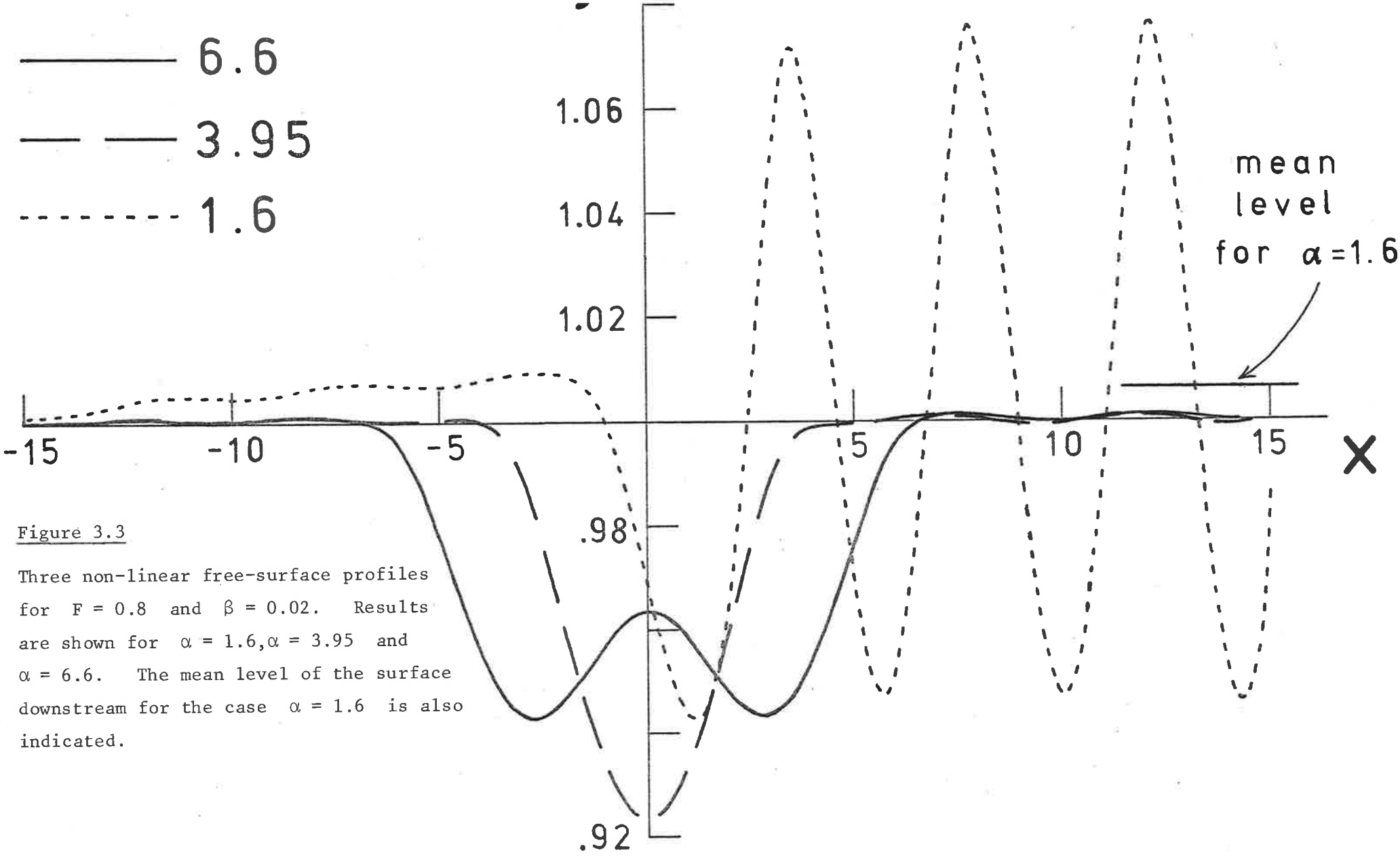

Figure 3.3

Three non-linear free-surface profiles for $F = 0.8$ and $\beta = 0.02$. Results are shown for $\alpha = 1.6, \alpha = 3.95$ and $\alpha = 6.6$. The mean level of the surface downstream for the case $\alpha = 1.6$ is also indicated.

Fig. 3.2(a), attains its maximum value for these values of F and β, whilst the downstream wave amplitude is at a minimum for $\alpha \sim 3.95$ and $\alpha \sim 6.6$. As with the solutions obtained in chapter two, the three non-linear solutions in Fig. 3.3 all exhibit a very small wave train *upstream* of the semi-ellipse. Again, this numerical error results from the truncation of the integrodifferential equation (3.7) at the first point ϕ_0, and the subsequent imposition of the radiation condition (3.6) there. The amplitude of the spurious upstream waves for the solution with $\alpha = 1.6$ in Fig. 3.3 has been reduced as far as possible by making small changes to the value of η_0 imposed at the first point ϕ_0, exactly as described in Section 2.5(a). The free-surface profile for $\alpha = 1.6$ is also slightly in error over the last quarter of a wavelength or so downstream, due to the truncation of the integrodifferential equation at the last point ϕ_N downstream. However, as with the solutions obtained in chapter two, errors from this source do not discernibly affect the remainder of the free-surface profile. Note that the mean level of the free surface downstream, computed by the technique described in Section 2.6, lies well above the undisturbed level $y = 1$ for the case $\alpha = 1.6$.

The amplitude of the downstream waves for the cases $\alpha = 3.95$ and $\alpha = 6.6$ shown in Fig. 3.3 is extremely small, being roughly the same size as the amplitude of the spurious upstream waves. Indeed, we believe that the presence of downstream waves is due only to the existence of the upstream

waves, and have no doubt that a surface profile totally without waves may be obtained by eliminating the small, numerically produced, upstream waves. Thus the non-linear drag curve of Fig. 3.2(a) is expected to pass through zero at $\alpha \sim 3.95$ and again at $\alpha \sim 6.6$. However, the non-linear drag in Fig. 3.2(a) is shown to vanish at slightly smaller values of α than these. This is due to a small numerical error in the procedure for computing the non-linear drag (described at the end of Section 3.4), which is again a consequence of imposing the radiation condition (3.6) at the point $f = \phi_0$ on the bottom. Thus, although the non-linear drag may be computed without difficulty for small α, the results are more subject to error as α becomes large and F becomes small.

The non-linear effects of the ellipse height β upon the downstream peak-to-trough wave height are investigated in Fig. 3.4. Results are presented for $\beta = 0.05$ and for $\beta = 0.1$, at $F = 0.5$. The predictions of Lamb's linearized theory, computed from equation (3.24), are indicated by dashed lines, whilst in the non-linear case, results were obtained for 36 different values of α when $\beta = 0.5$, and for 39 values of α when $\beta = 0.1$, and are indicated by points in Fig. 3.4. The wave drag is not shown for these cases, since the error which occurs in the computation of the non-linear wave resistance at large values of α renders the accuracy of the results uncertain.

According to Lamb's linearized theory, described in Section 3.3(b), the values of α at which the wave height becomes zero are functions only of F, and do not depend

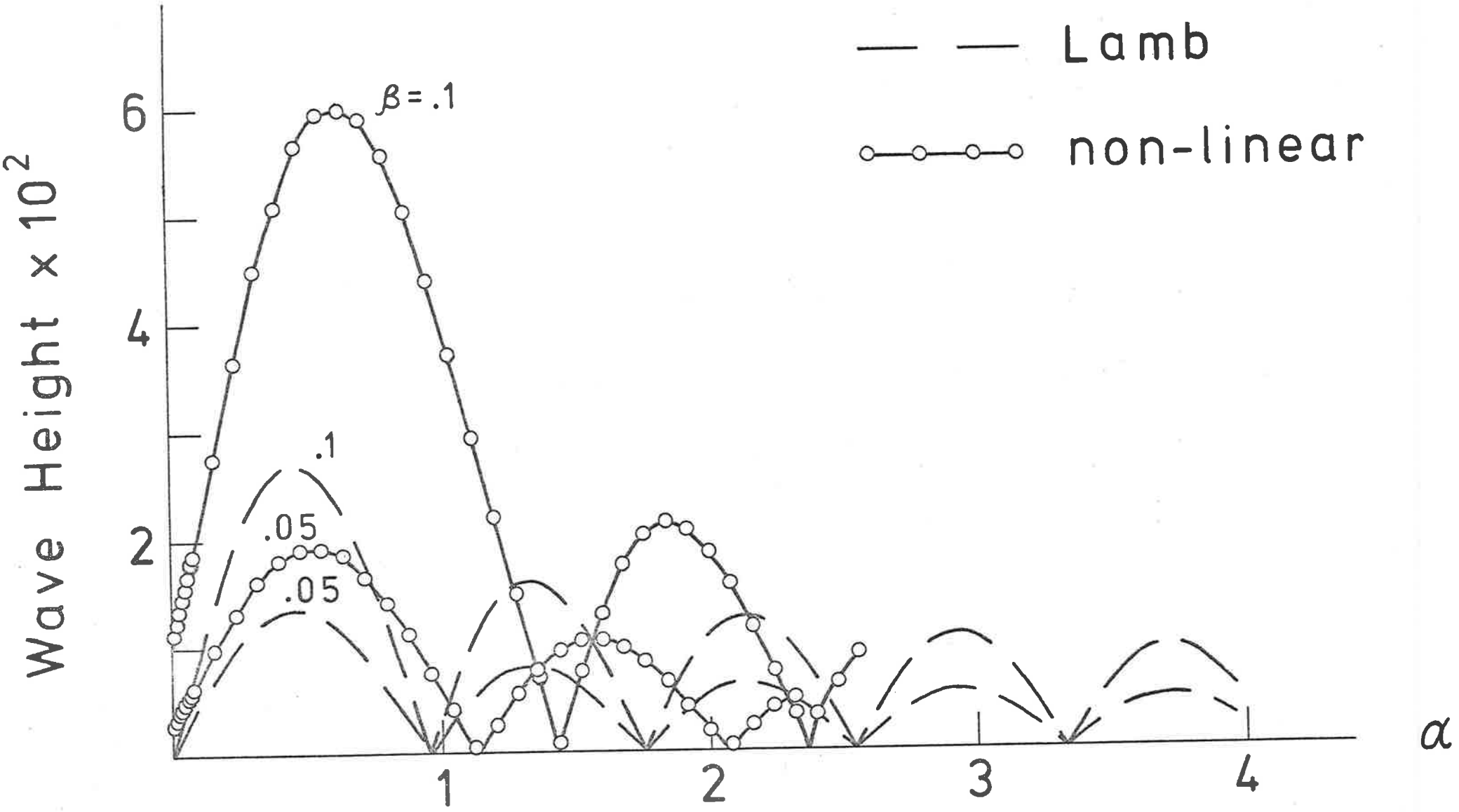

Figure 3.4 Downstream wave height as a function of α, for $F = 0.5$. The linearized theory of Lamb, discussed in Section 3.3(b), and the non-linear results are presented for $\beta = 0.05$ and for $\beta = 0.1$.

on β . However, the non-linear results in Fig. 3.4 show a strong dependence upon β . For $\beta = 0.05$, the non-linear wave height takes its first minimum at a value of α which is about 20 per cent larger than the value predicted by Lamb's theory, and for $\beta = 0.1$, the value of α at which the first minimum occurs is some 50 per cent greater than Lamb's linearized result. At this value of the Froude number, surface profiles have again been computed for which the height of the downstream waves is extremely small, and we do not doubt that it may be made to vanish altogether by eliminating the spurious waves from the upstream portion of the flow.

In the limit $\alpha \to 0$, the ellipse degenerates to a vertical plate of zero thickness and height β attached to the bottom of the stream. Lamb's theory ceases to be valid for small α , and predicts that the downstream wave train vanishes as $\alpha \to 0$. Of course, the non-linear results in Fig. 3.4 do not confirm this prediction, and indicate instead that the downstream wave height remains finite as $\alpha \to 0$. The linearized theory of Section 3.3(a), in which the ellipse is assumed to be small and roughly circular, appears to provide a reasonably good estimate for the downstream wave height in this limiting case; allowing α to become zero in equation (3.16) gives a peak-to-trough wave height $2A_1$ of 2.32×10^{-3} for $\beta = 0.05$ and 9.27×10^{-3} for $\beta = 0.1$, when $F = 0.5$.

3.6 Summary and Further Remarks

The problem investigated in chapter two has been generalized in a straightforward manner to include the case of two-dimensional steady flow about a submerged semi-ellipse. The problem is again formulated using the complex potential $f = \phi + i\psi$ as the independent variable, and is solved using the boundary-integral technique of chapter two.

Two linearized theories have been discussed. The first of these is a straightforward generalization of the linear theory of chapter two, and is derived under the assumption that the ellipse is an essentially circularly-shaped object. However, it also appears to provide reasonable results for ellipses of very high aspect ratio $R = \beta/\alpha$, although it ceases to be valid for ellipses for which α is large. The second linearized theory which was investigated is based upon the classical solution of Lamb, and requires the ellipse to be a long, thin obstacle. According to this theory, the amplitude of the downstream wave train, and hence also the wave drag, may become zero for ellipses of certain special lengths. However, the assumptions implicit in this theory are locally violated in the neighbourhood of the stagnation points at each end of the semi-elliptical body, and, apparently as a consequence of this, the theory fails for small α.

The exact non-linear equations of motion are solved numerically, using a Newtonian iteration scheme to obtain the free-surface profiles. For $F > 1$, the symmetric, wave-free profile predicted by the linearized solutions is

confirmed by the non-linear results. For $F < 1$, the non-linear surface profile is essentially free of waves upstream, and generally possesses a train of Stokes waves downstream. The remarks made in chapter two concerning the possible non-uniqueness of non-linear solutions are doubtless applicable here also; there exists the possibility of a region of overlap in the supercritical flow regime $F > 1$, in which both the symmetric wave-free solution and a solution possessing a downstream wave train exist simultaneously. In addition, it is possible that solutions of the type described by Aitchison (1979) may also be found.

As with Lamb's linearized solution, the non-linear results also appear to indicate that the downstream wave height and the wave resistance may both become zero for certain ellipse lengths. These special ellipse lengths are functions only of the Froude number F in Lamb's theory, although they also become strongly dependent upon the ellipse height β when the effects of non-linearity are included.

Although free-surface profiles for $F < 1$ have been obtained in which the downstream wave height is extremely small, we have not yet observed it to vanish completely. This appears to be due to the necessity of the present numerical method to impose a radiation condition at the first point upstream. Consequently, a spurious, numerically-produced wave train is present upstream, and it appears that the very small downstream waves which are obtained may only be made to vanish completely by ridding the free surface of the spurious upstream waves. To search for configurations

having exactly zero drag, it may perhaps be possible to formulate the problem differently, taking advantage of the symmetry of the solution about $x = 0$ for these cases, and allowing all the free-surface points to vary. The parameter α would presumably be an unknown quantity, to be obtained along with the free-surface profile in the Newton's method solution of the problem. Work is presently continuing on this non-linear eigenvalue problem.

REFERENCES

Abramowitz, M. and Stegun, I.A. 1972 *Handbook of mathematical functions.* Dover.

Aitchison, J.M. 1979 A variable finite element method for the calculation of flow over a weir. *Rutherford Laboratory report no. RL-79-069.*

Benjamin, T.B. 1970 Upstream influence. *J. Fluid Mech.* 40, 49 - 79.

Cabannes, H. 1951 *ONERA Note Technique*, No. 5.

Cokelet, E.D. 1977 Steep gravity waves in water of arbitrary uniform depth. *Phil. Trans. Roy. Soc. London*, A 286, 183 - 230.

Domb, C. and Sykes, M.F. 1957 On the susceptibility of a ferromagnetic above the Curie Point. *Proc. Roy. Soc. London* A 240, 214 - 228.

Forbes, L.K. and Schwartz, L.W. 1981 Supercritical flow past blunt bodies in shallow water. To appear in *Zeit. Angew. Math. Phys. (ZAMP).*

Forbes, L.K. 1981 On the evolution of shock-waves in mathematical models of the aorta. To appear in *J. Austral. Math. Soc.* B 22.

Haussling, H.J. and Coleman, R.M. 1977 Finite-difference computations using boundary-fitted coordinates for free-surface potential flows generated by submerged bodies. *Proc. 2nd. Int. Conf. on Numerical Ship Hydrodynamics.* 221 - 233.

Havelock, T.H. 1927 The method of images in some problems of surface waves. *Proc. Roy. Soc. London* A 115, 268 - 280.

Hayes, W.D. and Probstein, R.F. 1966 *Hypersonic flow theory*, vol. 1. Academic.

Kochin, N.E., Kibel', I.A. and Roze, N.V. 1964 *Theoretical Hydromechanics* (tr. from 5th Russian edition). Interscience.

Lamb, H., 1932 *Hydrodynamics* (6th edition) Cambridge University Press.

Monacella, V.J. 1967 On ignoring the singularity in the numerical evaluation of Cauchy Principal Value integrals. *U.S. Department of the Navy, Hydromechanics Lab., Research and Development report no. 2356.* David Taylor Model Basin (Washington D.C.)

Pandolfi, M. and Zannetti, L. 1977 Numerical investigations about the predictions of free surface shallow water motions. *Proc. 6th Australian Hydraulics and Fluid Mech. Conf.* 364 - 368.

Preiswerk, E. 1938 *Mitt. aus dem Inst. für Aerodynamik*, No. 7.

Salvesen, N. and von Kerczek, C. 1978 Nonlinear aspects of subcritical shallow-water flow past two-dimensional obstructions. *J. Ship. Res.* 22, 203 - 211.

Schwartz, L.W. 1974a Hypersonic flows generated by parabolic and paraboloidal shock waves. *Phys. Fluids* 17, 1816 - 1821.

Schwartz, L.W. 1974b Computer extension and analytic continuation of Stokes' expansion for gravity waves. *J. Fluid Mech.* 62, 553 - 578.

Schwartz, L.W. 1975 Series solution for the planar asymmetric blunt-body problem. *Phys. Fluids* 18, 1630 - 1638.

Schwartz, L.W. 1981 Nonlinear solution for an applied overpressure on a moving stream. To appear in *J. Engineering Maths.*

Shanks, S.P. and Thompson, J.F. 1977 Numerical solution of the Navier-Stokes equations for 2D hydrofoils in or below a free surface. *Proc. 2nd Int. Conf. on Numerical Ship Hydrodynamics.* 202 - 220.

Stoker, J.J. 1957 *Water Waves.* Interscience.

Stokes, G.G. 1880 *Mathematical and Physical Papers*, vol. 1. Cambridge University Press.

Tuck, E.O. 1965 The effect of non-linearity at the free surface on flow past a submerged cylinder. *J. Fluid Mech.* 22, 401 - 414.

Van Dyke, M.D. 1958a A model of supersonic flow past blunt axisymmetric bodies, with application to Chester's solution. *J. Fluid Mech.* 3, 515 - 522.

Van Dyke, M.D. 1958b The supersonic blunt-body problem - review and extension. *J. Aerospace Sci.* 25, 485 - 496.

Van Dyke, M.D. 1975 Computer extension of perturbation series in fluid mechanics. *S.I.A.M. (Soc. Ind. Appl. Math.) J. Appl. Math.* 28, 720 -734.

Von Kerczek, C. and Salvesen, N. 1977 Non-linear free-surface effects - the dependence on Froude number. *Proc. 2nd. Int. Conf. on Numerical Ship Hydrodynamics.* 292 - 300.

Wehausen, J.V. and Laitone, E.V. 1960 Surface waves. In *Handbuch der Physik*, vol. 9, Springer-Verlag.

Werlé, H. 1973 Hydrodynamic flow visualization. *Ann. Rev. Fluid Mech.* 5, 361 - 382.

Wynn, P. 1966 On the convergence and stability of the epsilon algorithm. *S.I.A.M. (Soc. Ind. Appl. Math.) J. Numer. Anal.* 3, 91 - 121.

Yamada, H. 1957 On the highest solitary wave. *Rep. Res. Inst. for Appl. Mech., Kyushu University* 5, 53 - 67.